Skoltech
Skolkovo Institute of Science and Technology

Skolkovo Institute of Science and Technology

PRECLINICAL TESTING OF NEW MODALITIES FOR PET VISUALIZATION
AND TREATMENT OF RAS-DRIVEN CANCERS

Doctoral Thesis

by

ANNA A. MOROZ

DOCTORAL PROGRAM IN LIFE SCIENCES

Supervisor

Professor Konstantin Severinov

Co-Supervisor

Professor Michael Evans

Moscow - 2018

Abstract

RAS isoforms are commonly mutated oncogenes, as it hyperactivity drives the pathobiology of several major public health challenges including pancreatic adenocarcinoma, colorectal cancer, and lung cancer [Fernández-Medarde A. et al, 2011]. Despite the compelling cell biology showing that tumours can be highly "addicted" to RAS signaling, over 20 years of medicinal chemistry developing direct small molecule inhibitors of RAS isoforms have yielded no clinically active therapies. On this basis, RAS is generally designated by the cancer community as an "undruggable" oncogene [Cox A et al, 2014].

Up to 30% of all human cancer types have mutations in one or all three RAS genes including more than a half of colon cancers (~55%) and stunning 97% of pancreatic cancers (PC). Taking just PC alone, as a common type of cancer, we obtain the following figures: more than 250,000 cases have been reported per year over the last twenty years [Torre et al, 2012; Siegel et al, 2015; Rahib et al, 2012]. Since treatment efficacy in oncology correlates with the early diagnostics and correct staging of the disease, finding new biological targets specific to cancer cells potentially serving as action points for therapy or good sites for diagnostics is of the utmost importance.

In my work I explore an antibody against CDCP1 for both imaging and targeted radio therapeutic potency in tumours positive for mutated RAS and specifically PC model. Anti-CDCP1 antibody was radiolabeled with ^{89}Zr or ^{177}Lu, and its properties were studied in vivo in both PDX and HPAC pancreatic cancer cell line animal models. Mice injected with ^{89}Zr were imaged (PET/CT) at various time points followed by a biodistribution study. To assess the treatment potency of anti-CDCP1, the antibody was radiolabeled with ^{177}Lu and injected in nu/nu mice bearing subcutaneous HPAC tumours. The treatment effect was assessed by measuring tumour sizes via caliper, and dosimetry studies were performed using SPECT/CT.

Applying the previously described labeling methods (Martinko et al, 2018), we have achieved high (90%+) labeling efficacy for both isotopes. *In vitro* nuclear imaging showed an increase in both accumulation and SNR over time, peaking at ~16% ID/g at 72-hour time point, with extremely low background values. A biodistribution assay have demonstrated a measurable non-specific uptake in liver and bone tissues.

For the therapeutic arm of the experiment, a significantly lower tumour growth was observed in animals treated with anti-CDCP1 ^{177}Lu labeled abs. The results of this study have also confirmed the ability of anti-CDCP1 antibody labeled with [89]Zr to produce good quality images, allowing for further studies aiming to translate this approach into clinical diagnostics of PC, specifically to monitor tumour progression and assess tumour burden. Moreover, treating the PC tumours with anti-CDCP1 ^{177}Lu labeled abs has demonstrated a significant effect that opens up a way to further studies exploring a therapeutic potential for this method.

Publications

Manuscripts:

1. "A preclinical assessment of ^{89}Zr-atezolizumab identifies a requirement for carrier added formulations not observed with ^{89}Zr-C4.

   Moroz, Anna; Lee, Chia Yin; Wang, Yung-hua; Hsiao, Jeffrey; Sevillano, Natalia; Truillet, Charles; Craik, Charles; Fong, Lawrence; Wang, Cheng-I; Evans, Michael. Bioconjugate Chemistry, Publication Date (Web): September 18, 2018 DOI: 10.1021/acs.bioconjchem.8b00632"

2. "Imaging PD-L1 Expression with ImmunoPET.

   Charles Truillet, Hsueh Ling J. Oh, Siok Ping Yeo, Chia-Yin Lee, Loc T. Huynh, Junnian Wei, Matthew F. L. Parker, Collin Blakely, Natalia Sevillano, Yung-Hua Wang, Yuqin S. Shen, Victor Olivas, Khaled M. Jami, **Anna Moroz**, Benoit Jego, Emilie Jaumain, Lawrence Fong, Charles S. Craik, Albert J. Chang, Trever G. Bivona, Cheng-I Wang, and Michael J. Evans. Bioconjugate Chemistry 2018 29 (1), 96-103 DOI: 10.1021/acs.bioconjchem.7b00631"

3. "Targeting iron metabolism in high grade gliomas with 68Ga-citrate PET/MR.

   Spencer Behr, Javier E. Villanueva-Meyer, Yan Li, Yung-Hua Wang, Junnian Wei, **Anna Moroz**, Julia K Lee, Jeffrey C Hsiao, Kenneth T Gao, Wendy Ma, Soonmee Cha, David Wilson, Youngho Seo, Sarah Nelson, Susan Chang, Michael J Evans. JCI Insight. 2018 Nov 2; 3(21): e93999. DOI: 10.1172/jci.insight.93999

4. "Adoptive immunotherapy with genetically engineered T lymphocytes modified to express chimeric antigen receptors. Review.

   Anna Pavlova (Moroz), Maschan M.A., Ponomarev V.B. Oncohematology. 2017;12(1):17-32. (In Russian.) DOI: 10.17650/1818-8346-2017-12-1-17-32"

Abstracts:

1. "Remodeling of the cell surface proteome presents new opportunities for the treatment of RAS driven malignancies.

    Anna Moroz, Alexander Martinko, Junnian Wei, Yung-Hua Wang, Jeffrey C. Hsiao, Sean D. Carlin, Jeremy Sharib, Charles Truillet, Kimberly Kirkwood, James A. Wells, Michael J. Evans. 15th Annual Radiology Imaging Research Symposium, October 23, 2018. Abstract & Poster"

2. "Targeting mTORC1 signaling to detect tuberous sclerosis complex and lymphangioleiomyomatosis with PET.

    Anna Moroz, Charles Truillet, Junnian Wei, Yung-Hua Wang, Jeffrey C. Hsiao, Sean D. Carlin, Davide Ruggero, Kevin Leung, James A. Wells, Hilaire Lam, Elizabeth P. Henske, Michael J. Evans. 15th Annual Radiology Imaging Research Symposium, October 23, 2018. Abstract & Poster"

3. "A preclinical assessment of 89Zr-atezolizumab identifies a requirement for carrier added formulations not observed with 89Zr-C4.

    Anna Moroz, Lee, Chia-Yin, Yung-hua Wang, Jeffrey C. Hsiao, Natalia Sevillano, Charles Truillet, Charles S. Craik, Lawrence Fong, Cheng-I Wang, Michael J. Evans. 15th Annual Radiology Imaging Research Symposium, October 23, 2018. Abstract & Poster"

4. "The effect of lactate dehydrogenase-A (LDH-A) knockdown and human prostate-specific membrane antigen (hPSMA) directed CAR T cell treatment on hPSMA(+) Myc-CaP tumors.

    Mayuresh M. Mane, Khalid Shalaby, Ivan Cohen, Avi S. Albeg, Jenny Ijoma, Myat Ko, Masatomo Maeda, Kiranmayi Vemuri, Jaya Satagopan, **Anna Moroz**, Juan Zurita, Larissa Shenker, Ellen Ackerstaff, Masahiro Shindo, Ekaterina Moroz, Maxim

A. Moroz, Inna Serganova, Jason Koutcher, Vladimir Ponomarev, Ronald G. Blasberg. Fourth CRI-CIMT-EATI-AACR International Cancer Immunotherapy Conference 2018, Abstract & Poster."

5. "Imaging hPSMA-directed CAR T cell tumor targeting and efficacy in murine prostate tumors with LDH-A knockdown.

Mayuresh M. Mane, Khalid Shalaby, Ivan Cohen, Avi S. Albeg, Jenny Ijoma, Myat Ko, Masatomo Maeda, Kiranmayi Vemuri, Jaya Satagopan, **Anna Moroz**, Juan Zurita, Larissa Shenker, Ellen Ackerstaff, Masahiro Shindo, Ekaterina Moroz, Maxim A. Moroz, Inna Serganova, Jason Koutcher, Vladimir Ponomarev, Ronald G. Blasberg. World Molecular Imaging Congress (WMIC) 2017, Abstract & Poster."

6. "Concurrent and simultaneous multi-reporter bioluminescence imaging (BLI). Maxim A. Moroz, Juan Zurita, Larissa Shenker, **Anna Pavlova (Moroz)**, Inna Serganova, Ronald Blasberg, Vladimir Ponomarev. World Molecular Imaging Congress (WMIC) 2016 Abstract & Poster."

7. "Imaging theefficacy of TRAIL-enhanced CAR T-cell immunotherapy. Maxim A. Moroz, Juan Zurita, **Anna Pavlova (Moroz)**, Nikita Sumzin, Larissa Shenker, Prasad Adusumilli, Vladimir Ponomarev. World Molecular Imaging Congress (WMIC) 2016 Abstract & Poster."

Acknowledgements

The author thanks:

Professor Severinov and members of biology program in Skolkovo Institute of Technology for guidance and profound support.

Professor Evans, members of UCSF and collaborators from other institutes for time and effort invested in me, while I learned, including Professor Jim Wells, Professor Charles Craik, Professor Charles Truillet, Professor Youngho Seo, Dr. Elizabeth P. Henske, Dr. Sean D. Carlin, Dr. Alexander Martinko, Dr. Kevin Leung, and Dr. Junnian Wei.

Table of Contents

List of Symbols and Abbreviations

Ab – Antibody

ADC – Antigen Delivery System

AML – Acute Myeloid Leukemia

ATCC – American Type Culture Collection

BFCA – Bi-Functional Chelating Agent

Bq – Becquerel

Bp /kb – Base Pairs / Kilo Base Pairs

CAPRI – Calcium-promoted RAS Inactivator

CAS9 – Caspase 9

CCD – Charge-coupled Device

CD – Cluster of Differentiation

CDCP1 – CUB Domain Containing Protein 1

Ci – Curie

CRISPR – Clustered Regularly Interspaced Short Palindromic Repeats.

CT – Computed Tomography

Cu – Cuprum

Cys – Cysteine

Da – Dalton

DAR – Digital Autoradiography

DFO – Desferrioxamine

DMSO – Dimethyl sulfoxide

DOTA – 1, 4, 7, 10-tetraazacyclododecane-1, 4, 7, 10-tetracetic acid

DTPA – NR-diethylenetriaminepentacetic acid

ECD – Extracellular Domain

EGFR – Epidermal growth factor receptor

ERK – Extracellular Signal-regulated Kinase

F –Fluorine

Fab – Fragment Antigen Binding

FACS – Fluorescence-Activated Cell Sorter

Fc – Constant Fragments

FDA – Food Drug Administration

FDG – Fluoro-Deoxyglucose

Ga – Gallium

GDP – Guanosine Diphosphate

GEF – Guanine Nucleotide Exchange Factor

GFP – Green Fluorescent Protein

Gly – Glycine

GSK – Glycogen Synthase Kinase

GTP – Guanosine Triphosphate

Gy – Grey

HD – Heat Denaturating

H&E – Hematoxylin Eosin

HNSCC – Head and Neck Squamous Cell Carcinoma

HSP90 – Heat Shock Protein 90

HVR – Hypervariable region

I – Iodine

ID/g – Injected Dose per gram

IgG – Immunoglobin G

In – Indium

Kd – Kilodalton

KeV – Kiloelectron Volt

LAM – Lymphangioleiomyomatosis

LD – Lipid Droplet

Lu – Lutetium

MAPK – Mitogen-activated Protein Kinase

mAb – Monoclonal Antibody

mM – Millimole

mRNA – Matrix Ribonucleic Acid

mTOR – Mechanistic Target of Rapamycin

NFAT – Nuclear factor of activated T cells

Ng – Nanogram

Nm – Nanometre

NOTA – 1, 4, 7-triazacyclononane-1, 4, 7-acetic acid

NSG – NOD scid gamma

OIS – Oncogene-Induced Senescence

PBS – Phosphate-buffered saline

PC – Pancreatic Cancer

PD1 – Programmed Death Receptor 1

PDAC – Pancreatic Ductal Adenocarcinoma

PDL1 – Programmed Death Ligand 1

PDX – Patient Derived Xenografts

PET – Positron Emission Tomography

PI3K – Type I phosphoinositide 3-kinases

PKC – Protein Kinase C

PKCδ – Protein Kinase C δ

PTM – Translational Lipid Modifications

RAS – Protein family (RAts Sarcoma)

RCE1 - RAS-converting enzyme 1

RNA – Ribonucleic Acid

SI – Switch 1

SII – Switch 2

Ser – Serin

SFK – Src Family Kinases

sgRNA – Single Guide RNA

siRNA – Short Interfering RNA

SNR – Signal to Noise Ratio

SPECT – Single Photon Emission Computed Tomography

SUV – Standardized Uptake Values

TAG – Tumour-Associated Glycoprotein

Tc – Technetium

TRASK – Transmembrane protein associated with Src kinases

TSC – Tuberous Sclerosis Complex

μg – Microgram

μl – Microlitre

USCF – University California San Francisco

VH – Heavy Chain

VL – Light Chain

Y – Yttrium

Zr – Zirconium

List of Figures

List of Tables

Novelty

In this work, CDCP1 protein was assessed as a possible target for immunotherapy of RAS-driven cancers. The translational value of this work was increased by using not only cancer cell-derived xenograft animal models, but also patient derived xenografts (PDX) developed from biopsy materials of patients with pancreatic cancer (98% RAS driven disease). To achieve that radiolabelling of the anti-CDCP1 antibodies with isotopes 89-Zirconium and 177-Lutetium was performed, which allowed to use both PET (with ^{89}Zr) and SPECT (with ^{177}Lu). A decrease of tumour burden accompanied by increase of the overall survival was demonstrated in groups treated with anti-CDCP1 with ^{177}Lu as well as first successful ImmunoPET imaging with anti-CDCP1 with ^{89}Zr. The results were achieved *in vitro* and validated *in vivo*. On this basis, a comprehensive model of the RAS-driven cancer diagnostics and treatment has been validated and can be extended to other forms of cancer and even introduced into the clinic once further more detailed work is done.

In the study with ^{89}Zr labeled transferrin my colleagues and I have successfully assessed and described a new molecular imaging approach that may improve detecting and monitoring procedures of clinically problematic cells arising from TSC and/or LAM.

Findings from reverse translational study with ^{89}Zr labeled Atezolizumab has, for the first time revealed a special importance of lower specific activity to measure tumour-associated PD-L1, especially for tumours with modest antigen expression. Measuring PD-L1 with non-invasive imaging is an unusual clinical challenge, as it does not need to be overexpressed to promote tumour growth, and patients with as little as 1% of PD-L1 positive cells on immunohistochemistry can experience durable clinical responses to checkpoint inhibitors therapies. My results provided a novel approach to achieve that goal.

Personal contribution

The main part of *in vitro* and all *in vivo* research for all three parts of this project was performed by the author. The antibodies were purified and after bioconjugation with chelator agents were radiolabeled with ^{89}Zr and ^{177}Lu. Cancer cell lines were analyzed using Flow Cytometry and used to develop cell line-derived and patient-derived xenografts in experimental animals. The resulting animal models were further used for imaging (PET/SPECT/CT) and therapeutic studies applying radiolabeled CDCP1/Atezo and Transferrin proteins as diagnostic and treatment agents in different groups of animals. After the end point of the experiment extensive *ex vivo* tests were performed, including biodistribution and histology.

Introduction

A complex network of signaling pathways controls normal cell behavior in multicellular organisms. This network assures proper function, including protein expression, rate of proliferation and cellular death [Perbal et al, 2003]. A pathway malfunction leads to a loss of normal cell functioning and in most cases induces a disease. Specifically, for oncology, the vast majority of cancers are found to have various pathway mutations responsible for the breakdown of normal growth regulation, making this area of biology critical for understanding and treating this malady. In my work, I have focused on developing an approach to target RAS protein family, as one of the most prominent players in cancer regulation and, currently, one of the primary targets of cancer research. Specifically, I was studying CDCP1 as a potential target for distinguishing between normal cells and cells carrying mutated RAS in order to target the latter with the newly developed anti-CDCP1 radiolabeled antibodies for diagnostic and therapeutic purposes.

The cutting-edge and one of the most rewarding strategies to cure cancer today is immunotherapy [Zavala V et al, 2015]. It is based on harnessing the variety of body self-defense tools against tumour. Some methods involve development of modified immune cells [Geyer et al, 2016], some rely on deactivating tumour suppression of the host immune system [Pardoll et al, 2012], and others involve specific delivery of therapeutic or diagnostic tools directly to the cancer site using antibodies as vehicles [Nicodemus et al, 2015]. In my work, I used Anti-CDCP1 antibody that I have labeled with isotopes of Zirconium and Lutetium (89 and 177 respectively), and used their specific chemical and physical properties for therapy and diagnostics of one of the RAS related cancers – pancreatic cancer.

Chapter 1. Review: RAS Protein Family

1.1. Overview

One of the first proteins identified to play a significant role in cell growth control was the product of the RAS oncogene. This name is an acronym derived from *RA*t *S*arcoma since this gene was primarily identified in strains of rat sarcoma viruses [Harvey et al, 1964]. While seeking for dominant oncogenes in both humans and animals, scientists revealed most of these genes to be mutant alleles of cellular RAS genes [Takai Yet al, 2001]. Moreover, RAS mutations were found in tumours induced by retroviruses that lack oncogene sequences, suggesting that viral integration in the vicinity of cellular proto-oncogenes leads to point mutations in their sequences and constitutive activation of RAS proteins [Hayward et al, 1981]. Since that discovery in early 1980s, RAS superfamily has been a focus of intense research in the field of cancer biology.

The recent classification of RAS superfamily divides its members into five sub-families: RAS, RHO, RAB, Sar1/Arf and RAN (Figure 1) [Simuanshu et al, 2017]. The functions of different families were relatively recently determined to be as follows: RAS subfamily members mainly regulate gene expression, Rho family proteins regulate gene expression and cytoskeletal reorganization [Narumiya et al, 2018], RAB proteins regulate intracellular vesicle trafficking [Pylypenko O et al, 2017], RAN – nucleocytoplasmic transport during different phases of cell cycle, microtubule organization during mitosis [Sheng et al, 2018]. Three RAS genes are found in mammalian genomes: HRAS, KRAS and NRAS [Barbacid et al, 1987]. Alternative splicing of KRAS transcript results in two proteins isoforms: KRAS-4A, KRAS-4B increasing the total number of protein isoforms to four.

These are ubiquitously expressed low-molecular weight (21 kDa) guanine nucleotide binding proteins with intrinsic GTPase activity. Nowadays, the RAS signaling pathway is

well-studied at the molecular level in a variety of organisms. [Campbell et al, 1998], as well

as the structure of the key proteins of this pathway [Wittinghofer et al, 1998].
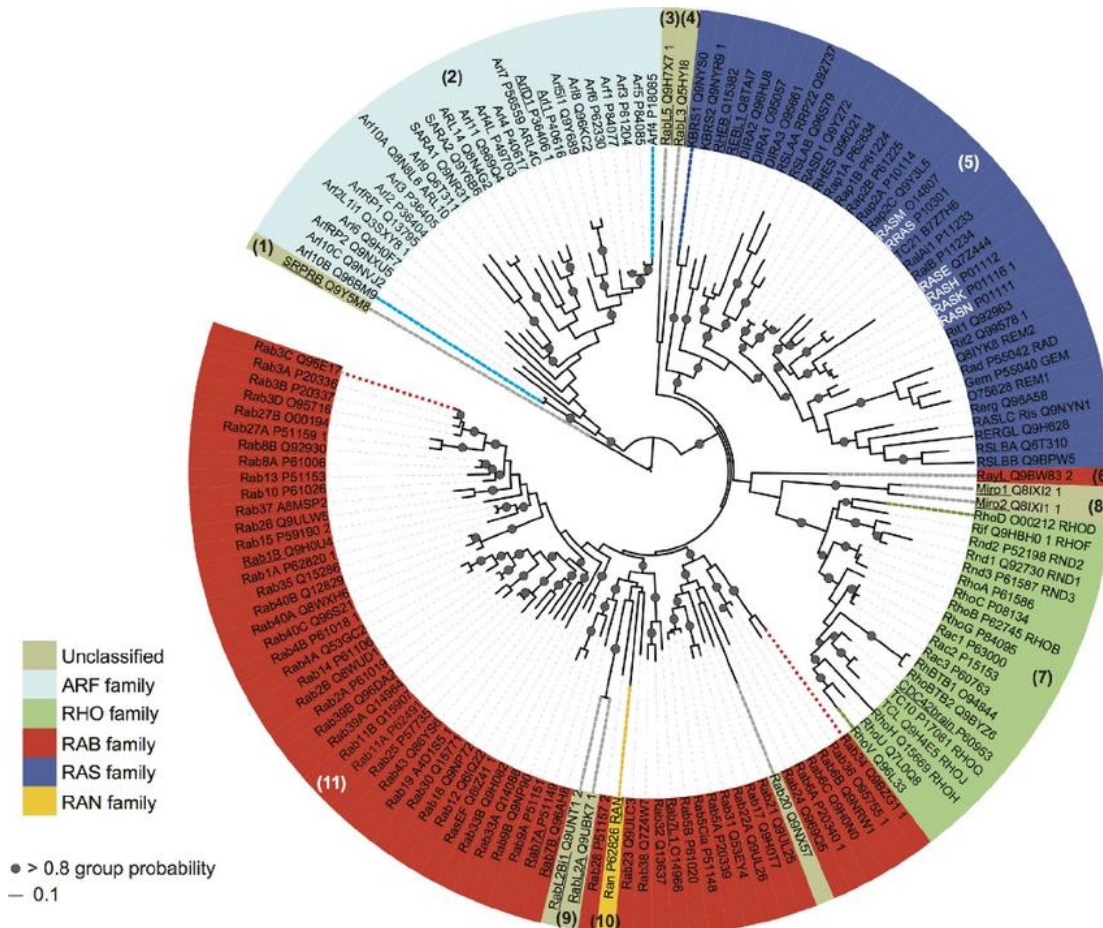
Figure 1. Schema of RAS family Wennerberg et al., 2005. Color code indicate classification adapted with permission from: [Rojas et al, 2012]: RAS family marked as blue; RHO is shown in green; RAB subfamily is marked red; Arf is shown in cian; RAN is shown yellow. Unclassified - beige.

1.2. Structure of RAS proteins

Members of the RAS family are interrelated as they share about 90% of amino acid

sequences. They share almost 100% identical part of the first 1-86 amino acids – effector

lobe, there is ~82% sequence similarity within residues 87-166 region – allosteric lobe, the C-terminal 20 amino acids differ and form a hypervariable region (HVR). Amino acids 1-166 of G domain are responsible for specific interaction with GTP and GDP and essential for hydrolysis of bound GTP to GDP and P1 [Keeton et al, 2017]. Within the G domain there are switch I (SI) and switch II (SII) regions that change in conformation during GDP–GTP cycling and are the main determinants of downstream effector binding [Hobbs et al, 2016].

RAS is located in the intracellular leaflet of the membrane where it functions as a communication hub allowing for extracellular growth factor-dependent signaling to be transmitted to a dozen different intra-cellular signaling pathways, including the classically studied MAPK and PI3K pathways [Downward et al, 2003]. Post-translational lipid modifications (PTM) of RAS proteins are required for their binding to cell membrane and regulators, as well as for activating downstream effects.
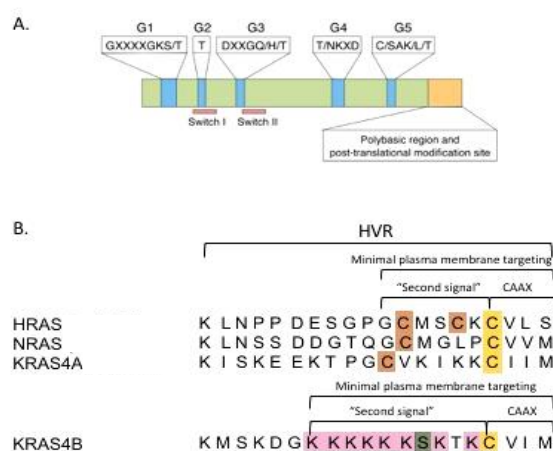
Figure 2. GTPase structure. (A). *Consensus amino acid sequences (G1, G2, G3, G4, G5) are responsible for interaction with GTP/GDP. Polybasic region on the COOH terminus of the protein serves as a post-translational modification site crucial for proper GTPase functioning.* **(B).** *HVRs of the four diffirent RAS isoforms demonstrated. Cysteine residues that undergo farnesylations are marked yellow, palmitilation sites are shown in green. Phosphorilation site at Ser181 is marked blue. Adapted by permission from Springer Nature from: [Ahearn I et al, 2011].*

1.3. Post-translational modifications of RAS proteins.

PTMs occur in HVRs of RAS proteins in sites of the following structure: Cysteine (Cys)-Aliphatic amino acid (A) - Aliphatic amino acid (A) - Any amino acid (X). PTMs comprise a sequence of three reactions: (1) farnesylation at Cysteine residue; (2) proteolytic removal of A-A-X sequence by RCE1 enzyme and (3) carboxymethylation of the exposed Cys residue by isoprenylcystein carboxymethyltransferase. HRAS, NRAS and KRAS4A possess an additional Cystein residue that requires palmitoylation [Christiansen J et al, 2011].

Sequence of PTMs converts RAS from globular hydrophilic to hydrophobic form associated with cell membrane. The enzymes involved in post-translational modifications are well-characterized and there were attempts to use them as potential therapeutic targets [Cox et al, 2010] (Figure 3). The difference in hypervariable regions of RAS proteins underlies the dissimilarity of their functions [Haigis et al, 2008].
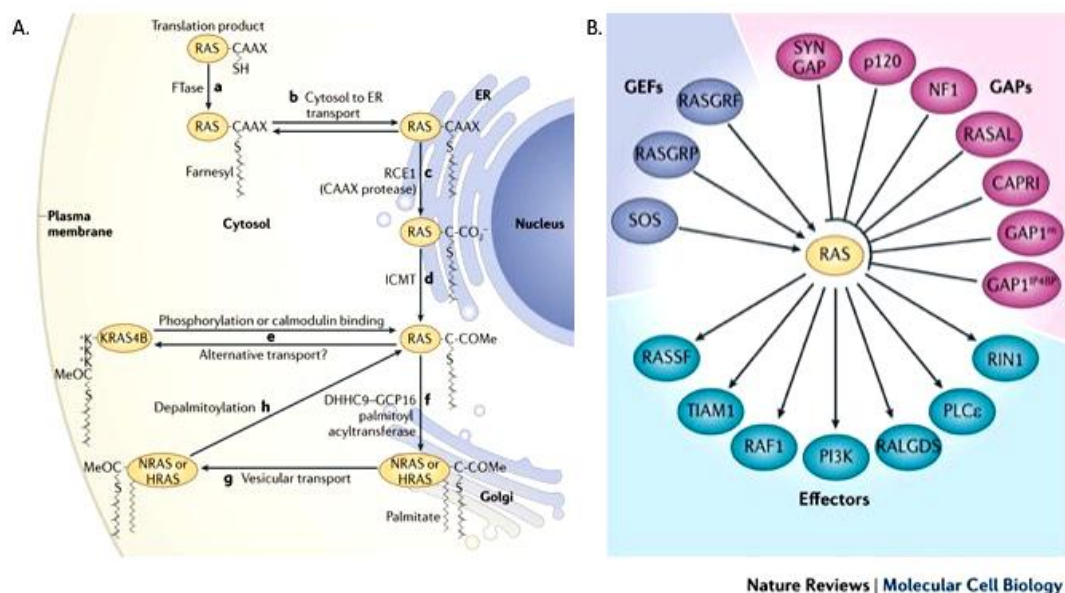
Figure 3. Post-translational modifications and regulation of RAS. Schema of RAS proteins post translation modifications (A) and signaling (B) demonstrates various upstream effectors (GAPs etc) and downstream targets (PI3K etc) involved in RAS pathway. Adapted by permission from Springer Nature from: [Ahearn I et al, 2011].

1.4.   Regulation of RAS pathway

In normal conditions, the activity of RAS is regulated by the ratio of bound GTP to GDP [Cullen et al, 2002]. Upstream signal stimulates GDP-bound form to dissociate allowing its exchange to GTP due to 10 times higher concentration of the latter in the cytosol. When bound to RAS protein, GTP induces a conformational change of the downstream effector(s) binding region thus making RAS proteins active and engaging the downstream target enzyme(s). If bound to GDP, RAS proteins remain inactive. Since RAS proteins serve as transmitters of upstream signals to downstream pathways, they are often called: "molecular switches".
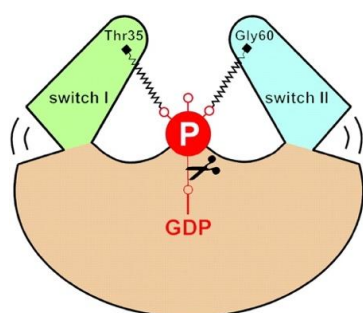
A diagram of the loaded spring mechanism [Vetter et al, 2001].

The GTP/GDP ratio depends on several factors such as guanine exchange factors, nucleotide hydrolysis by GTPase activation proteins. GEfs activate RAS by inducing release of GDP thus allowing GTP to bind, whereas GAPs return RAS into GDP-bound state by elevating the intrinsic rate of GTP hydrolysis. Upstream and downstream regulation of the RAS pathway involves a great number of divergent proteins (Figure 3) [Downward et al, 2003].

1.5.   RAS functions

RAS regulates numerous cellular functions, including "gene expression, proliferation, survival, differentiation, cell cycle entry, and cytoskeletal dynamics" [Downward et al, 2003]. The biological effects of RAS proteins are determined by downstream pathways that they regulate, including the best-studied Mitogen-activated Protein Kinase (MAPK) cascade.

Once activated, RAS proteins directly bind to an active serine/threonine RAF1 protein kinase, which in its turn induces gene expression through the MAPK (also known as MEK) kinase [Downward et al, 2003; Ahearn et al, 2011; Rebollo et al, 1999; Dumphy K et al, 1998]. As a result of MAPK pathway stimulation, several transcription factors such as ELK1, FOS, c-JUN, AP1 (FOS-JUN heterodimer formation) are activated which promotes expression of key cell-regulatory proteins that enable cell cycle progression through G1 phase [Dunn et al, 2005]. A considerable number of studies have shown this pathway to participate in diverse biological processes including negative selection of T cells in the thymus [Daniels et al, 2006] and proliferation of epithelial cells [Hecquet et al, 2002].

Besides RAF1/MAPK cascade, other proteins were demonstrated to interact with RAS directly [Hecquet et al, 2002]. For example, RAS can interact with type I phosphatidylinositol 3-kinases (PI3Ks), which control a large number of downstream enzymes including PDK1 (3-phosphoinositide-dependent protein kinase-1) and AKT and provide a strong anti-apoptotic signaling. Another pathway leading to apoptosis down-regulation through inhibiting the FORKHEAD transcription factors of the FoxO family is RALGDS (RAL guanine nucleotide dissociation stimulator). Some of the most studied pathways are shown in Figure 4.
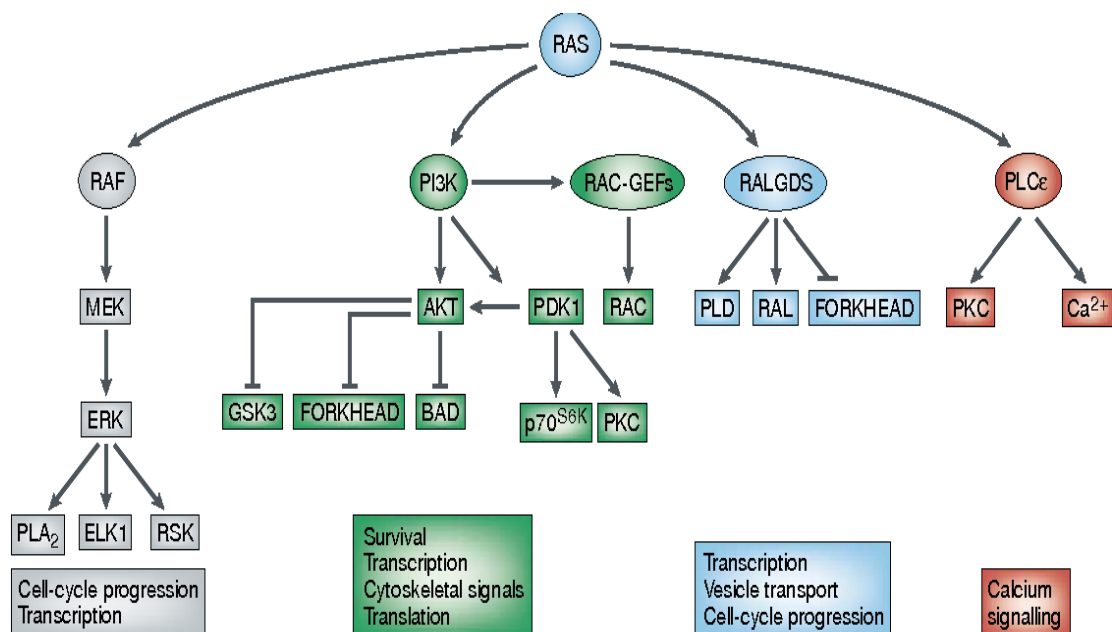
Figure 4. RAS downstream signaling. *When bound to GTP, RAS enters activated state and interacts with downstream targets leading to various effects, including, but not limited to ERK activation (via MAP kinase), generation of second messenger lipids (via PI3 kinase) as well as protein kinase C (PKC) activation and calcium mobilization (via Forehead transcription factors Phospholipase Cε (PLCε). Adapted by permission from Springer Nature: [Downward et al., 2003].*

1.6. RAS pathway in cancerogenesis

Missense mutations in RAS genes are found in nearly "30% of all human cancers, with 98% of the mutations at one of the three mutational hotspots: G12, G13 and Q61 (COSMIC v75)" [Hobbs et al, 2016]. In addition to point mutations which result in defective GAP-mediated GTP hydrolysis and therefore lock the enzyme in the GTP-bound, activated form, other mechanisms of RAS pathway activation in cancer exist: GAP deletion [e.g., loss of neurofibromin 1 (NF1)], Growth factor receptor (EGFR) activation, mutations or amplification of RAS effectors (BRAF, PTEN).
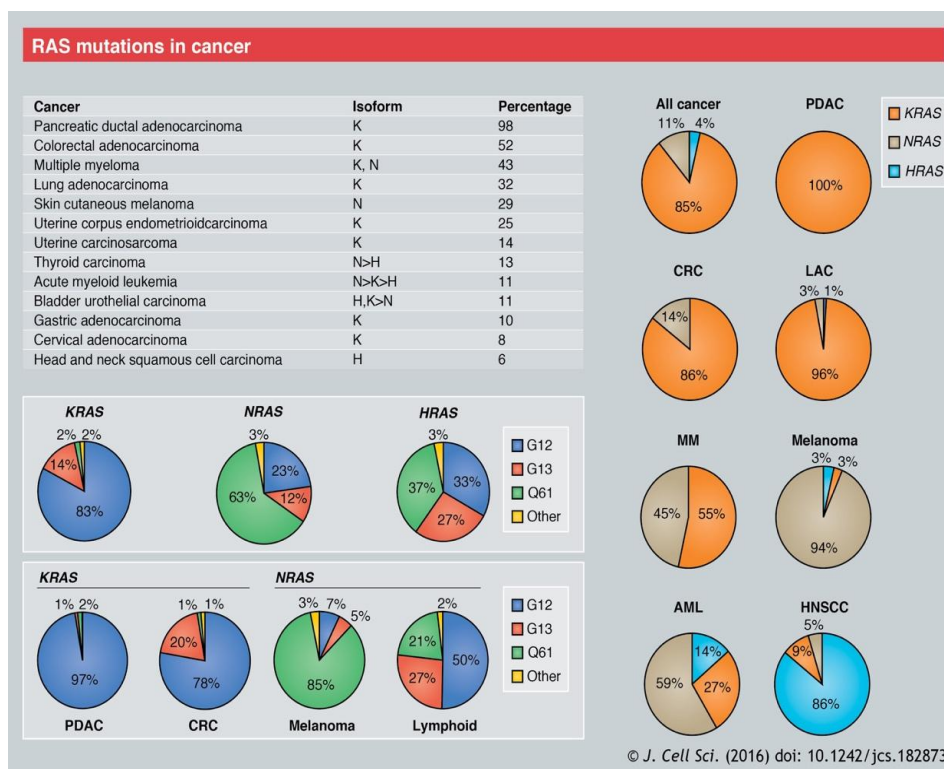
Figure 5. *Frequency of RAS gene isoform mutations in various types of cancers.* *The predominant mutation for pancreatic ductal adenocarcinoma (PDAC), lung and colorectal carcinoma is KRAS, whereas cutaneous melanoma is mostly driven by NRAS [Cox et al, 2014]. KRAS and NRAS almost equally contribute to multiple myeloma development. Predominant isoform for AML is NRAS (59%) with KRAS in the second place (27%). Adapted with permission from: [Hobbs et al, 2016].*

RAS isoforms contribute differently to cancer: KRAS is the most mutated isoform (85%), with NRAS in the seond place (11%) and HRAS in the last place (4%) (Lampson et Al., 2013). Historically the G12V mutation attracted most attention as the 'poster child' for oncogenic RAS but now it was reported that mutations at each of the three missense-mutation hotspots (G12, G13 and Q61) have distinct structural and biochemical defects, equally contribute to carcinogenesis and occur in RAS hotspots with different frequencies (Table 1).

Table 1. Frequency of single-base-change missense mutations in RAS isoforms [Hobbs et al, 2016].

Hot spot	Base substitution	Frequency of mutation		
		KRAS	NRAS	HRAS
Glycine (G) 12	Valine (V)			57%
	Aspartic acid (D)	41%	52%	
Glycine (G) 13	Aspartic acid (D)	89%	50%	3%
	Arginine (R)			85%
Glutamine (Q) 61	Histidine (H)	58%	6%	5%
	Arginine (R)		47%	43%

Various functional outcomes resulting from different mutation hotspots were shown: "G12V mutation leads to a loss of GAP sensitivity, Q61L reduces intrinsic hydrolysis and GAP sensitivity as well as increases nucleotide exchange. G13D decreases GAP-mediated hydrolysis and increases the rate of nucleotide exchange. Q61R shows alterations in switch II structure resulting in impaired GTP hydrolysis" [Hobbs et al, 2016]. There is evidence on the prognostic value that different mutations can have for anti-EGFR therapy in patients with colorectal cancer [Zanella et al, 2015; Van Cutsem et al, 2015, Cousin et al, 2015]. Ambiguous results were shown for pancreatic cancer prognosis: KRAS G12D and G12R were found to be poor prognostic factors [Ogura et al, 2013], whereas another research group showed that G12R alone accounts for an increased survival rate [Faris et al, 2014].

1.7. RAS treatment approach

The history of RAS-guided therapy development is nearly three decades long embracing both significant hopes and just as significant disappointments. Over the last few years there were numerous calls in scientific community to end the pursuit that couldn't yield

an effective drug and focus on other, more promising areas of cancer research. However, there are still a substantial number of groups that have dedicated their careers to solving the issue of successful development of anti-RAS therapy. They have received a significant boost when in 2015 NCI driven RAS Initiative was launched. Many institutes worldwide have since followed this pursuit and several distinct strategies emerged.

The first strategy was to find drugs that inhibit farnesyl transferase [Appels et al, 2005]. Six such drugs demonstrated significant success in preclinical stage and made it to clinical trials (" BMS-214662 (Bristol-Myers Squibb, Princeton, NJ, http://www.bms.com), L778123 (Merck & Co., Inc., Whitehouse Station, NJ, http://www.merck.com), tipifarnib (experimental name, R115777; Zarnestra™; Ortho Biotech Products, L.P., Bridgewater, NJ, http://www.orthobiotech.com), lonafarnib (experimental name, SCH66336; Sarasar™; Schering-Plough Corporation, Kenilworth, NJ, http://www.sch-plough.com), FTI-277 (Calbiochem, EMD Biosciences, San Diego, http://www.emdbiosciences.com), and L744832 (Biomol International L.P., Plymouth Meeting, PA, http://www.biomol.com))". However, these trials ended in one of the biggest failures in history of drug development as every single one failed in human clinical trials due to a low efficiency and toxicity. It was later discovered that "in the absence of a farnesyl tail, another enzyme is able to attack a different fatty tail on RAS, rendering drugs useless" [De La Cruz et al, 2015].

Some researchers, have been looking into targeting RAS protein itself [Zhang et al, 2018]. They used (NMR) spectroscopy for fragment-based drug discovery, a method of finding lead compounds for new therapeutics largely based on achievements in computer modeling [Bauer et al, 2011]. It offered new start for targeting the "smooth, unpocketed surface of RAS proteins". Scientists nowadays liken the technique, called "fragment-based screening", to "constructing a key to fit a lock by cutting one notch at a time". In this way, more than hundred small molecules that bind to KRAS were found, that binding directly to

KRAS between switch I and switch II induce a change in the protein structure and inhibit GEFs-catalyzed KRAS activation. Ample research focused on this strategy is in progress now. [Sun et al, 2012].

Another current approach is based on specific mutations within KRAS and developing an agent specific to hotspots. In 2013 a compound known as G12C was developed to target the corresponding KRAS mutation, which is found in 20% of lung cancers, places cysteine, which easily reacts with various molecules, in place of glycine. This cysteine-modifying inhibitor is now at the pre-clinical stage [Ostrem et al, 2013; Zhu et al, 2014].

One of new avenues in this research area is developing drugs for "personalized medicine," that work in patients with specific RAS mutations. "The new concept is based on employing oncogene-induced senescence (OIS), which is considered a powerful tumour suppressor mechanism. Another group demonstrated a new target - Caveolin-1, which acts as a scaffolding protein to functionally regulate signaling molecules" [Nunez-Wehinger et al, 2014]. The lack of caveolin-1 expression was shown to inhibit oncogenic KRAS (KRasG12V)-induced premature senescence, leading to therapeutic benefit in mice model [Halim et al, 2012].

Chapter 2. Review: CDCP1 as a target for RAS pathway

2.1.   Rationale of research

Another way to target RAS pathway was demonstrated by Professor J. Wells. His group was interested in targeting RAS pathway and the approach they chose was to analyze the surfacome of RAS-driven cancer cells by a comparison with well-characterized non-tumour epithelial cell line MCF10A with the same cell line transduced with KRASG12V. Instead finding a protein with downstream effects on RAS pathway, the idea was to find any protein(s) that may distinguish the cells carrying RAS mutation from the normal healthy cells [Martinko et al, 2018].

Glycoprotein capture and enrichment proteomic method was adapted to quantitatively measure surface proteins levels of expression using SILAC and LC-MS/MS [Hoedt et al, 2014]. After thorough data analysis and eliminating equivocal results, a total of 17 proteins were found to be significantly upregulated in KRASG12V expressing cells, including proteins responsible for cell adhesion, cell-cell adhesion and motion. 13 of these 17 proteins were reversibly influenced after treatment with MEK-inhibitor (i) but not AKTi and EGFRi suggesting MAPK contribution to increased invasiveness, metastasis, and epithelial to mesenchymal transition [Zhou et al, 2017]. As the next step these results were validated *in vitro* using the newly synthesized recombinant monoclonal Abs. To develop Abs, seven top candidates were chosen with at least 2-fold upregulation detected by both mass spectrometry and RNAseq, including CDCP1.Phage display technique was then applied to prepare antibodies [Hammers et al, 2014]. Resulting antibodies were tested according to the recommendation of the Working Group for Antibody Validation. Binding and specificity were confirmed via Flow Cytometry and CRISPRi knockdown, respectively. Using synthesized Abs expression of top seven candidates was assessed in eight cancer cell lines

known to harbour oncogenic RAS mutations, including human Pancreatic Ductal Adenocarcinoma Cancer (PDAC) [Deer et al, 2010]. Only one out of the seven candidates, specifically CDCP1, was found to be overexpressed in all panels of the analyzed cell lines. Anti-CDCP1 antibody, 4A06, was further confirmed to possess an ability to selectively deliver cytotoxic payload to mutant KRAS cells and mediate T cell activation in vitro using NFAT-GFP transduced Jurkat T cell model [Martinko et al, 2018].

2.2. CDCP1 (CUB domain-containing protein 1) overview

Over the recent years, significant interest concentrated on CDCP1 that was identified as a human tumour-associated gene. In 2001 a scientific group in Austria reported that they identified a novel human tumour gene that they dubbed CDCP1 [Scherl-Mostageer et al, 2001]. To identify CDCP1 representational difference analysis and cDNA chip technology were mainly utilized. The report stated that "this gene consisted of eight exons and the upstream region and, interestingly, contained neither a TATA- nor a CCAAT-box upstream of it. Notably, the CpG site was located around the transcription start" [He et al, 2010]. Before its identification, a cleaved form of the CDCP1 protein was described separately as a "78-kDa tyrosine phosphorylated protein observed after the loss of integrin alpha-6,beta-4-mediated human keratinocytes adhesion" [He et al, 2010].

2.3. CDCP1 structure

The CDCP1 protein is a Type-I transmembrane glycoprotein. It is also known as SIMA135, gp140 and, more recently TRASK (Transmembrane protein associated with Src kinases). It is 836 amino acids long and consists of a 29-amino-acid-residue terminal signal peptide, an extracellular domain, a transmembrane domain and a cytoplasmic domain containing nearly 150 amino acids [Uekita et al, 2011].

- The first domain to review is extracellular, and it consists of CUB domains (for complement C1r/C1s, Uegf, Bmp1). The CUB domainis a structural motif of about 100 residues characterized by an immunoglobin-like fold and it is most likely involved in protein–protein interactions [Dirican et al, 2016]. The CUB domains were reported to take part in embryogenesis and organogenesis. Full-length CDCP1 undergoes protease cleavage in cancer cells and keratinocytes. The cleavage sites are located in the extracellular domain at Arginine-368, Lysine-369 (serine protease cleavage sites) and at Lysine-277 (trypsin cleavage site). Upon cleavage, a smaller C-terminal membrane protein is generated, also described in literature as the "70–85-kDa fragment of CDCP1" [Yang et al, 2015; Wortman et al 2009; He et al, 2018].

- Cytoplasmic domain of CDCP1 includes five conserved residues of tyrosine that can be phosphorylated by Src family kinases. Two proline-rich stretches potentially capable of binding Src homology 3 (SH3)-containing proteins are located in this domain as well [Yang et al, 2015; Wortman et al 2009; He et al, 2018].

- CDCP1 contains 14 putative N-glycosylation sites.
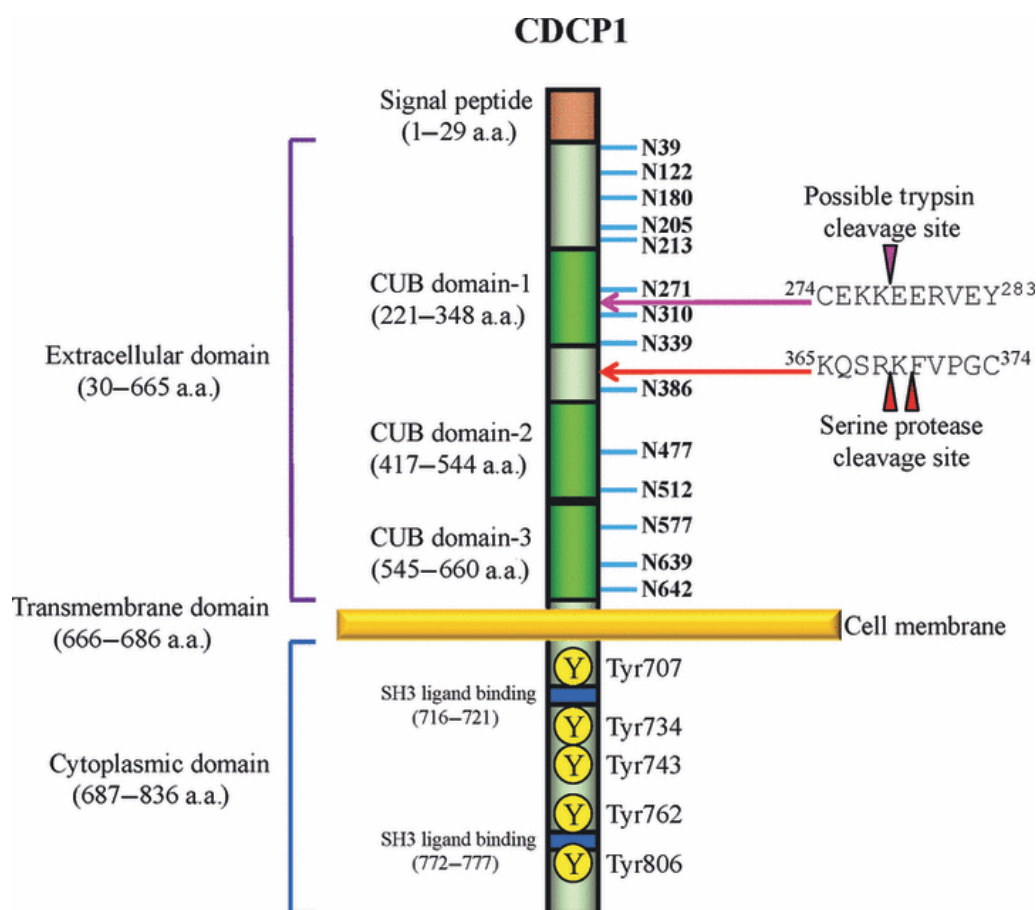
Figure 6. Graphic representation of the CDCP1 structure. *CDCP1 is composed of cytoplasmic domain, transmembrane domain, extracellular domain and a short signal peptide. Extracellular domain of CDCP1 consists of three CUB domains. It also includes several protease cleavage sites: R368, K369 (serine protease cleavage sites) and at K277 (trypsin cleavage site). Adapted with permission from: [Uekita et al, 2011].*

The CDCP1 gene was "mapped to chromosome 3p21-p23 using fluorescence *in situ* hybridization (FISH)" [Zubacova et al, 2011]. After that the expression profiling was performed via RT-PCR with various cell lines and "specifically designed laser capture micro dissected colon cancer biopsies, the CDCP1 mRNA was found to be approximately 6 kb and to be overexpressed in some human cancer tissues, such as colon and lung" [Zeng et al, 2017; Kurosawa et al, 2016; Andre et al, 2006]. Also this mRNA was found to be present in breast cancer tissues. [Scherl-Mostageer et al, 2001].

2.4. CDCP1 function

CDCP1 was shown to play a significant role in malignant progression in a number of cancers, including kidney, lung, ovary, colon, rectum and pancreas [He et al, 2016; Kubelac et al, 2015]. It also contributes to survival, migration and anchorage-independent cell survival and was found to contribute to anoikis resistance which is a "form of programmed cell death occurring in the anchorage-dependent cells when they detach from surrounding extracellular matrix" [Talukdar et al., 2018]. Inhibition of this type of apoptosis is critical for tumour metastasis [Liu et al, 2011; Chiu et al, 2017; Nakashima et al, 2017; Wright et al, 2017].

CDCP1 expression is driven by activating upstream signaling pathways such as EGFR and RAS/MEK [Dong et al, 2012]. Activation of EGFR stimulates activation of RAS and inhibits proteasome-dependent degradation of CDCP1. As a result, CDCP1 accumulates and its recycling to the cell membrane increases. Activating RAS proteins significantly promotes CDCP1 mRNA and protein expression through stimulating MEK signaling pathway. Moreover, hypoxic conditions, a common microenvironment for cancer cells, are known to contribute to CDCP1 overexpression and activation (Figure 8) [Uekita et al, 2014].

CDCP1 can directly bind to HER2 receptor, driving tumourogenesis and promoting resistance to trastuzumab (anti-HER2 monoclonal antibody) therapy [Alajati et al, 2015; Wright et al, 2016]. Furthermore, CDCP1 contributes to doxorubicine resistance and resistance to anti-EGFR therapeutics gifitinib and cetuximab [Karachaliou et al, 2018; Chiu et al, 2017].

Other downstream effects of CDCP1 are due to activation of PKCδ and Src signaling pathways. As a major substrate of Src family kinases (SFKs), it mediates migration and resistance to therapy. Src-dependent pathways activate PI3K/Akt signaling to promote cell survival. Importantly, CDCP1 affects only the detached cells. SFKs are the key regulators of various cell functions, including cell cycle and proliferation, cell adhesion, cell migration

under the control of extracellular stimuli. Numerous studies demonstrated elevated activity of SFKs or increased protein expression in a broad panel of human cancers. The elevated activity of SFKs frequently correlates with the higher rates of tumour development, methastatic potential and poor outcomes in general. [Ingley et al, 2008; Leroy et al, 2015; Li et al, 2010; Shattil et al, 2005; Pace et al; 2006].

Lately it has been shown that CDCP1 cleavage is necessary for its activation, and it stimulates CDCP1 homodimerization. Full length CDCP1 (flCDCP1) can bind to Src or PKCδ with no downstream effects. Cleaved CDCP1 (cCDCP1) can form homodimers, allowing both Src and PKCδ bind to cCDCP1 in close proximity to each other and facilitate phosphorylation of protein kinase C δ (PKCδ) by Src kinase, leading to migration and cell invasion (Figure 7). In this case cleaved CDCP1 dimers act as "docking stations" [Wright et al, 2016].
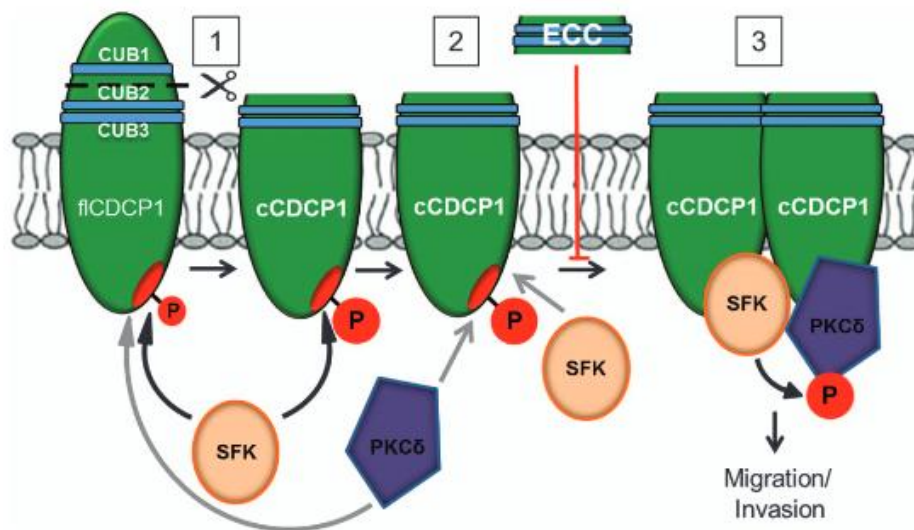
Figure 7. Dimerization of CDCP1 as an important factor of CDCP1 activation. Full length CDCP1 (flCDCP1) binds to Src or PKCδ with no downstream effects. Cleaved form of CDCP1 (cCDCP1) can form homodimers, allowing both Src and PKCδ to bind to cCDCP1 in close proximity to each other and facilitate phosphorylation of protein kinase C δ (PKCδ) by Src kinase, leading to migration and cell invasion. Adapted with permission from: [Wright et al, 2016].

CDCP1 is also known to regulate lipid metabolism by reducing cytoplasmic lipid droplet (LD) abundance and promoting fatty acid oxidation (FAO) and oxidative phosphorylation. Disrupting lipid metabolism most likely contributes to progression and cell migration in triple-negative breast cancer [Wright et al, 2017] and some other cancers [Luo et al, 2017; Huang et al, 2015; Aguirre-Portoles et al, 2017] as the required amount of energy is produced.
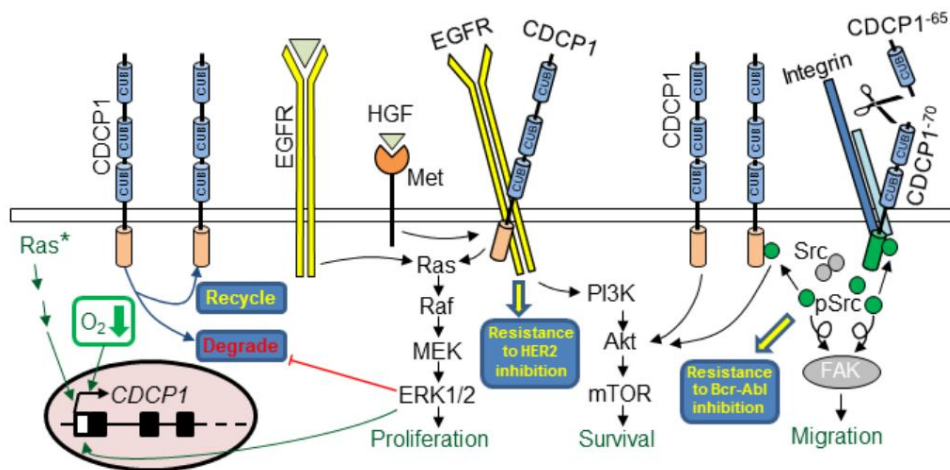
Figure 8. CDCP1 signaling pathway. Effects of CDCP1 include proliferation, survival and migration. It also reported tomediate resistance to chemotherapies. Hypoxic conditions inside the tumour increase CDCP1 expression. Adapted from: [He et al, 2015].

2.5. CDCP1 expression in normal tissues

The expression of CDCP1 in human tissues was studied by Northern blot. Moderate levels of expression were observed in kidneys, small intestine. A lower signal was detected in peripheral blood T cells. A borderline specific signal was present in skeletal muscles, colon, placenta and lung. mRNA was not detected in several organs like heart, spleen, liver and brain [Hooper et al, 2003].
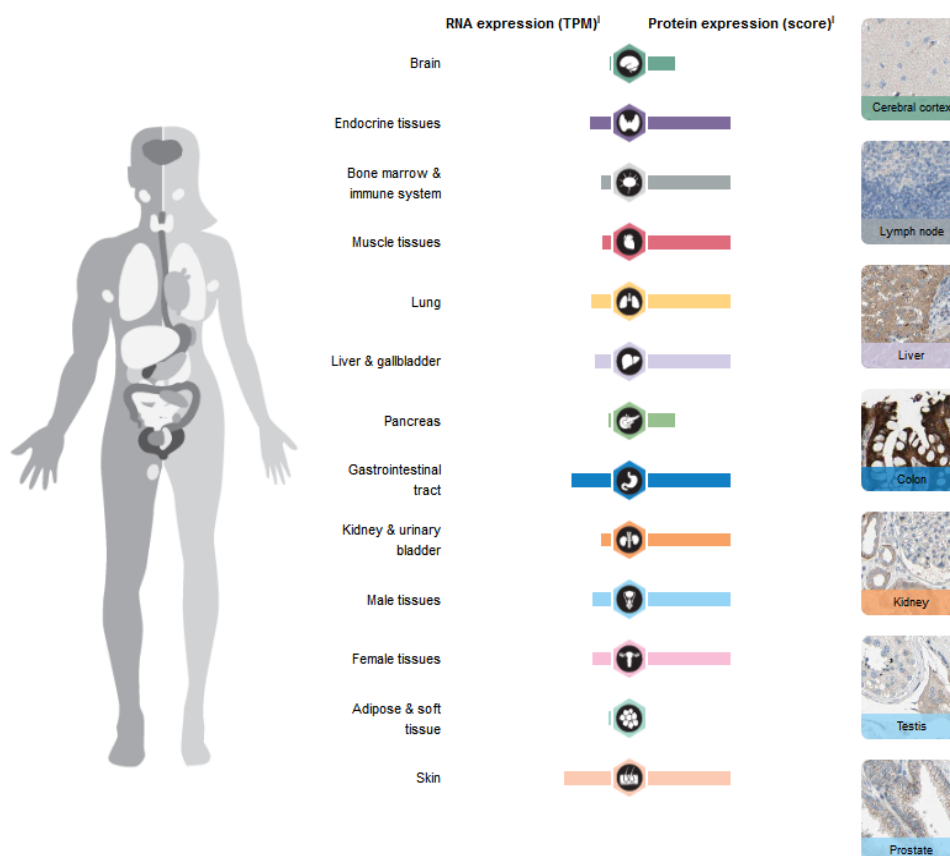
Figure 9. CDCP1 expression in various human tissues. (Obtained from proteinatlas.org)

Moreover, CDCP1 was proved to be moderately expressed on cells with both mesenchymal stem cell and neural progenitor cell phenotypes, which opens a possibility to apply CDCP1 in the field of stem cell research [Vincent et al, 2016].

2.6. CDCP1 expression in cancer

CDCP1 protein levels were assessed by IHC in samples of biopsies derived from subjects with colon and breast cancer of various ages and sexes with the use of polyclonal and few monoclonal antibodies. The results demonstrated significant levels of CDCP1 expression in colon cancer with an important observation that the connective tissues were not stained beyond statistically insignificant levels. A similar pattern of CDCP1 expression was also observed in about 95% of breast cancer samples. In addition to these diseases, cell

samples from other tumours were tested and "predominant staining of epithelial cells derived from a lobular mammary carcinoma was shown" [Buhring et al, 2004]. These data complied with the previous observations regarding mRNA levels. Further studies demonstrated elevated levels of CDCP1 in samples from some aggressive epithelial cancers. Most importantly, these levels of CDCP1 were clearly shown to directly correlate with "poor prognosis, higher relapse rate and occurrence of metastases" [Buhring et al, 2004].
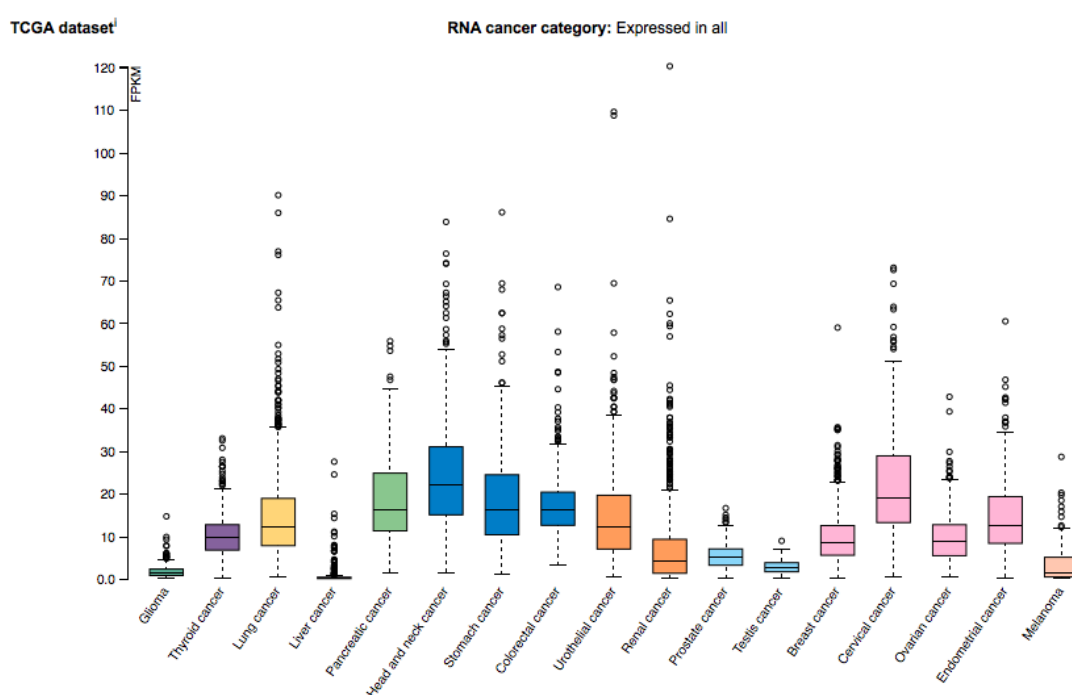
Figure 10. CDCP1 RNA expression in different cancers. The Cancer Genome Atlas dataset. (Obtained from proteinatlas.org)

2.7.   Current clinical applications based on CDCP1

CDCP1 has proved to be a potent biological marker deserving to be investigated as an effective target for anti-cancer therapy. To do that, the main goal would be to identify the desired mode of action to develop useful therapeutics. Clearly, despite significant advances in

understanding the CDCP1 role, there is still very little actual benefit from this knowledge to the clinical diagnostics and treatment of cancer. Many groups are now trying to shed light on these questions and synthesize potent anti-CDCP1 antibody.

25A11 for Metastatic Prostate cancer. The first anti-CDCP1 antibody to test was 25A11. In cell culture experiments, it was shown to inhibit prostate cancer invasiveness [Siva et al, 2008].

Treatment with the same antibody coupled with cytotoxin saporin (a ribosome-inactivating toxin) resulted in inhibition of methastatic prostate cancer in a mouse xenograft model. This was a significant milestone in CDPC1 research. In a preclinical study 25A11 was shown to inhibit tumour cell migration and invasion in cultures. Further studies were conducted and 25A11 was demonstrated in fact to internalize. So, when conjugated to saporin, 25A11 was shown to inhibit primary tumour growth. Further observations demonstrated that "size and incidence of lymph node metastases also decreased in a prostate cancer spontaneous metastatic tumour model" [Siva et al, 2008]. Today 25A11 antibody is commercially available for flow cytometry, immunohistochemistry (IHC) and ELISA application.

RG7287 for metastatic lung cancer. Another therapeutic antibody to test was RG7287. Kollmorgen et al reported that: "Prolonged RG7287 treatment induced internalization and down-regulation of CDCP1 in several cancer cell lines. In xenograft models with endogenous CDCP1 expression, RG7287 treatment resulted in significant tumour growth inhibition concomitant with substantially reduced CDCP1 levels." [Kollmorgen et al, 2013].
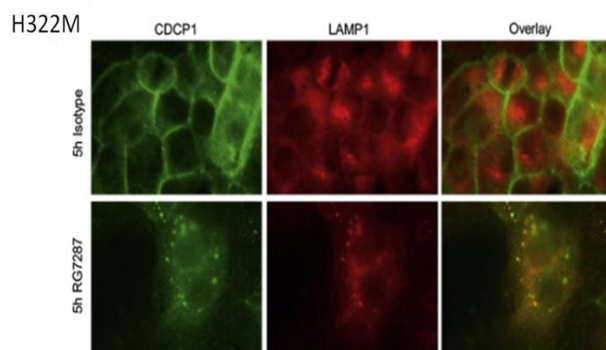
Figure 11. Effect of anti-CDCP1 antibody RG7287. H322M (human lung, cervical node metastasis) cells were cultured on fetal calf serum-coated glass coverslips. RG7287 antibody or human isotype control were applied for 5 h at concentration 10 µg/ml. The cells were stained for CDCP1 and Lysosomal-associated membrane protein 1 (LAMP1), a protein associated with high metastatic potential. Adapted from: [Kollmorgen et al, 2016].

41-2 for prostatic cancer. Another monoclonal antibody, 41-2, was used to study extravasation step of metastasis on prostate cancer tumour cell line expressing CDCP1. 41-2 was confirmed to efficiently inhibit tumour extravasation, underscoring the functional importance of CDCP1 during this process. Even single treatment with mAb 41-2 dramatically decreased dissemination of PC3-hi/diss cells from primary tumours. Moreover, this group provided insights into CDCP1 functions as a pro-survival molecule in the metastatic cascade [Deryugina et al, 2009]. No further preclinical or clinical studies with neither 41-2 nor RG7287 antibodies were reported.

4A06 for RAS driven cancers. Last but not least, anti-CDCP1 antibody 4A06, developed for testing CDCP1 expression on cancer cell lines and confirmed to be able to selectively deliver cytotoxic payload to mutant KRAS cells and mediate T-cell activation was shown to have high affinity to CDCP1 receptor [Martinko et al., 2018]. The potential of this antibody as a diagnostic tool and a radio therapeutic agent will be demonstrated and discussed in greater detail in the following chapters.

Concluding it is well known that the migration of tumour cells into blood stream is the first and crutial step of cancer metastasis. The presence of tumour cells in circulation was clinically observed to be a prognostic factor for poor overall survival in patients with various types of cancer. Overall, CDCP 1 has a significant potential as it is expressed in tumour tissues and plays a functional role in tumour metastasis and migration. Taking the aforementioned into consideration, this protein represents a valuable target for both therapeutic and diagnostic studies. Antibody treatment that downregulates the function of CDCP1 or destroys tumour cells would have significant clinical relevance.

Chapter 3. Antibodies for imaging and therapy in cancer research.

3.1.   Overview of basic structure and function

Antibodies (Abs) are the secreted form of the receptor of B cells, i.e., an antibody is identical, in terms of its specificity, to the B-cell receptor of the cell that secretes it. The only difference is a portion of the C-terminus of the heavy-chain region, which is constant. In the B-cell receptor the C-terminus is a hydrophobic sequence that is anchored to the membrane, while in antibodies it is a hydrophilic sequence. Antibodies are soluble and are secreted in large quantities making it relatively easy to obtain and study them [Alberts et al, 2002; Janeway et al, 2001].

An antibody consists of three parts of approximately same size, connected by a tether [Grawe et al, 2017]. These molecules carry out a dual task, binding to a wide variety of antigens and interacting with a limited number of effector molecules and cells. All antibodies are designed in the similar way and the term immunoglobulin is used for all of them [Valent et al, 2016].

There are two types of light chains, lambda (λ) and kappa (κ). "In different organisms, the ratio of chains differs. In mice, the κ to λ ratio is nearly 20:1, in humans it is close to 2:1 and in cows it is reversed and equals 1:20" [Li et al, 2007]. The class, and therefore the effector function, is defined by the structure of antibody's heavy chain. There are five main heavy-chain types that define classes of antibodies: immunoglobulins M, D, G, E, and A. IgGs are most relevant for cancer research [Janeway et al, 2001; Redey et al, 2008].

Antibodies are frequently subdivided into antigen binding (Fab) and constant (Fc) fragments. The Fab contains the variable region, which consists of three complementarity determining regions (CDRs) that form the antigen binding site of the antibody and provide

for antigen specificity. The Fc fragment enables antibodies to link to immune effector cells (Figure 12) [Louis et al, 2010].
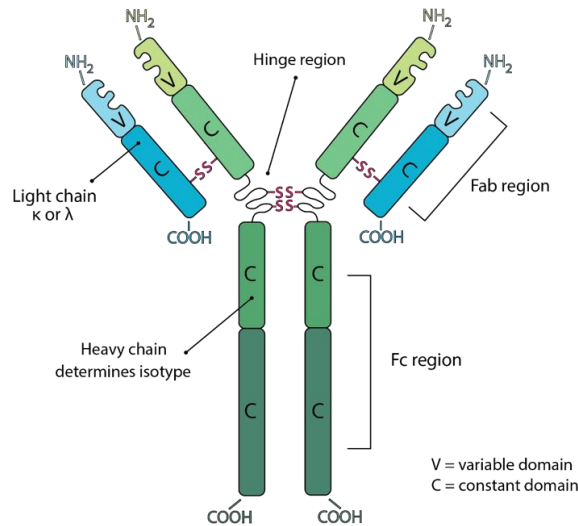
Figure 12*. **IgG structure and function.** (Obtained from: https://bxcell.com/antibody-structure/).*

Functional subtypes of IgG, mainly IgG1 and IgG3, are responsible for the activation of the complement pathway. The binding of two or more IgG molecules to cell surface (antigen) activates the complement system through high-affinity binding of the C1 complex to the Fc region and a complement system cascade. This results in developing the pores by the membrane attack complex (MAC) on the cell surface and, ultimately, cell lysis [Dunkelbreger, et al, 2010]. Chemotactic complement molecules C3a and C5a lead to recruitment and activation of immune cells (macrophages, neutrophils, basophiles and others) [Zipfel et al, 2009].

A lot of attention focused on antibodies' ability to activate multiple pathways such as RAS/MAPK, mTOR and EGFR to name a few, that are critical in cancer development and

can provide unique treatment and diagnostic, as well as prognostic opportunities [Johnson et al, 2006; Nishio et al, 2015; Sashacharyulu et al, 2012; Troiani et al, 2014].

3.2.   Classification and development

Polyclonal Antibodies. The first antibodies used for cancer research were produced by immunizing an animal (usually a mouse) with human tumour cells or cell extracts. After harvesting, a variety of antibodies against a wide spectrum of antigens was obtained, some of which were "tumour specific". Since these antibodies were derived from many B-lymphocyte clones, the term "polyclonal" is used to describe them. Notably, substantial variation occurred when this production method was used [Nakazawa et al, 2010].

Monoclonal Antibodies. In 1975, Kohler and Milstein developed a method for selecting clones of cells that produced pure antibody against a single antigen [Kohler et al, 1975]. Animals were immunized with an antigen source, as in the case of production of polyclonal antibodies. Required cell clones were then grown in artificial cell systems or animals to produce large amounts of pure antibody. This allowed for mass production of antibodies for clinical use [Backer et al, 1988].

Fab' Fragments. Smaller molecules tend to get clear faster, and this observation has led to the development of a technique, whereby whole antibodies are split into antibody fragments which maintain immunoreactivity. Given the fact that the specificity of antibody binding depends on the variable region of the IgG molecule, elimination of the constant region should produce faster clearance without compromising affinity. Fab' fragments consist of variable regions of one heavy chain (VH) and one light chain (VL), while F(ab')2 fragments consist of two Fab(v) fragments connected at the hinge region. They are approximately 30 and 60%, respectively, of the molecular weight of intact antibody. These fragments are cleared from non-tumour sites more quickly due to their smaller size and also

move faster through extravascular space into the interior of the tumour [Nisonoff et al, 1960].

Chimeric Antibodies. Another approach to reducing the amount of mouse protein in an antibody is to fuse the variable region of murine monoclonal antibody of interest to the constant region of human antibody, either chemically or using genetic engineering techniques. Resulting antibodies were named "chimeric". Their antigenicity is similar to that of antibody fragments [Morrison et al, 1989].

"Humanized" antibodies were developed through genetic engineering techniques by grafting the complementarity-determining regions of mouse antibodies into human molecules. hAbs are expected to have antigenicity similar to FV fragments while retaining other characteristics of a whole antibody [Mayhofer et al, 2018].

Human Antibodies. Antigen-stimulated human B lymphocytes from cancer patients are modified and grown in media that allows harvesting high-purity antibody. Low to none antigenicity was confirmed in clinical trials, in which no antigenic responses were detected in patients receiving multiple injections of human antibodies [Steis et al, 1990].

Bifunctional Antibodies. Another modification is the development of bifunctional antibodies that have an ability to bind to tumour-associated antigens as well as to a radiolabeled ligand. This development was fundamental for radiolabeling in which the unlabeled antibody is injected first, followed by injection of the labeled ligand after clearance of unbound antibody from the blood pool. It significantly decreases background, allowing detection of small lesions, for example enhanced detection of liver lesions using Indium-111 [Stickney et al, 1991].

3.3. Scientific and clinical applications

Antibodies in modern science are used therapeutically both as biological agents for direct effect and as a tool for targeted delivery of other active molecules to specific sites. In addition to that, there is a growing number of studies demonstrating application of antibodies in the field of molecular imaging, where they are labeled with various dyes, proteins and isotopes for further visualization.

Direct therapeutic effect of antibodies is achieved by activating complement via mAb opsonization of tumour cells that elicit immune response. This process starts by engagement of antibody receptors on immune effector cells after activation of complement. Complement was reported to play a significant role in modulating the anti-tumour function of many antibodies by complement/antibody-dependent cytotoxicity and through the effects it indirectly exerts on tumour microenvironment. Notably, complement activity can have certain negative effects and the balance of such effects and treatment efficacy remains an important issue to be resolved [Rogers et al, 2014].

Another type of Ab-induced tumour cell killing happens as a result of effects on tumour cell signaling. Tumour signaling is affected when antibodies interfere with growth signaling through binding with membrane receptors. Abs can also neutralize cytokines crucial for cell proliferation. This observation led to many pre-clinical studies aiming to specify targets that could be validated as clinically relevant. One of the most important targets is the EGFR, which is overexpressed in a number of different oncological diseases. During binding to a ligand, EGFR receptor dimerization occurs which activates tyrosine kinase domain and, via MAPK pathway, promotes cell proliferation and migration. This was exploited therapeutically during development of Cetuximab – a "chimeric EGFR-specific IgG1 monoclonal antibody which induces cell cycle arrest and apoptosis in tumour cells by blocking ligand binding and receptor dimerization" [Redman et al, 2015].

Antibodies can provide for indirect therapeutic effect as well, by serving as delivery systems carrying isotopes and/or drug conjugates (ADCs). Ibritumomab, a mouse anti-CD20 antibody, can serve as an example of isotope-carrying model. This radiotherapeutic was approved a decade ago for treatment of NHL. Moreover, it showed efficacy in Rituxan-resistant lymphoma due to massive focal irradiation of the tumour cells. Another example of ADC is Gemtuzumab, which is an anti-CD33 (a common marker of myeloid leukemic blast cells) recombinanthumanized monoclonal antibody. The antibody is linked to calicheamicin and was the first out of the two ADC approved by the FDA for use in patients with relapsed AML. Sadly, this antigen is also expressed on myeloid lineage cells and Ibritumomab use was accompanied by significant adverse effects, so it is currently withdrawn. Serious side effects are an "Achilles' heel" of ADC systems as only two ADCs out of hundreds reported in pre-clinical settings reached patients [Pathak et al, 2012].

Another application for antibodies is molecular imaging. It is a growing field aiming to expand the role of antibodies in oncology by adding research and diagnostic components to it. Antibodies are now considered as a robust molecular imaging tool to interrogate cell surfaces *in vivo*. Identifying and researching the important biomarkers as targets for imaging laid the ground a new generation of mAbs optimized for *in vivo* visualisation. Progress in molecular visualization and availability of new and robust radionuclides provide for a broader implementation of immuno- SPECT and PET. There is an agreement in the clinical and scientific communities that "Abs imaging can provide a sensitive, noninvasive means of molecular characterization of cell surface phenotype *in vivo"* [Wu et al, 2008]. Therefore, progress in this area can be beneficial for diagnosis, prognosis and therapy selection as well as monitoring of treatment in cancer.

3.4.   Development of radiolabelled antibodies for diagnostics and therapy of cancer

In the 90s FDA approved the use of a radiolabelled antibody in patients with cancer for diagnostic purposes. It was CYT-103 (OncoScint OV/CR) labelled with Indium-111**.** This antibody is specific to a tumour-associated glycoprotein TAG-72 of murine origin previously found in several mucin-producing adenocarcinomas [Markowitz et al, 1993]. After this advance, the field of radiolabelled antibodies expanded and soon the first therapeutic success using radiolabelled antibodies was reported in the treatment of lymphoma [Press et al, 1999]. Since then, radiolabelling techniques became well-established and radiolabelled antibodies are now an accepted clinical and laboratory reality. Treating solid tumours represents a current challenge since they are resistant to radiations and, due to a low accessibility to large molecules, keep clinical efficacy of Abs at a low level. However, radiolabelled antibodies used in minimal or small-size metastatic disease demonstrated significant clinical efficacy that merits further research [Kohler et al, 1975].

Recombinant antibodies have shown "considerable potential for increasing the therapeutic index of radiolabelled antibodies" [Chames et al., 2012]. In many cases the pre-clinical studies end up with successful translation into clinical trials and wide application. Furthermore, a significant number of new radioisotopes, such as Lutetium-177 and Zirconium-89, with favourable properties have further improved the safety of radiotherapy using antibodies. Some new research suggests that "alpha particle and Auger electron emitters can be used to target microscopic clusters of tumour cells, opening the possibility to kill the "last tumour cell", which is the "Holy Grail" in cancer therapy". Several pre-clinical and clinical studies have confirmed the potential of this approach [Aghevlian et al, 2017].

3.5.   Radiolabelling

The procedures of radiolabelling antibodies are well-established. The major factors are considered to be: the choice of radionuclide and the method of conjugation. While at the first stage of development in 80s the iodination techniques were prominent, currently the major emphasis is put on the methods of conjugating metallic radionuclides using chelating agents as it is a proven technique of producing clinically useful radiolabelled antibodies.

Choice of the Isotope. In the process of choosing an isotope for biological application several factors should be considered; count rates should be high enough, the radiation dose should be safe for the patient and the efficiency of interaction with the gamma camera crystal should be sufficient. As the interest to the field of antibody-based therapy in oncology grew, so did the number of studies focused on the development of diagnostics for these treatments in particular nuclear imaging agents. In addition to general factors, the major specific requirement in the construction of antibody-based nuclear imaging agents is similar physical half-life of the radioisotope and the half-life of the immunoglobulin [Zeglis et al, 2011]. Antibodies have somewhat slower pharmacokinetics and usually need days to reach their peak biodistribution. This makes various isotopes from ^{111}In to ^{99m}Tc with half-lives from several hours to several days good candidates for antibody-based nuclear imaging.

Each of these isotopes has both advantages and disadvantages. ^{64}Cu was successfully used for antibodies in multiple pre-clinical studies in smaller animals such as mice and rats. The chemistry of the procedures was worked out very well and the outcomes were promising, but during translation into clinic its 12.7 h half-life was proved to be ineffective due to the slower pharmacokinetic conditions of imaging in human body [Anderson et al, 1992; Cai et al, 2007].

Another promising candidate - ^{86}Y - had a number of successful applications in preclinical trials but its short half-life was a limiting factor for human imaging in addition to

decay characteristics and quite laborious and expensive radionuclide production and purification.

In contrast to these isotopes [124]I has long been the best candidate for ImmunoPET due to a near-ideal half-life that resulted in optimal antibody-based imaging [Verel et al, 2004]. But recently its value was questioned because of low resolution, high energy of its positrons, only 24% emission rate of positions, and dehalogenation of [124]I-labelled antibodies *in vivo*. *These negative factors* combined substantially limit its clinical potential. Iodine-123 is chemically identical to Iodine-131 and close to Iodine-124 but has no beta emission and a much shorter half-life (13 hours). Its efficiency with the gamma camera is almost as good as that of technetium-99m. Unfortunately, Iodine-123 is quite expensive and is not readily available.

Nowadays, there are two more isotopes that are considered as potentially optimal candidates - [111]In and ^{67}Ga as both of them have favourable physical half-lives and behaviour for antibody-based imaging. However, at this moment SPECT limitations lead to the growing interest in the clinical implementation of immunoPET compaired to immunoSPECT. [Chan et al, 1987].

It would be prudent to mention a number of studies done with ^{99m}Tc, which was judged to be a poor choice for this field due to limitations based on used modality (SPECT) and relatively short half life. [Sapienza et al, 2002].

The task to select a better suited isotope for antibody-based imaging lead several groups in investigating [89]Zr as imaging agent. [Diikers et al, 2009; Munnink et al, 2010]. [89]Zr has beneficial characteristics for this approach. Its half-life of 78.4 h is better suited to antibody-based imaging and it is logistically less challenging in clinic as it is safer and cheaper. In addition, it's stabililty is a factor as well is the fact that it residualizes in tumours more effectively than most other probes [Perk et al, 2005].

The recent addition to the list - the ^{177}Lu radionuclide - has attracted a lot of attention in academic, commercial and clinical communities as a viable candidate for a variety of therapeutic and diagnostic procedures. Currently ^{177}Lu has became a key therapeutic radionuclide for preclinical studies with a rapid translation into clinic. The interest in ^{177}Lu in cancer research has developed from significant advances in molecular and cell biology applicable for targeted molecular therapies. Its physical characteristics such as mostly β^- particles emission with the range of E $_{\beta(max)}$ from 176 to, predominantly, 497 keV (78.6 %) and some low-energy gamma photons [Ashutosh et al, 2015].

^{89}Zr isotope stays intracellularly after the internalization of antibody-antigen complex which allows radioactivity to gather in tumour cells, increasing concentration in comparison to other tissues. Fast clearance of non-specific activity from the body, results in superior contrast images. Due to relatively long half-life of ^{89}Zr it becomes possible to perform imaging several days after injection. Delayed visualization allows a reduction of background signal and results in noticeably improved images.

There are several examples of success in using ^{89}Zr immunoPET to monitor therapy effect and as a prognostic factor. One of the examples is the study in ovarian cancer envoling ^{89}Zr-bevacizumab treatment in combination with heat shock protein 90 inhibitor (NVP-AUY922). HSP90 inhibition has a profound antiangiogenic effect and results in a decrease in the VEGF secretion. Therefore, ^{89}Zr-bevacizumab works as biomarker for the HSP90 inhibition. This approach provides means for quantifiable visualization of early antiangiogenic response *in vivo* [Nagengast et al, 2010].

Table 2. Clinically available radioisotopes for antibody labelling.

Radionucleide	$t_{1/2}$	Average β^+ Enrgy/ I $_{\beta+}$ (%)	Principle γ Emissions/ I$_\gamma$ (%)	Optimal Production Method	Typical Chelators	Theranostic Partner Isotope
^{89}Zr	78.4 h	396keV/ 23%	909 keV/ 99%	Cyclotron	DFO HOPO DOTA	-
^{64}Cu	12.7 h	278 keV/ 18%	-	Cyclotron	NOTA DOTA TETA SAR family	^{67}Cu
^{86}Y	14.7 h	660 keV/ 32%	1076 keV/ 83% 628 keV/ 33% 1153 keV/ 31% 777 keV/ 22% 1921 keV/ 21% 1854 keV/17%	Cyclotron	DOTA DTPA	^{90}Y
^{52}Mn	5.6 d	242 keV/ 29%	1434 keV/ 100% 935 keV/ 95% 744 keV/ 17%	Cyclotron	DOTA	-
^{55}Co	17.5 h	570 keV/76%	931 keV/75% 1409 keV/ 17%	Cyclotron	DOTA HBED TETA NOTA	^{58m}Co
^{152}Tb	17.5 h	1140 keV/ 20%	-	Proton-induced spallation	DOTA	^{161}Tb
^{90}Nb	14.6 h	620 keV/ 51%	1129 keV/ 93% 2319 keV/ 82% 141 keV/ 67% 2186 keV/ 18%	High energy cyclotron	DPOA	-
^{66}Ga	9.3 h	1750 keV/ 57%	1039 keV/ 37% 2752 keV/ 23% 4295 keV/ 4%	Cyclotron	DOTA NOTA	^{71}Ga
^{72}As	26.0 h	1170 keV/ 88%	834 keV/ 81% 630 keV/ 8%	Cyclotron	Trithiol / lipoic acid	^{77}As
^{69}Ge	39.1 h	490 keV/ 24%	107 keV/ 36% 574 keV/13% 872 keV/ 12%	Cyclotron	Metal oxide nanoparticles	-

Success of ^{89}Zr-based probes in imaging of rat and mouse cancer models resulted in clinical translation, especially for ^{89}Zr-labelled antibodies. One of the groups reported "using ^{89}Zr-trastuzumab for imaging Her2-positive lesions in patients (n=14) diagnosed with metastatic breast cancer" [Diikers et al, 2010]. Studies with the ^{89}Zr-trastuzumab resulted in "high quality images, with high spatial resolution and good signal-to-noise ratio due to high uptake in tumour". In this study "the radiation dose to patients was attenuated compared to

the ^{89}Zr-cmAb-U36 investigations: patients received 37 MBq ^{89}Zr-trastuzumab for an average dose of 20 mSv" [Strosberg et al, 2017].

Another significant success in the field is clinical approval of ^{177}Lu-Dotatate (Luthathera) for use in patients. At the late stages of clinical trials in 2017 the treatment with Luthatera resulted in "markedly longer progression-free survival and a higher response rate than regular treatment among patients with midgut neuroendocrine tumours. Clinically significant myelosuppression occurred in roughly 8% of patients in the Luthatera group" [Strosberg et al, 2017].

3.6. Methods of coupling of antibodies to radionuclide

Two main methods of coupling of antibodies to radionuclide are iodination (or attaching isotope of iodine) and conjugation with radio metal. Both types of the procedures were developed as a result of many years of dedicated research.

Radioisotopes of iodine (^{123}I, ^{125}I ^{131}I) have been extensively used for labelling antibodies due to their ease of handling and long enough half-lives. The chemistry of iodine can form stable covalent bonds minimally altering the protein backbone. It is introduced directly by halogenation (in presence of enzymatic or chemical oxidants) of tyrosine and histidine residues of Abs. Common agents that are used as chemical oxidants are Iodogen, and Chloramine-T. There have been many reports of using them for direct labelling in order to convert sodium iodide to iodine form. According to previous studies, "in order to achieve higher labelling efficiency, the oxidant should be compatible with the aqueous solution of the protein and should not affect the protein structure. It is considered that Iodogen method achieves less specific activity, but has better effect on protein stability" [Gupta et al, 2014]. Conjugation of metallic radionuclides (^{89}Zr, ^{177}Lu, etc) to antibodies requires a chelating agent. The choice of chelating agent specifically relies on the properties of the radiometal

ion. The chelator is a source of donor atoms, which stabilize metal complex. Usually, a bi-functional chelating agents (BFCA) are used. They can bind covalently to monoclonal Abs and chelate radiometals simultaneously without affecting their kinetic and thermodynamic stability. Chelators like DOTA (1, 4, 7, 10-tetraazacyclododecane-1, 4, 7, 10-tetracetic acid), DTPA (NR-diethylenetriaminepentacetic acid), NOTA (1, 4, 7-triazacyclononane-1, 4, 7-acetic acid), DFO (p-SCN-Bn-Deferoxamine) have been used for radiolabelling antibodies for radioimmunotherapy and radioimmunodiagnosis. Labelling antibody with heavy metal radionuclides (^{177}Lu, ^{99m}Tc) and radiohalogen (^{125}I) is described [Aluicio-Sarduy et al, 2018].

Table 3. Parameters important for the choice of potential PET-radiometals. Decay properties, production methods, chelators, and theranostic pairs.

Radionuclide	$T_{1/2}$ (h)[a]	Emissions[b]	E max (keV)[c]	Range (mm)[c]	Labelling method
Technetium-99m	6.0	γ	140		Direct labelling or N2S2 or N3S complexes
Indium-111	67	γ	171 and 245		DTPA, DOTA
Iodine-123	13.3	γ	159		Direct labelling (tyrosine)
Fluorine-18	1.83	β^+	633	3.0	
Gallium-68	1.13	β^+	1,899	9.1	DOTA, NOTA
Copper-64	12.7	β^+ β^-	653 579	3.1 2.8	Many different chelating agents
Zirconium-89	78	β^+	902	4.3	DFO
Iodine-124	100	β^+	1,535 and 2,138	7.4 and 10	Direct labelling (tyrosine)
Iodine-131	193	β^- γ	610 362	2.9	Direct labelling (tyrosine)
Yttrium-90	64	β^-	2,250	11	DOTA
Rhenium-188	17	β^- γ	2,120 155	10	Direct labelling or N2S2 or N3S complexes
Lutetium-177	162	β^- γ	498 208	2.0	DOTA
Copper-67	62	β^- γ	392–577 184	1.8	Many different chelating agents
Bismuth-213	0.76	α γ	8,400 440	0.1	CHX-DTPA, DOTA
Astatine-211	7.2	α x	5,870 and 7,450 77–92	0.055–0.080	SAB, SAPS

3.7. Nuclear imaging

PET or Positron-emission tomography is a type of molecular imaging that directly or indirectly visualizes metabolic processes in the object of interest [Ter-Pogossian et al, 1975]. Its basic principles were formulated nearly half a century ago and via constant modification and advancement it is now an integral part of nuclear medicine usually aiding in diagnosis of disease or assessment of treatment efficacy [Weber et al, 1999].

PET consists of the ring of the detectors that detect pairs of gamma photons emitted from the annihilation of a positron, which is injected into the body. Three-dimensional images of isotope localization and concentration within the body are then reconstructed by computer analysis [Vandenberghe et al, 2006].

To initiate a study, a tracer containing positron emitting isotope is injected into the subject and after a waiting period during which the molecules or cells concentrate in relevant tissues, the study is conducted. During the decay, a positron and an antiparticle with positive charge are emitted. The positron encounters an electron and annihilates both electron and positron, producing a pair of annihilation gamma photons moving in opposite directions. Coincident events are detected in a scintillator of PET, creating light, which is detected by photomultiplier tubes [Strother et al, 1990].

Radionuclides used for PET imaging are isotopes with relatively short half-lives from such as ^{11}C and ^{13}N (less than 20 minutes), to more commonly used, ^{18}F, ^{68}Ga (less than 2 hours), to ^{89}Zr and ^{124}I (3-4 days). These radionuclides are attached to molecules commonly used by the body (such as glucose) or to molecules binding to receptors (Abs). Such labelled compounds are also called radiotracers. PET technology can be used to non-invasively trace a biological pathway, groups of cells (stem cells or T cells), or any compound in living species provided it can be radiolabellled with a PET isotope, making the list of processes that can be probed with PET virtually limitless [Huang et al, 2015].
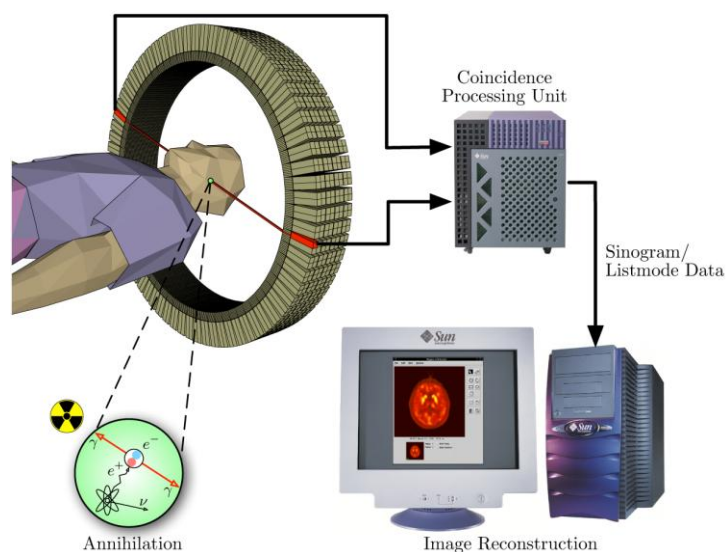
Figure 13. Schema of a PET acquisition process. *(Obtained from: https://commons.wikimedia.org/wiki/)*

SPECT is another nuclear imaging technique older than PET. It is similar to planar imaging (Gamma Camera) as it also makes use of single gamma rays emitted from injected radioisotope; it is capable of providing three-dimensional information. This information is presented as cross-sectional slices through the object. To do a SPECT study, the camera is moved in circle around the patient. Projections are acquired at multiple preset positions, every degree (more often every 3-10 degrees). 360-degree rotation is used to obtain the best quality of a reconstructed image. Some innovative approaches such as Multi-headed Gamma Cameras are currently used in clinic and provide accelerated acquisition (10-15 minutes) [Magdy et al, 2011].
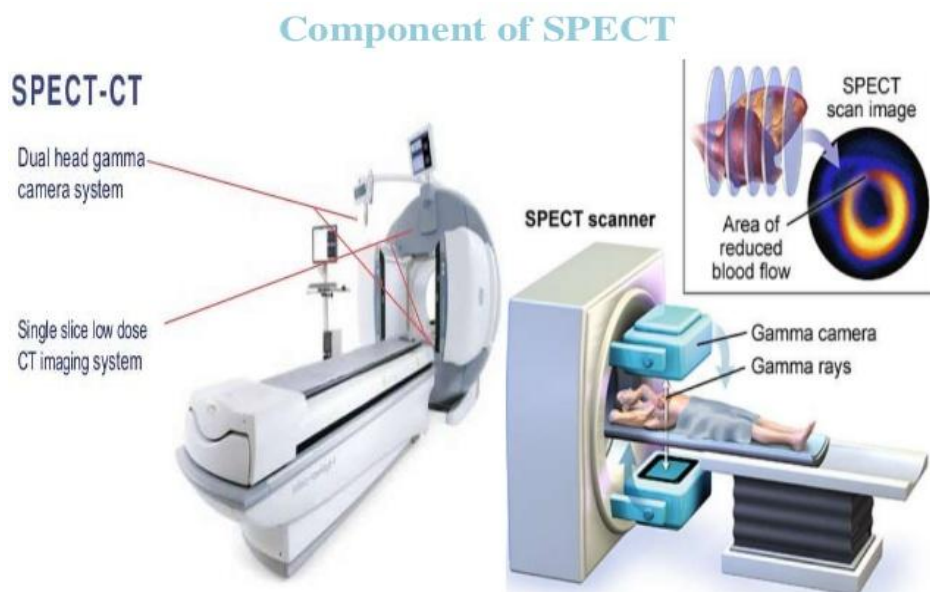
Figure 14. SPECT scanner augmented with CT capabilities. *(Obtaned from the Internet)*

In SPECT tracers are measured directly by their gamma decay, whereas PET scanner detects coincident annihilation events, which provides for more accurate localization of the event and, therefore, higher spatial resolution of images compaired to SPECT. However, SPECT is more sensitive, especially in localized areas (in comparison with full body imaging) and can utilize larger number of isotopes [Cai et al, 2013].

Both SPECT and PET can be supplemented with **Computed tomography, or CT,** for anatomical co-registration. CT is a diagnostic imaging test used to generate the cross-sectional images than can be done in many planes. It employs "computer-processed combinations of X-ray measurements taken from various angles to receive cross-sectional (tomographic) images of specific areas of an object of interest" [Bockisch et al, 2009].

Chapter 4. Project objectives and preliminary data

4.1. Diagnostics and treatment of RAS-driven cancers.

RAS isoforms are among the most commonly hyperactivated oncogenes in cancer. Although RAS itself is not "druggable", it was hypothesized that RAS may confer oncogenic transformation at least in part by remodeling the abundance and diversity of protein expression on the cell surface. It was further hypothesized that cell surface proteins whose expression was highly upregulated by mutant RAS could be targeted with small molecules or antibodies to selectively detect tumour cells with molecular imaging, and/or treat cells with ligand-drug conjugates.
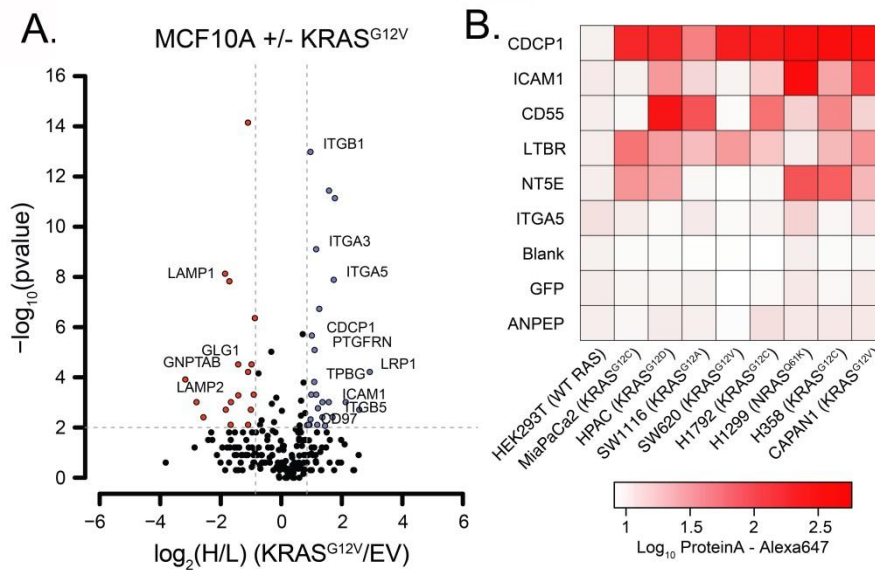
Figure 15. KRAS mutant cell surface proteomics screen results (A). A volcano plot depicting the results of a cell surface proteomics screen to identify proteins differentially regulated by mutant KRAS. The upregulated hits are annotated in the upper right portion of the plot. (B). A heat map showing the relative expression levels of the top 7 hits emerging from the proteomics screen. Protein expression was determined with flow cytometry, and CDCP1 was highly induced in all cell lines compared to control (HEK293T with WT RAS).

Towards this model of "indirectly" inhibiting RAS, proteomics was recently applied to characterize the cell surface proteomic changes driven by oncogenic RAS. A survey conducted in MCF10A cells revealed 17 proteins significantly upregulated on the cell surface due to oncogenic KRASG12V. Validation studies showed that the cell surface expression of CDCP1 was most dramatically, and most consistently, upregulated in human cancer cell lines by mutant KRAS. Moreover, using the industrial automated phage display platform within the Antibiome center at UCSF, several highly potent and specific recombinant human IgGs against the extracellular domain of CDCP1 were generated. The general goal of the project was to develop and evaluate the pharmacology of ^{177}Lu-4A06 and ^{89}Zr-4A06, a novel recombinant human antibody targeting the cancer-associated cell surface antigen CUB domain containing protein 1 (CDCP1)

The following specific aims were set:

Aim 1. To assess toxicity, specificity, stability and biodistribution of newly developed anti-CDCP1 antibody (4A06) labelled with ^{89}Zr isotope

Aim 2. To assess toxicity, specificity, stability and bio-distribution of 4A06 antibody labelled with ^{177}Lu isotope

Aim 3. To test therapeutic potential of ^{177}Lu-4A06 in pancreatic ductal adenocarcinoma cancer animal model

Preliminary Results

Preliminary results are described in the following article:

- Martinko AJ, Truillet C, Julien O, et al. Targeting RAS-driven human cancer cells with antibodies to upregulated and essential cell-surface proteins. Settleman J, ed. eLife. 2018;7:e31098. doi:10.7554/eLife.31098.

Development and characterization of 4A06, a potent and specific human recombinant Fab against an extracellular epitope on CDCP1: To facilitate the discovery of high affinity and specificity Fabs against CDCP1, the recombinant extracellular domain (ECD) was expressed as an Fc fusion protein in HEK293 cells. A biotin acceptor tag was introduced on the C terminus along with a TEV proteolysis site between the Fc-domain and the ECD. These tags allow for site selective capture of the Fc-fusion on magnetic streptavidin beads, and release of the ECD/Fab complex after TEV proteolysis. This is a custom "catch and release" strategy designed to selectively release Fab-phage bound to ECD, while avoiding enrichment of Fab-phage that either binds the Fc-domain or the beads themselves. The Fc-fusion was transiently expressed in HEK293 cells and purified with Protein A for phage selection. Four rounds of "catch and release" were performed with a well-validated synthetic Fab-phage library (Figure 15). 4A06 was one of four Fabs identified against CDCP1, and further *in vitro* characterization revealed it to have a sub nM Kd for CDCP1 (Kd = 2.8 nM). Moreover, CRISPR deletion of CDCP1 from multiple mammalian cell lines abrogated binding of fluorescently labelled 4A06 to cells, confirming the specificity of the antibody for CDCP1 (Figure 16).
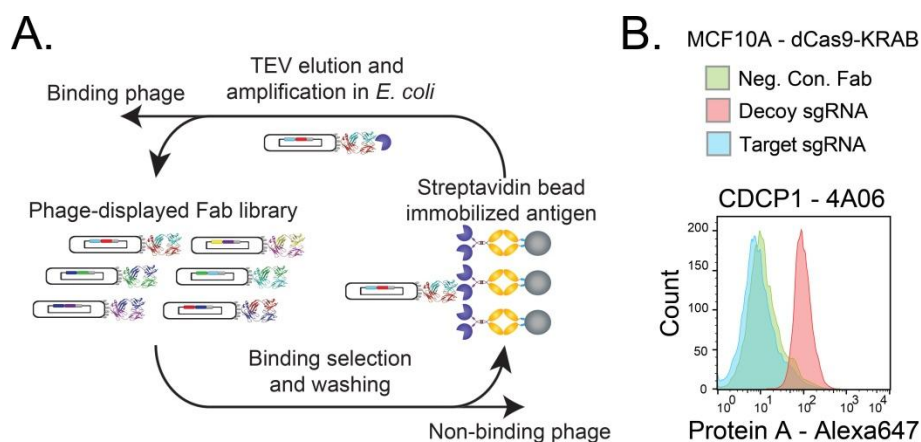
Figure 16. 4AO6 antibody synthesis and characterization (A). A schema showing the catch and release phage display selection strategy used to identify 4A06, a potent recombinant human Fab against CDCP1. (B). Flow cytometry data showing that fluorescently labelled 4A06 selectively binds to MCF10A cells with CDCP1 expression (decoy sgRNA), but not to cells previously subjected to CRISPR/Cas9 deletion of CDCP1 (target sgRNA). These data underscore the specificity of 4A06 for CDCP1.

^{89}Zr-4A06 specifically targets tumour expression of CDCP1: To evaluate if the Fab can measure tumour autonomous expression of CDCP1 *in vivo* with PET, we next conducted bioconjugation and radiochemistry on 4A06. 4A06 was functionalized with desferrioxamine (DFO) by reacting p-isothiocyanatobenzyl-DFO with solvent exposed epsilon amino groups on lysine residues. This resulted in an antibody chelate number of ~2. Radiolabelling was achieved by incubating ^{89}Zr oxalate with DFO-4A06 for 120 min. ^{89}Zr-4A06 was purified with size exclusion chromatography, and the radiochemical yield was consistently >95% with a purity consistently >99%.

To assess specific binding *in vivo*, intact male nu/nu mice were inoculated with subcutaneous HPAC xenografts, a human pancreatic cancer model with the KRAS^{G12V} mutation, and ~3 x 10^6 copies of CDCP1 per cell. PET/CT and biodistribution studies showed specific binding of ^{89}Zr-4A06 within 4 hours post injection. Moreover, the radiotracer persisted in the tumour out to 24 hours post injection. Tumour uptake of the radiotracer was significantly suppressed in mice receiving heat denatured ^{89}Zr-4A06, or a co-

injection of 20-fold excess unlabelled 4A06. The radiotracer uptake was also very low in A549, a human lung cancer model with only 6×10^5 copies of CDPC1 per cell.
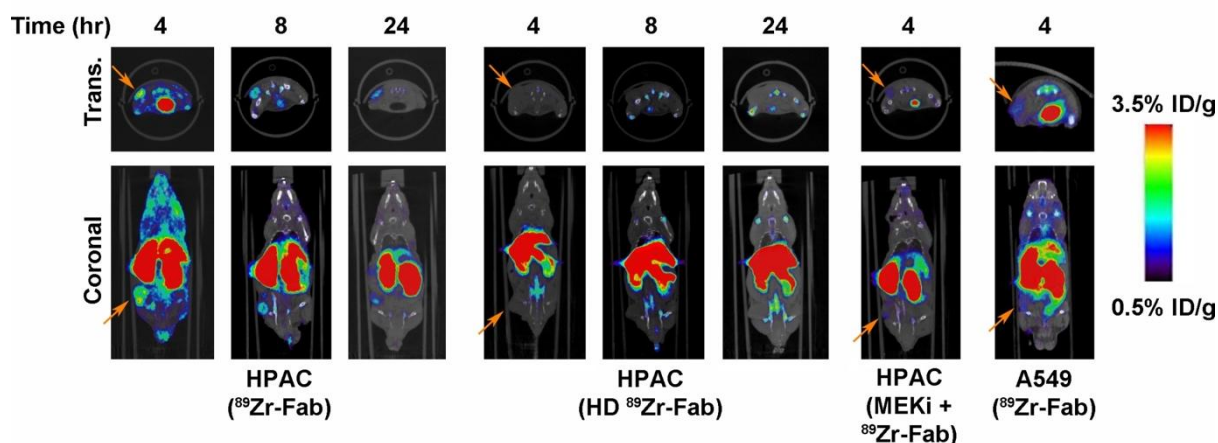
Figure 17. Representative microPET images of four immunocompromised nu/nu mice bearing cancer xenografts targeted with ^{89}Zr-labelled CDCP1 Fab. Images over time show the tumour specific expression of CDCP1, as well as the persistent binding of the Fab to the tumour over 24 hr (Left). Importantly, when the same Fab was heat-denatured prior to injection or when a negative control xenograft was used, there was no observable uptake of the ^{89}Zr-Fab (Middle and Right). Remarkably, no uptake was observed in the mouse treated with a sub-toxic dose of MEKi prior to imaging, demonstrating the coupling of CDCP1 expression MAPK pathway signaling in vivo. (Data are decay corrected).

Using the same technique of protein labelling with radioactive isotopes two more independent studies were conducted.

4.2.   Imaging of PD-L1 expression with ImmunoPET

The PD-1, a short for programmed cell death-1 receptor, is present on the surface of T-lymphocytes in an activated state. It has two ligands: PD-L1 (CD274) and PD-L2 (CD273), which were discovered on the macrophages or dendritic cells acting as co-inhibitory factors, which can decrease or completely stop the T-cell response. In normal conditions PD-1/PD-L1 system ensures that the immune system is activated only when it is needed, reducing the risk of chronic autoimmune reaction.

The idea of their existence was around for quite a while until it was proved by scientists from Dana-Farber Institute, who discovered that cancer cells of several origins "wear" one of those proteins, called PD-L1. It is a defense mechanism that allows the cancer cells to avoid human immune system [Gordon et al, 2000].

The ramification of this discovery was profound as it changed the notion that tumours are part of human body, instead by finding a way to block this PD1/PDL1 interaction, the immune system will be able to "see" the tumour and conduct the attack. Such a clear therapeutic concept immediately attracted major pharmaceutical companies and this field is currently one of the best-funded areas of cancer research. Nowadays scientific community calls this and similar systems - *check point inhibitors* and defines them as a relatively novel class of inhibitors that operates by modulation of immune cell - tumour cell interaction resulting in tumour suppression.

The first clinical trial of a PD-L1-blocking drug began in 2008 in patients with blood cancers [Berger et al, 2008]. Currently, there are several successful implementations of monoclonal antibody therapies against PD-1 and PD-L1. The most frequently used is Nivolumab, an anti-PD-1 drug developed by Bristol-Myers Squibb, which is approved for previously treated metastatic melanoma and squamous non-small cell lung cancer [Gettinger et al, 2014]. Soon other drugs based on the same principle were introduced to treat melanoma [Hodi et al, 2010] and other cancers like lung, prostate, renal and bladder cancers where progress was reported in various stages of clinical trials [Garon et al, 2015; Slovin et al, 2013].

Literature also reports Atezolizumab (trade name Tecentriq®), a fully humanized, monoclonal IgG1 against the PD-L1. In late 2016, Atezolizumab was approved by FDA for the treatment of patients with metastatic non-small cell lung cancer (NSCLC).

The mixed and transient clinical responses to antibody-based immune checkpoint inhibitors have stimulated a great interest in identifying biomarkers to predict which patients are most likely to benefit from therapy. Tissue analysis has shown that tumour mutational burden, deficiencies in DNA mismatch repair machinery, and/or checkpoint protein expression can predict favourable outcome [Rizvi et al, 2015; Patel et al, 2015; Le et al, 2017].

However, these biomarkers generally depend on the analysis of one biopsy from patients with widespread tumour burden and therefore can bear undesirable false positivity and negativity. On this basis, the molecular imaging field proposed that a more holistic view of tumour biology among all lesions in a patient might confer more reliable predictive biomarkers.

Predicting tumour responses to checkpoint inhibitors with routine CT and PET/CT has been challenging as progressive disease is often difficult to distinguish from responsive disease early after the initiation of therapy [Kwak et al, 2015; Wong et al, 2017].

For instance, edema or necrosis following recruiting T-cell to the tumour microenvironment can cause tumour enlargement that mimics progression on CT. Moreover, ^{18}F-fluoro-deoxyglucose (FDG) is avidly consumed by activated lymphocytes. Therefore, the increase in ^{18}F-FDG accumulation in the tumour microenvironment after effective therapeutic intervention poses a challenge to distinguish this normal process from elevated radiotracer uptake induced by progressing tumours. In both cases, observing clear radiographic tumour responses often requires constant imaging several months of post-therapy.

Many groups have responded to this challenge by developing experimental molecular imaging technologies targeting checkpoint proteins, antigens specific to T-cell populations (e.g. CD4, CD8), or biological events upregulated by cytotoxic T-lymphocytes (e.g. nucleotide salvage pathways, granzyme B) [Wei et al, 2018; Ehlerding et al, 2016]. On the

leading edge of clinical translation are several protein-based radiotracers targeting PD-L1, including [89]Zr-atezolizumab (atezo), [89]Zr-avelumab, and the adnectin ^{18}F-BMS-986192 [Bensch et al, 2017; Donnelly et al 2018]. The first available clinical data from 16 patients receiving [89]Zr-atezo support the expected diversity of PD-L1 expression levels in clinical disease (SUVmax between 1.6 and 46) and underscore the potential utility of imaging to holistically measure checkpoint protein expression over a patient's entire tumour burden. Notably, high radiotracer uptake was also observed in many PD-L1 rich normal tissues (e.g. liver, spleen, kidneys, lymph nodes, and intestines). Whether radiotracer sequestration in normal tissues interferes with measurement of PD-L1 in tumours is unclear.

Therefore, reverse translational studies with [89]Zr-atezo were conducted to understand whether the measurement of tumour-associated PD-L1 expression could be improved, as well as to begin assessing its relative strengths and weaknesses compared to [89]Zr-labelled C4, a recombinant human anti-PD-L1 IgG1 that detects tumour associated antigen with little "background" in normal mouse tissues. Like atezo, C4 has low nM affinity for an epitope on the ectodomain of natively expressed human and mouse PD-L1 ($EC_{50} = 5.5$ nM and 6.6 nM, respectively). Moreover, functionalization of C4 with desferrioxamine (DFO) for imaging did not significantly impact its affinity ($IC_{50} = 5.2$ nM, 9.9 nM for natively expressed mouse and human PD-L1, respectively), or the immunoreactive fraction (~93%). Although atezo was previously radiolabellled with Cu-64 and In-111, directly comparing the existing preclinical biodistribution data to those for [89]Zr-C4 is challenging, as the differences in bioconjugation chemistries and biological fates of the catabolized radiometals can impact biodistribution in a manner unrelated to the properties of the respective antibodies [Bryan et al., 2011; Lesniak et al., 2016; Chatterjee et al., 2016]. Moreover, biodistribution studies with [89]Zr-C4 were conducted in immunocompetent C57BL/6J and T-cell deficient nu/nu mice, while studies with [64]Cu- and ^{111}In-atezo were conducted in severely immunodeficient NSG mice. As a

recent study elegantly demonstrated, the immune status of laboratory mice can dramatically impact immunoglobulin biodistribution in normal tissues of relevance to PD-L1 like the spleen and bone through CDR-independent mechanisms [Sharma et al, 2018].

The goal of this study was to conduct reverse translational studies aiming to improve quality of PD-L1 imaging and to more systematically compare characteristics of ^{89}Zr-atezo and ^{89}Zr-C4.

4.3 Targeting mTORC1 signaling to detect tuberous sclerosis complex and lymphangioleiomyomatosis with PET

Tuberous sclerosis complex (TSC) is an autosomal dominant disease predicated on genetic mutations that inactivate the TSC1/TSC2 complex [Crino et al, 2006; Patel et al, 2015].

TSC is generally a non-malignant yet progressive disorder that manifests itself through a "bloom" of hemartomas in various organs from infancy into adulthood, many of which incur debilitating symptoms (e.g. epilepsy, impaired cognitive development). TSC also significantly elevates the risk of secondary disorders that arise in part due to TSC1/2 inactivation, including the destructive lung disease lymphangioleiomyomatosis (LAM) [Le et al 2017].

The clinical courses of TSC and LAM are highly unpredictable. On this basis, non-invasive biomarkers of disease burden and/or activity are crucial to effective disease management. For instance, routine electroencephalogram in asymptomatic TSC infants captures those at high risk of developing epilepsy, which in turn motivates prophylactic treatment with vigabatrin for seizure control [Kwak et al, 2015]. Moreover, elevated serum VEGF-D levels in women with TSC can signal the onset of LAM, which, when combined with high resolution CT, enables earlier diagnosis and treatment [Wong et al, 2017]. Despite

these milestones, the overwhelming majority of clinical manifestations of TSC and LAM have no cognate biomarker for diagnosis, predicting aggressive versus indolent disease, or monitoring response to systemic therapies.

Although TSC and LAM are phenotypically heterogeneous, a unifying subcellular consequence of TSC1/2 loss is elevated mTORC1 signaling, regardless of how and in what organs clinically problematic cells manifest [Wei et al, 2018]. On this basis, we hypothesized that a molecular event regulated downstream of mTORC1 could serve as a useful biomarker of disease burden. mTORC1 regulates a broad spectrum of metabolic changes, including transferrin dependent Fe(III) uptake into cells [Ehlerding et al, 2016; Bensch et al, 2017 The possibility to use radiolabelled transferrin to non-invasively measure mTORC1 activity in models of malignant cancers using PET was recently demonstrated [Donnelly et al, 2018].

The the primary objective of this study was to determine if non-malignant models representative of TSC and LAM are detectable with [89]Zr-transferrin.

Chapter 5. Materials and methods

5.1. *In vitro* studies

5.1.1 Cell cultures

HPAC, a pancreatic adenocarcinoma epithelial cell line was acquired from American Type Culture Collections (ATCC). It was derived in 1985 from xenograft of moderate to well-differentiated pancreatic adenocarcinoma.

A549, a human lung cancer was also acquired from ATCC. This line was initiated in 1972 from human lung carcinoma tissue.

B16F10, mouse melanoma cell line, growing as a mixture of spindle-shaped and epithelial-like cells, was acquired from ATCC.

H1975, human adenocarcinoma; non-small cell lung cancer cell line from ATCC.

The stock of cells was expanded to 50 million cells and then frozen in liquid nitrogen in aliquots of 3 million cells in 1 ml of DMSO media and cultured according to recommendations. Each individual cell culture was not kept beyond 10 passages to minimize the risk of mutations.

RT4, tsc2 ang1 and HCV29 cells were acquired from ATCC and subcultured according to manufacturer's recommendations. 97-1 human bladder cancer cell line was kindly provided by Dr. Margaret A. Knowles University of Leeds, UK and subcultured in F12 media Kaighn's modification (HyCloneTM, Logan, Utah) with 10% (v/v) fetal calf serum (FCS), 1% penicillin/streptomycin (Pen/Strep). ELT3, 105K were subcultured in DMEM (Corning, Manassas, VA) with 10% FCS, 1% Pen/Strep, 621-101 in F12 media (Corning, Manassas, VA) with 10%FCS, 1% Pen/Strep.

5.1.2. Patient derived xenografts

PDX were generated from patients admitted to UC Medical Center with clear pancreatic ductal adenocarcinoma tumours, following an approved IACUC protocol **AN142193-02A**. Some of the tissue was used for *in vitro* evaluation, including preparation of single cell suspension for Flow Cytometry. Briefly, the cell tissue was mashed via filter wells and washed with warm PBS. The resulted supernatant was centrifuged at 2000 rpm for 5 minutes and resuspended in buffer with 5% FCS for staining and subsequent FACS analysis. KRAS p.G12D mutation was confirmed with next generation sequencing (UCSF 500 Genetic Panel).

5.1.3. Antibodies

Antibodies were generated as previously described at [Martinko et al., 2018]: "C43 (DE3) Pro +*E. coli* were grown in TB at 37 °C to an OD600 of 0.6–0.8 and then Ab expression was induced by adding 1 mM IPTG. The cells were harvested by centrifugation and Fabs were purified by Protein A affinity chromatography. Fab purity and integrity were assessed by SDS-PAGE and intact protein mass spectrometry using a Xevo G2-XS Mass Spectrometer (Waters)".

5.1.4. Flow cytometry

Approximately $1x10^6$ cells per sample were lifted with Cellstripper (Corning, Manassas, VA), washed twice with PBS pH 7.4, and subsequently blocked with flow cytometry buffer (PBS, pH 7.4, 3% BSA). Anti-CDCP1 (10 mg/mL) or commercial antibodies were added to cells which were kept for 30 minutes on ice. Antibodies were detected by adding Protein A – Alexafluor-647 conjugate (Life Technologies; 1:1000). Cells were extensively washed, and fluorescence was quantified using a FACSCalibur on FL4

single channel analysis (BD Biosciences). All flow cytometry data were analysed using FlowJo software (FlowJo LLC, Oregon). Data were normalized for living cells only.

5.1.5. Immunoblotting

Cells were plated at approximately 2-3x106 cells/plate in a 10cm tissue-culture plate and cultured overnight before drug treatment. The medium was replaced with medium supplemented with 100 nM INK128 (Adooq Bioscience LLC, Irvine, CA), 10nM RAD001 (Selleck Chemicals, Houston, TX), 100 nM NVP-BEZ235 (LC Laboratories, Woburn, MA), 5 nM doxorubicine, or vehicle (0.2% DMSO). The cells were further incubated at 37°C for 5 hr, after which the cells were washed with PBS and lysed with RIPA Lysis and Extraction Buffer (Millipore, Temecula, CA) supplemented with 1X Protease and phosphatase Inhibitor Cocktail (Thermo Scientific) at 4°C for 10 min. Immunoblotting was performed using antibodies to a total S6, p-S6 (S235/236). Protein concentration was determined by the Bradford absorbance assay, and 15 μg of lysate were resolved with 1D SDS-PAGE.

5.1.6. Real-time PCR

RNA was harvested from cells with an RNAeasy plus mini kit (Qiagen). The purity and concentration of RNA was quantified using a NanoDrop spectrometer (Thermo Scientific), and 1.5 μg of RNA was converted to cDNA RT kit (Applied Biosystems). Relative changes in mRNA levels were assessed with a Pikoreal real time PCR cycler (Thermo Fisher Scientific). Ct was calculated using the respective actin control, and ΔΔCt was calculated by normalizing Ct values to vehicle control. Primers were ordered from INTEGRATED DNA TECHNOLOGIES (Redwood City, CA) with the following sequences: Human primers Forward: 5'- AAA ATC CGG TGT AGG CAC AG -3';

Reverse: 5'- CAC CAA CCG ATC CAA AGT CT -3'; Mouse/ rat Forward: 5'- GTT TCT GCC AGC CCC TTA TTA T -3'; Reverse: 5'- GCA AGG AAA GGA TAT GCA GCA -3'.

5.1.7. *Cellular receptor binding assays*

Cells were seeded at a density of 4×10^5 cells per well in 12-well plates. On the day of the experiment, cells were subjected to a PBS wash followed by incubation for 1 h at 37 °C, 5% CO2 in PBS with ^{89}Zr-atezo (0.5 µCi), or ^{89}Zr-atezo with 10x unlabeled atezo or C4. Cells were incubated for 30 min at 4 °C, whereupon the medium was removed, and the residual unbound radiotracer was removed with two washes with ice cold PBS. The cell bound activity was harvested by lysis in 1 mL of 1 M NaOH and collected. The unbound and cell-associated fractions were counted in a γ counter and expressed as a percentage of the total activity added per well per cell number. Experiments were performed in triplicate, and the data are representative of at least two independent experiments.

5.1.8. *Bioconjugation of antibodies with chelator agents*

As the first step to develop radiolabeled antibodies suitable for *in vivo* imaging and later for clinical applications, I have conducted series of studies aiming to develop bioconjugates of abs with chelator groups. Kinetic constants for anti-CDCP, anti-CDCP1 conjugated with DFO, anti-CDCP1 conjugated with DOTA against human CDCP1 were determined using an Octet RED384 instrument (ForteBio) as previously described ay [Christopher et al,. 2016]: "Six concentrations of each antigen (250 nM, 125 nM, 62.5 nM, 31.25 nM, 15.625 nM) and 7.812 nM for human CDCP1 were tested for binding to the anti-CDCP1 antibody immobilized on Anti-Human IgG Fc Capture biosensors (Fortebio). All measurements were performed at room temperature in 384-well microplates and the running buffer was PBS with 0.5% (w/v) bovine serum albumin (BSA) and 0.05% (v/v) Tween

20. Anti-CDCP1 antibody was loaded for 180 sec from a solution of 300 nM, baseline was equilibrated for 60 s, and then the antigens were associated for 600 s followed by 1200 sec disassociation. Between each sample, the biosensor surfaces were regenerated three times by exposing them to 10 mM glycine, pH 1.5 for 5 sec followed by PBS for 5 sec. Data were analyzed using a 1:1 interaction model on the ForteBio data analysis software 8.2".

DOTA-NHS-ester: Anti-CDCP1 antibody clone 4A06 (400 μL at a concentration of 7.65 mg/mL) was dispersed in 500 μL of 0.1 M sodium bicarbonate buffer (pH 9.0). The final reaction mixture volume was adjusted to a total volume of 1 mL by adding a sufficient amount of 0.1 M sodium bicarbonate buffer. 1,4,7,10-Tetraazacyclododecane-1,4,7,10-tetraacetic acid mono-N-hydroxysuccinimide ester (*DOTA-NHS-ester*, 10mg/mL DMSO, 40-60 molar excess) was added to the antibody solution dropwise while mixing vigorously. The final concentration of DMSO was kept below 2% (v/v) to avoid any precipitation. The reaction was allowed to incubate for 90 min at 37°C, whereupon the reaction mixture was purified with a PD-10 column using an ammonium acetate mobile phase (0.2 M sodium acetate, pH 7.0). The hTf-DFO solution was aliquoted and stored at -20° C until time of use.

p-Df-Bz-NCS: Anti-CDCP1 antibody clone 4A06 (261μL at a concentration of 7.65 mg/mL) was dispersed in 200 μL of 0.1 M sodium bicarbonate buffer (pH 9.0). The final reaction mixture was adjusted to a total volume of 0.5 mL by adding a sufficient amount of 0.1 M sodium bicarbonate buffer. Para-Isothiocyanatobenzyl-desferrioxamine (p-Df-Bz-NCS, 30 mM in DMSO, 4 eq.) was added to the antibody solution drop wise while mixing vigorously. The final concentration of DMSO was kept below 2% (v/v) to avoid any precipitation. The reaction was allowed to incubate for 30 min at 37°C, whereupon the reaction mixture was purified with a G25 column using an ammonium acetate mobile phase (0.2 M sodium acetate, pH 7.0). The hTf-DFO solution was aliquoted and stored at -20° C until time of use.

Bifunctional chelators (BFCs): *p-SCN-Bn-Deferoxamine* *((1-4-isothiocyanatophenyl)-3-[6,17-dihydroxy-7,10,18,21-tetraoxo-27-(N-acetylhydroxylamino)- 6,11,17, 22-tetraazaheptaeicosine] thiourea* and *DOTA-NHS-ester* (1,4,7,10-Tetraazacyclododecane-1,4,7,10-tetraacetic acid mono-N-hydroxysuccinimide ester) were obtained from Macrocyclics (Dallas, TX).

5.1.9. Radiolabeling

^{177}Lu labeling: A solution of ^{177}Lu-HCl (hydrochloric acid) (8mCi; 40 µl) was diluted with 200µL 0.2M ammonium acetate. 2 mg in 1.4mL of DOTA-anti-CDCP1 (pH = 7) were added into the reaction vial. After incubation for 60 min at 37°C, the reaction progress was monitored by ITLC using a 20 mM citric acid (pH 4.9–5.1) mobile phase. The decay corrected radiochemical yield was consistently > 95%.

^{89}Zr-labeling: A solution of ^{89}Zr-oxalic acid (5mCi; 40 µl) was neutralized with 2 M Na_2CO_3 (18 µl). After 3 min, 0.30 ml of 0.5 M HEPES (pH 7.1–7.3) and 1.5 mg of DFO-anti-CDCP1 (pH = 7) were added into the reaction vial. After incubation for 60 min at 37°C, the reaction progress was monitored by ITLC using a 20 mM citric acid (pH 4.9–5.1) mobile phase. The decay corrected radiochemical yield was consistently > 95%.

Radioiodination of anti-CDCP1: Iodination with iodine-125 was done in pre-coated iodination tubes (Pierce). 100 µg of anti-CDCP1 Ab was dispersed in 100 µL of PBS solution and added to the pre-coated iodination tubes. 0.5 mCi of iodine-125 was diluted with PBS up to 100µL and added to the iodination tubes. After 15 min of reaction the solution was purified via PD G-25 column pre-equilibrated with 10 mL of PBS solution. The purity was assessed *via* iTLC, and ^{125}I-Tf was always >98% pure.

5.1.10. Internalization study

Cells were seeded at a density of 4×10^5 cells per well in 12-well plates. On the day of the experiment, cells were subjected to a PBS wash followed by incubation for 15 min, 30 min or 60 min at 37^oC, 5% CO_2 in PBS with ^{125}I-anti-CDCP1 (0.5 μCi). A control set of cells was incubated for 15 min, 30 min or 60 min at 4^oC, whereupon the media was removed, and the residual unbound radiotracer was removed with two washes with ice cold PBS. Surface cell bound activity was harvested by application of ice-cold 10% aqueous Citric acid solution for 5 min at 4^oC. The cell bound activity was harvested by lysis in 1 mL of 1M NaOH and collected. The unbound, surface-bound and cell-associated fractions were counted in a gamma counter and expressed as a percentage of the total activity added per well per cell number. Experiments were performed in triplicate, and the data are representative of at least two independent experiments.

5.2.   *In vivo* studies

5.2.1. *Animal handling*

All animal studies were conducted in compliance with Institutional Care and Use Committee at UCSF. In order to perform animal studies, I have attended and successfully completed 17 various courses of *in vivo* training, ranging from general animal handling and biosafety to animal surgery and working with radioactive materials *in vivo*. I was supervising the whole colony of mice for my studies (126 mice in total), performing all injections and handling anesthesia while doing imaging experiments. I was responsible for development of cell line derived xenografts and I was also responsible for doing the entirety of dissections and *ex vivo* assays.

Animals in my colony were divided in the following studies and cohorts:

Table 4. Groups of animals in the *in vivo* studies.

Study	Number of groups	Number of animals per group
^{89}Zr Pilot	3	5
^{89}Zr BioD and Block	3	8
^{177}Lu Pilot dosimetry	1	5
^{177}Lu Pilot treatment	2	5
^{177}Lu treatment	2	10
PDX treatment with ^{89}Zr	2	5

5.2.2. *Establishment of the animal model with patient derived xenografts*

PDX were generated from patients admitted to UC Medical Center with clear pancreatic ductal adenocarcinoma tumours, in accordance with an approved IACUC protocol **AN142193-02A**. Briefly, after pathological evaluation of the recently resected tumour, tissue samples were collected from these specimens under patients' consent and surgically implanted orthotopically into 4-week-old NSG-mice.

5.2.3. *Small animal imaging*

Small animal PET/CT: All animal studies were conducted in compliance with Institutional Care and Use Committee at UCSF. PDX models nu/nu at 2-3 months old were used in these experiments. Three to five-week-old intact male athymic nu/nu immunocompromised mice were purchased from Charles River. Nu/nu mice were inoculated with 1.5x 10^6 HPAC cells subcutaneously into one flank in a 1:1 mixture (v/v) of media (DMEM/F12) and Matrigel (Corning). Xenografts were palpable within 14-18 days after

injection. Tumour-bearing mice (n=5 per treatment arm) received between 40 to 250 μCi of solution in 100 μL saline solution volume intravenously using a custom mouse tail vein catheter with a 28-gauge needle and a 100-150 mm long polyethylene microtubing. ~200 μCi and ~40 μCi were injected for imaging and biodistribution studies, respectively. The mice were imaged on a dedicated small animal PET/CT scanner (Inveon, Siemens Healthcare, Malvern, PA). Mice were imaged at 0.5, 4, 24, 48, 72, 96 hours post injection. Animals were scanned for 40 minutes for PET, and the CT acquisition was performed for 10 minutes. The co-registration between PET and CT images was obtained using the rigid transformation matrix from the manufacturer-provided scanner calibration procedure since the geometry between PET and CT remained constant for each of PET/CT scans using the combined PET/CT scanner. During the imaging procedure, animals were anesthetized with gas isoflurane at 2% concentration mixed with medical grade oxygen. The photon attenuation was corrected for PET reconstruction using the co-registered CT-based attenuation map to ensure the quantitative accuracy of the reconstructed PET data. Animals were scanned for 50 minutes for SPECT, and the CT acquisition was performed for 10 minutes.

5.3. Post-mortem tissue samples studies

5.3.1. Biodistribution studies

Biodistribution studies were conducted to evaluate the uptake of ^{89}Zr-CDCP1 / ^{177}Lu-CDCP1 in mice bearing subcutaneous tumours. At a dedicated time after radiotracer injection, animals were euthanized by cervical dislocation, and fifteen tissues (including tumour) were removed, weighed and counted on a gamma-counter for accumulation of ^{89}Zr-radioactivity / ^{177}Lu-CDCP1 activity. The mass of ^{89}Zr-CDCP1/^{177}Lu-CDCP1 injected was measured and used to determine the total number of CPM by comparison with a standard of

known activity. The data were background- and decay-corrected and was expressed in %ID/g.

5.3.2. *Digital autoradiography and histology*

DAR and histology were performed as previously described at [Escorcia et al., 2018]: "Tumours of animals were excised and Tissue–Plus OCT compound (Scigen, Gardena, CA) was added. For storage samples were kept in -80 C. 10 μm tissue sections were cut and placed in cassette with film for 48–72 h at − 20°C (BASMS-2325; Fujifilm, Tokyo, Japan), which was then read on a Typhoon 7000IP plate reader (GE Healthcare, Chicago, IL) at 25 μm pixel resolution. Several sequential sections were submitted to the MCCF at UPenn for hematoxylin and Eosin staining. Image analysis was performed with ImageJ" (https://imagej.nih.gov/ij/).

5.3.3. *Microscopy*

A Zeiss Axioplan2 microscope was used to develop microscopic images. MetaMorph software (Molecular Devices, Sunnyvale, CA) and Photoshop CS6 software (Adobe Systems, McLean, VA) weres used for montage and processing.

5.4. **Statistical analysis**

Data were analyzed using the unpaired, two-tailed Student's t-test using PRISM software. Differences at the 95% confidence level (P < 0.05) were considered to be statistically significant.

Chapter 6. Results

6.1. Preclinical testing of new modalities for PET visualization and treatment of RAS-driven cancer

6.1.1. ^{89}Zr-labeled 4A06 specifically detects tumour autonomous expression of CDCP1.

To understand if the 4A06 IgG can specifically target and bind to tumour associated CDPC1 in vivo, we functionalized the 4A06 antibody with desferrioxamine (DFO) for PET/CT studies. To achieve this, commercial para-isothiocyanatobenzyl-DFO was reacted with solvent-exposed ε-amino groups on lysine residues. The affinity of DFO-4A06 for the recombinant human ectodomain of CDCP1 was assessed ex vivo using biolayer interferometry (Fortebio, Octet Red384 system), and the KD of the DFO-conjugated antibody was equivalent to unmodified 4A06 (0.40 ±0.7 nM and 0.27±0.04 nM, respectively). In anticipation of the future studies with Lu-177 conjugated 4A06, the antibody was also coupled to the chelator 1,4,7,10-Tetraazacyclododecane-1,4,7,10-tetraacetic acid (DOTA) via similar chemistry. The affinity of DOTA-4A06 was also equivalent to unlabeled 4A06 (KD = 0.30 ± 0.05 nM) (Figure 18).
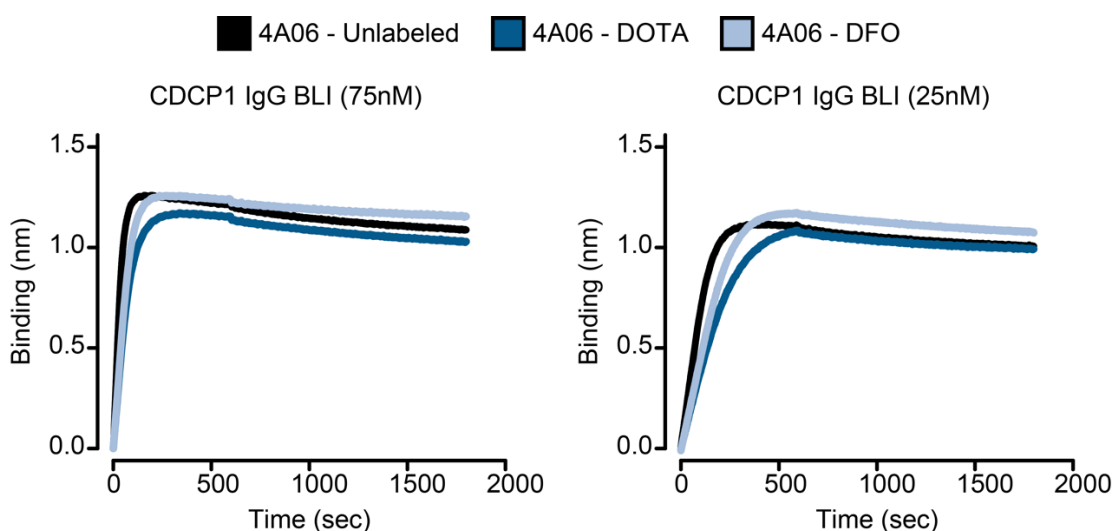
Figure 18. *Affinity assessment. The affinity of DFO-4A06 and DOTA-4A06 is equivalent to unlabeled 4A06 (K_D = 0.40 ±0.7 nM, 0.30 ± 0.05 nM and 0.27±0.04 nM, respectively).*

DFO-4A06 used was radiolabeled via incubation with [89]Zr-oxalic acid for 120 min and purified using size exclusion chromatography. The radiochemical yield was consistently >95%, the radiochemical purity >98%, and the specific activity was ~ 3,35 µCi/µg.

To evaluate specific antigen binding *in vivo*, [89]Zr-4A06 was administered to intact male nu/nu mice bearing subcutaneous HPAC tumours, a human pancreatic adenocarcinoma cell line with an endogenous KRAS G12V mutation. The tumour-associated radiotracer was visually obvious on PET/CT at 12 hours post injection, and the amount of radiotracer steadily increased out to 72 hours post injection. The analysis of tissue biodistribution *ex vivo* corroborated this trend, showing that the highest radiotracer uptake in the HPAC tumours occurred at 72 hours. Moreover, the radiotracer was steadily cleared from blood and normal mouse tissues from 24 to 72 hours. One notable exception was the liver which had persistently high radiotracer uptake due to clearance of the IgG. A separate cohort of mice received [89]Zr-4A06 with 20X excess unlabeled 4A06. PET/CT and biodistribution studies clearly showed that excess unlabeled 4A06 suppressed radiotracer uptake in the tumour,

confirming that ^{89}Zr-4A06 accumulation in tumours is due to specific receptor binding. Radiotracer biodistribution in normal mouse tissues was unaffected by a "blocking" dose of 4A06, as expected. Lastly, a separate cohort of mice bearing HPAC tumours were treated with ^{18}F-FDG, the gold standard and most widely applied radiotracer for tumour detection. Remarkably, ^{18}F-FDG did not accumulate in the HPAC tumour to the same extent as the ^{89}Zr-4A06 radiotracer, suggesting that ^{89}Zr-4A06 may have advantages compared to ^{18}F-FDG for tumour detection (Figure 19).
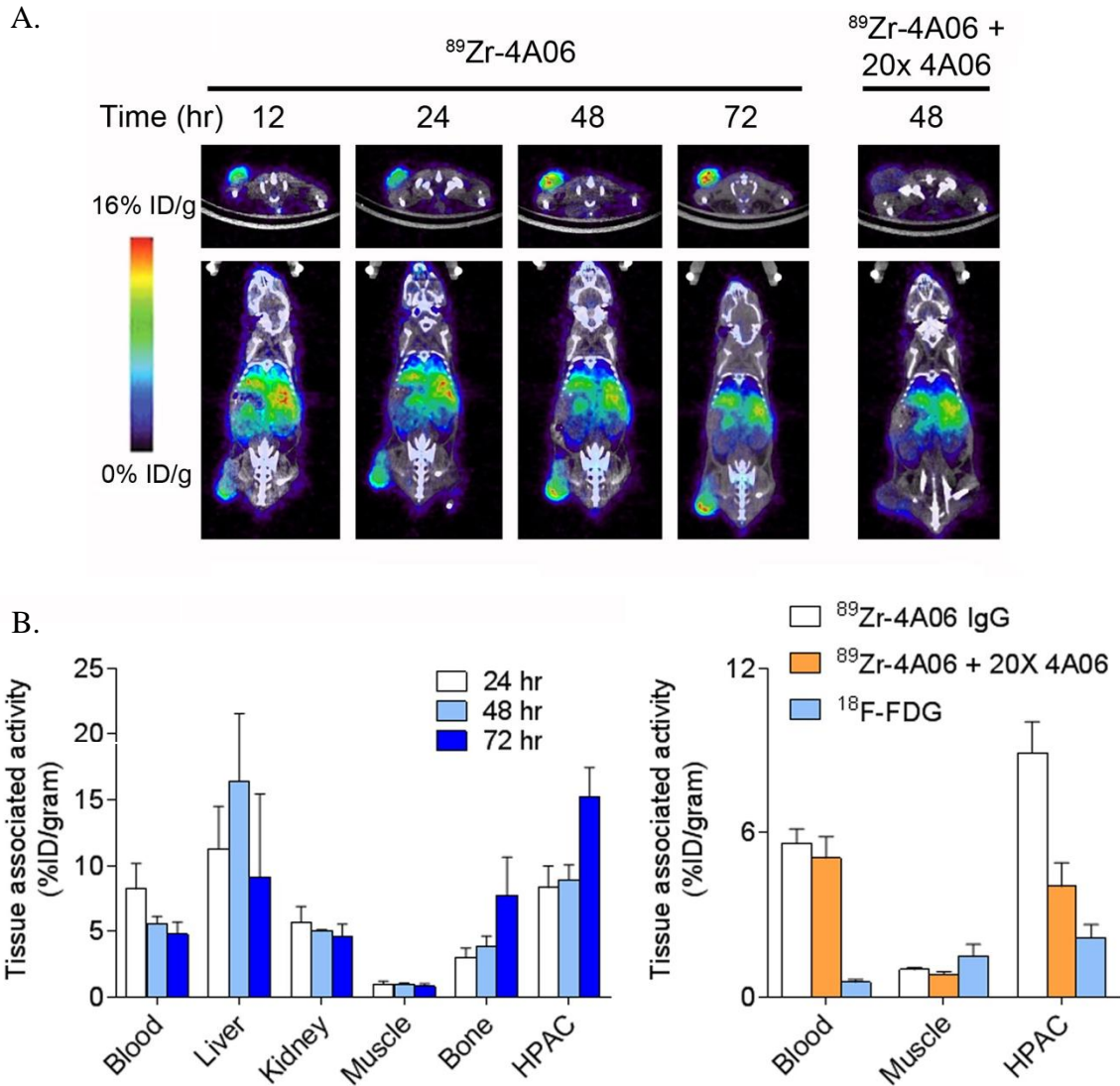
Figure 19. PET/CT and biodistribution data in animals injected with ^{89}Zr-4A06 (A). PET/CT (top) and biodistribution data (bottom) showing that ^{89}Zr-4A06 persistently associates with subcutaneous HPAC pancreatic cancer tumours after i.v. injection. Tumour uptake is significantly above the level observed in reference tissues (blood, muscle). (B). Biodistribution data collected 4 hours post injection show that heat-denatured (HD) ^{89}Zr-4A06 significantly suppresses radiotracer uptake in HPAC xenografts. ^{89}Zr-4A06 is also insubstantially taken up by A549 xenografts (blue), a tumour model with 50-fold lower CDCP1 expression compared to HPAC. *P<0.01 (Data are decay corrected).

While cell line models are routinely used in cancer research and are highly convenient, they are known to adopt or lose crucial biological features during the process of acclimation to *in vitro* culture conditions. On this basis, I next addressed the question if CDCP1 was expressed (or even over-expressed) in more clinically relevant patient derived

xenografts. PDX were generated from patients admitted to UC Medical Center with clear pancreatic ductal adenocarcinoma tumours. Flow cytometry of single cell suspensions with PE-labeled 4A06 showed that both PDXes expressed high levels of CDCP1.

Moreover, ^{89}Zr-4A06 detected subcutaneous implants of both PDXes in nu/nu mice at 48 hours post injection. Biodistribution studies showed that ^{89}Zr-4A06 accumulated in tumours to a level significantly above muscles, a standard reference tissue. To understand further the nature of the antibody-tumour interaction, PDXes were excised post mortem, and the intratumoral distribution of ^{89}Zr-4A06 was characterized with digital autoradiography (DAR). DAR images clearly showed high levels of ^{89}Zr-4A06 in sections from each PDX that overlapped with regions of viable tissue (defined by H&E). Moreover, the highest levels of ^{89}Zr-4A06 were detected around the outer rim of the PDX. This finding is consistent with the observation that large biomolecules like IgGs tend to have limited penetrance in dense tumour tissue (Data were decay corrected) (Figure 20).
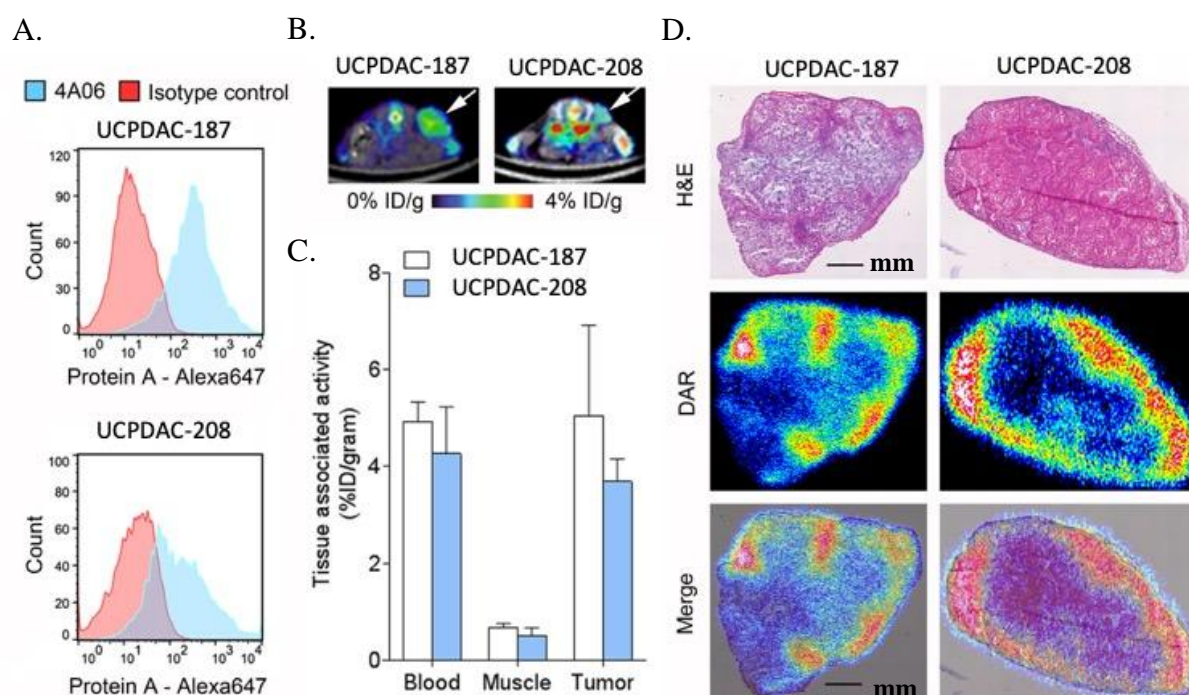
Figure 20. ^{89}Zr-4A06 detects pancreatic ductal adenocarcinoma in patient-derived xenografts (PDX). (A). Flow cytometry evaluation confirms CDCP1 expression in PDXs. UCPDAC-187 has higher CDCP1 expression, consistent with higher ^{89}Zr-4A06 uptake in vivo. (B). PET/CT images showing the biodistribution of ^{89}Zr-4A06 48 hours after injection in nu/nu mice bearing PDX derived from two different patients with PDAC. Tumour is highlighted with a white arrow. (C). Biodistribution data show the uptake of radiotracer significantly higher than the level of radiotracer observed in muscles (Data are decay corrected). (D). H&E staining of PDX tumours, digital autoradiography (DAR) showing penetration of PDX tumour by ^{89}Zr-4A06 and merged view.

6.1.2. ^{177}Lu-labeled 4A06 specifically detects tumour autonomous expression of CDCP1

The favourable imaging data in three discrete pancreatic cancer tumour models suggested that CDCP1 could be a useful target for radioimmunotherapy. To test this hypothesis more systematically, ^{177}Lu labeled 4A06 was synthesized by coupling of ^{177}Lu to DOTA chelators engineered onto the antibody backbone. The DOTA chelators were ligated to the IgG1 via solvent-exposed lysine side chains. The radiolabeling was performed using commercial ^{177}Lu-LuCl$_3$, and the radiochemical yield after 120 min was consistently >90% with a purity of >99%.

[177]Lu-4A06 was injected into male nu/nu mice bearing subcutaneous HPAC xenografts to estimate the amount of radioactivity absorbed by the tissue. SPECT/CT studies showed that the radiotracer accumulates in tumours from 4 – 96 hours post injection, with minimal uptake in normal mouse tissues as expected. At 48 hours post injection, little radiotracer was visualized in normal tissues, with the exception of the liver, which had persistently high uptake due to antibody clearance. Biodistribution studies conducted at 0.5, 4, 24, 48, and 96 hours post injection corroborated the trends suggested by the SPECT imaging data. The maximum tumour uptake of the radiotracer was ~15% ID/g at 48 hours post injection, while only the liver and the spleen (~18% ID/g) had substantial radiotracer uptake (Figure 21).

Using these data, the doses absorbed by the tumour and normal tissues were calculated. For tumours, there were a couple of assumptions. First, the model used for dose calculation is a sphere model, meaning the tumour volume is assumed to be a sphere. Second, only self-absorbed dose is calculated, namely the dose is calculated from the source (tumour) to the target (tumour). After manual segmentation of tumours, the last time point microSPECT/CT data were used to calculate the volume and accumulated activity by delineating the volume using both CT and SPECT images.
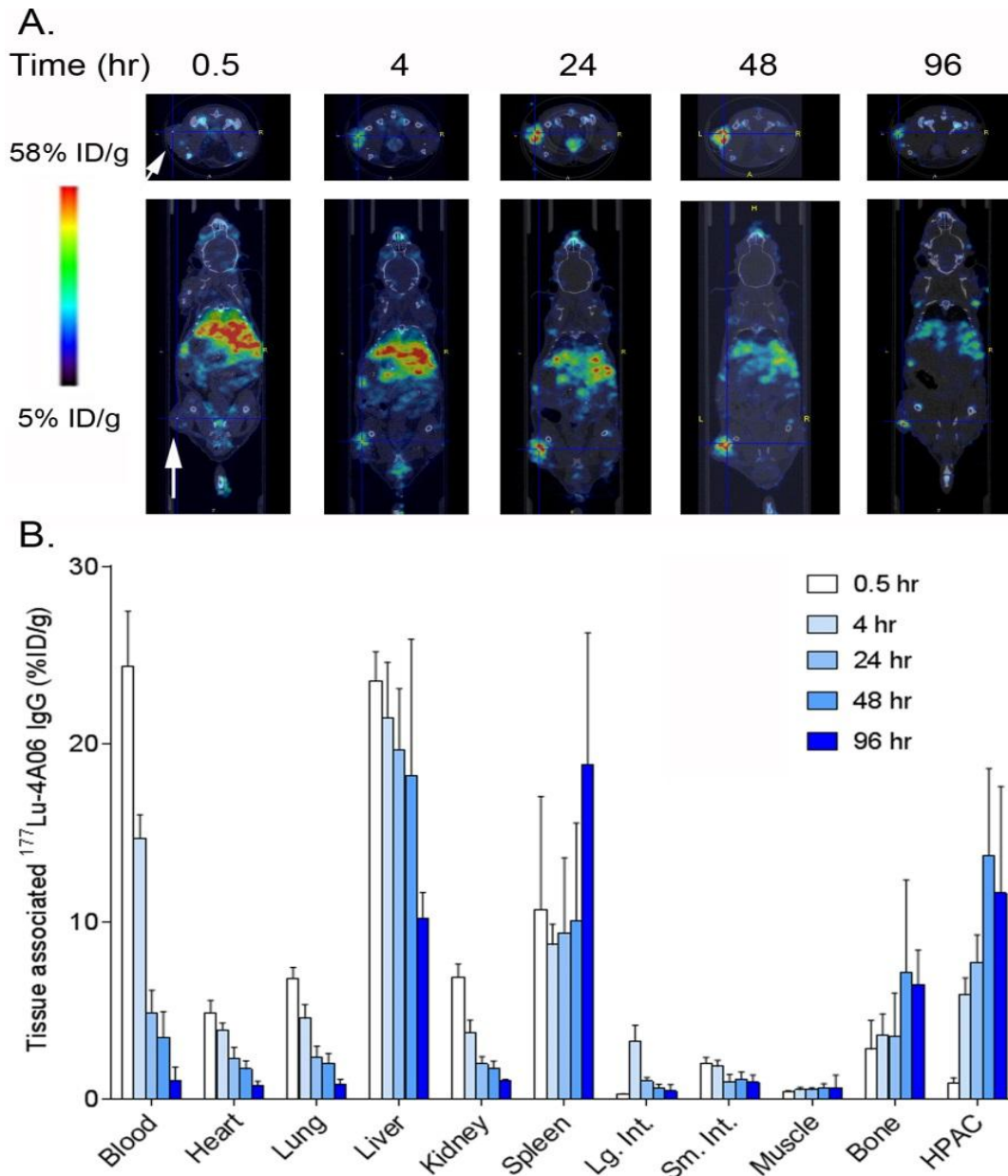
Figure 21. SPECT/CT and biodistribution data in animals injected with ^{177}***Lu-4A06.*** ***(A).*** *SPECT/CT data showing that* ^{177}*Lu-4A06 IgG is avidly taken up by subcutaneous HPAC tumours in vivo (white arrow).* ***(B).*** *Biodistribution data showing the high and persistent level of radiotracer uptake in HPAC tumours over time. Radiotracer uptake was observed in normal tissues like the liver and the spleen due to Fc receptor binding and clearance, as expected. Virtually no other normal tissue showed high radiotracer retention (Data are decay corrected).*

After the activity was divided by decay-corrected total injected activity in the body (i.e., percent of injected dose) for all time points and curve-fitting of the temporal data, residence times (in Bq-hr/Bq) were calculated. Using the sphere model in OLINDA|EXM (version 1.1),

the dose was calculated for a range of mass (0.01 – 6000 g). When the doses for different masses were calculated, a least-squares fit was used to derive a relationship between the dose and the mass as a continuous variable. After the volume was calculated from the manual segmentation assuming 1 g/ml density, the dose for each tumour was estimated from the fitted function, dose $= A \times (mass)^{-B}$ where A and B are parameters from the least-squares fit. With this methodology, the estimated dose to the tumours was 3.84, 4.89, and 1.78 mGy/MBq.

To determine the absorbed dose to normal tissues, volumes of interest (VOIs) were drawn from co-registered CT images for the brain, lungs, heart, liver, kidneys, and urinary bladder. All VOIs were cylinders (3 mm diameter and 5 mm height for the brain, 3 mm diameter and 3 mm height for the lungs, heart, and liver, and 2 mm diameter and 2 mm height for the kidneys and urinary bladder), and they were placed well within the anatomical boundaries to minimize the spill-over of radioactivity. The mean values (in Bq/ml) in these VOIs were multiplied by standard mouse organ volumes (in ml) to derive total activity within these organs. The total activity within the animal subtracted from all the organ activities was used as the activity in the remainder of the body. The percent of injected activity within the defined organs (%IA) was extrapolated to human-equivalent values using ratios of standard human organ weights to the mouse ones.

These input data were curve-fitted to derive residence times (in Bq-hr/Bq) and organ as well as effective doses for the data from each mouse. The data from the three animals were averaged to derive organ doses (in mGy/MBq) and effective dose (in mSv/MBq) using weighting factors published in ICRP Publication 60. Curve-fitting as well as organ and effective dose estimation were performed using OLINDA|EXM version 1.1 The doses to the normal tissues are outlined in Table 5.

Table 5. Dosimetry (OLINDA 1.1, ICRP60) estimated for ^{177}Lu-IgG using mouse imaging data.

Organ	Absorbed Dose (mGy/MBq) to adult male (73 kg)
Adrenals	8.65E-02
Brain	1.69E-02
Breasts	7.84E-02
Gallbladder Wall	9.13E-02
LLI Wall	8.29E-02
Small Intestine	8.40E-02
Stomach Wall	8.31E-02
ULI Wall	8.44E-02
Heart Wall	1.17E-01
Kidneys	7.97E-02
Liver	5.35E-01
Lungs	8.76E-02
Muscle	8.06E-02
Ovaries	8.37E-02
Pancreas	8.67E-02
Red Marrow	6.23E-02
Osteogenic Cells	2.50E-01
Skin	7.75E-02
Spleen	8.21E-02
Testes	7.99E-02
Thymus	8.12E-02
Thyroid	8.07E-02
Urinary Bladder Wall	1.86E-01
Uterus	8.40E-02
Total Body	9.64E-02
Effective Dose (mSv/MBq)	1.06E-01

6.1.3. An antitumour assessment study demonstrates that ^{177}Lu-4A06 suppresses pancreatic cancer tumour growth and extends overall survival

The study demonstrates that ^{177}Lu-4A06 suppresses pancreatic cancer tumour growth and extends overall survival: the SPECT/CT, biodistribution, and dosimetry data were highly promising, and a larger-scale antitumour assessment study was conducted. Intact male nu/nu mice bearing subcutaneous HPAC tumours (n = 5) were treated once with vehicle, unlabeled 4A06 (400 μg), and ^{177}Lu-4A06 (500 μCi/mouse, SA = 9.53 μCi/μg) intravenously. Tumour volume changes were measured twice a week via caliper to determine treatment-induced changes. The primary endpoint of the study was death (i.e. humane euthanasia) due to the tumour size in one dimension equal or more than 20mm.

Using this endpoint, the treatment arms of this study were statistically separated, and a Kaplan Meier analysis showed that mice receiving vehicle or unlabeled 4A06 survived for a shorter period compared to those treated with a single dose of ^{177}Lu-4A06 (Figure 22A). Moreover, at 20 days post treatment, the tumours in the ^{177}Lu-4A06 treatment arm were significantly smaller than those treated with vehicle or naked antibody (Figure 22B).
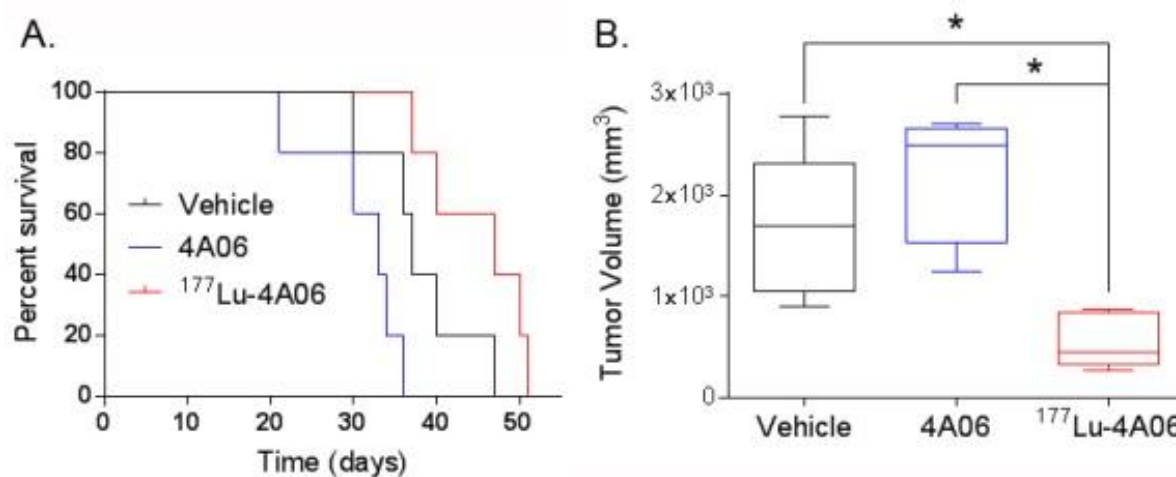
*Figure 22. ^{177}Lu-4A06 treatment study results. (A). A Kaplan Meier curve showing the survival of mice treated with vehicle, unlabeled 4A06 IgG, or ^{177}Lu-4A06 IgG. The median survival was significantly extended to 47 days for ^{177}Lu-4A06 compared to 37 and 33 days for the control arms. (B). A box-and-whiskers plot showing the tumour volumes for each treatment arm at 20 days, the final time point before any mice dropped out of the study due to reaching humane endpoint. The tumour volume was significantly lower in the ^{177}Lu-4A06 arm compared to the controls. *P<0.05*

6.2. Imaging of PD-L1 expression with ImmunoPET

6.2.1. *Synthesis and in vitro characterization of ^{89}Zr-labeled Atezolizumab*

Atezo was conjugated to the chelator desferrioxamine B (DFO) in the same way as it was described for 4A06. The affinity of DFO-atezo for the recombinant human ectodomain of PD-L1 was assessed *ex vivo* using biolayer interferometry (Fortebio, Octet Red384 system), and the K_D of the DFO-conjugated antibody was equivalent to naive atezo (1.8±0.09 nM and 1.9±0.2 nM, respectively). The chelate number per molecule of atezo was determined to be 2.26 ± 0.5 (Supplemental Figure 1A). DFO-atezo was radiolabeled via incubation with ^{89}Zr-oxalic acid for 120 min and purified using size exclusion chromatography. The radiochemical yield was consistently >95%, the radiochemical purity >98%, and the specific activity was 2.28 ± 0.4 µCi/µg over 5 independent radio syntheses (Supplemental Figure 1B).

All these values were compared favourably to those we achieved and reported for ^{89}Zr-C4, including a specific activity of ~7 µCi/µg.

6.2.2. *A comparison of the biodistribution of ^{89}Zr-Atezo and ^{89}Zr-C4 in tumour bearing immunocompetent and T cell deficient nu/nu mice*

The biodistribution of ^{89}Zr-atezo was first evaluated in immunocompetent C57BL/6J mice bearing subcutaneous B16 F10 tumours, a PD-L1 expressing mouse melanoma model that we previously showed to harbour high avidity for ^{89}Zr-C4. At a specific activity of 1.53 µCi/µg, ^{89}Zr-atezo had overall high accumulation in blood-rich abdominal tissues at early time points post injection, which generally declined from 24 to 72 hours, as expected (Figure 23A). Blood-associated activity also decreased from 4 to 48 hours. Persistent retention of ^{89}Zr-atezo from 24 to 72 hours was observed in the spleen, liver, kidney, lungs, small intestine, and bone. The uptake in the tumour increased from 4 to 24 hours, and remained constant at ~13% ID/g out to 96 hours. A separate cohort of tumour-bearing mice were treated with ^{89}Zr-atezo subjected to heat denaturation immediately prior to injection. Radiotracer accumulation in B16 F10 tumours was significantly reduced by heat denaturation, as expected.
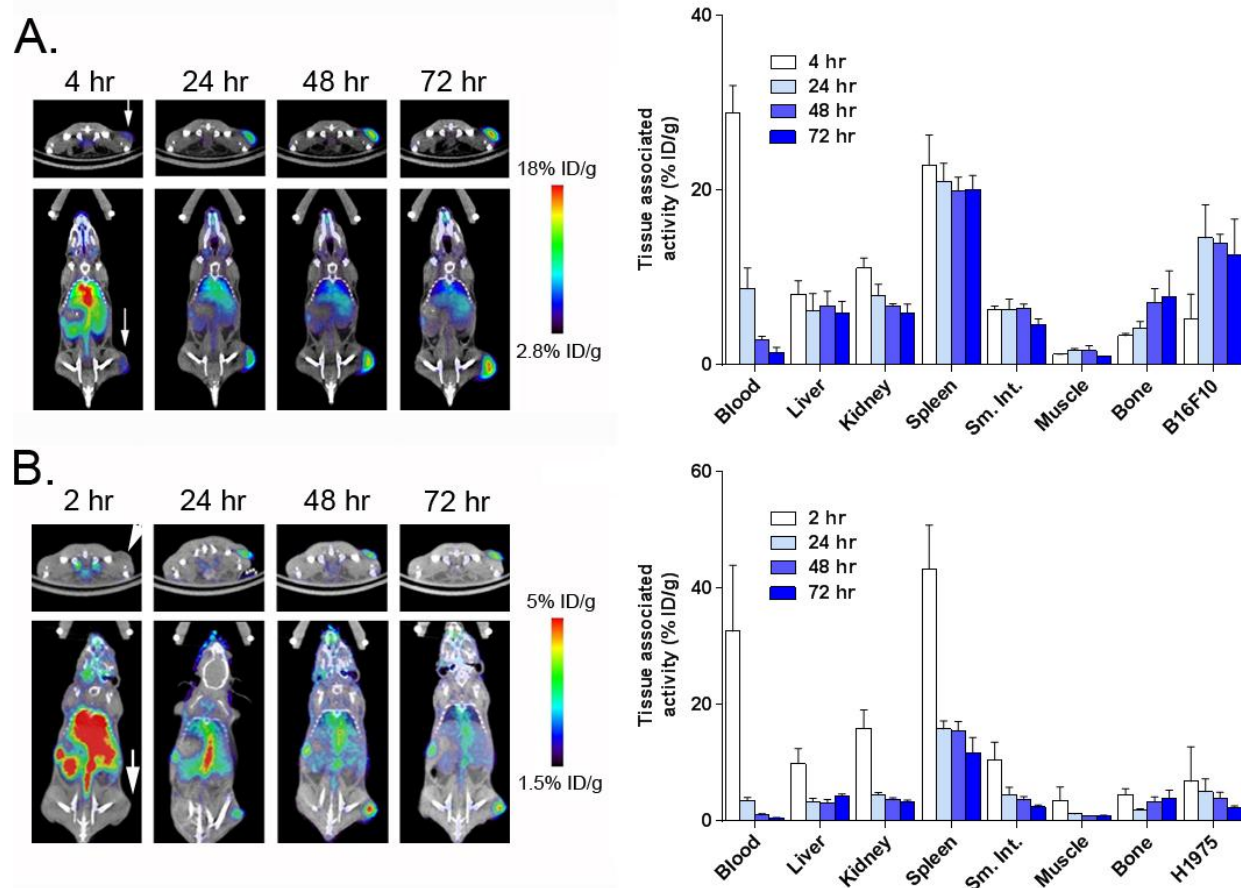
Figure 23. A summary of the biodistribution of ^{89}Zr-atezo over time in tumour-bearing animals. (A). ImmunoPET (left) and biodistribution studies (right) from selected tissues show the accumulation of ^{89}Zr-atezo in intact male C57BL/6J mice with subcutaneous B16F10 tumours. Persistently high uptake of the radiotracer was observed in the tumour, spleen, liver and kidney. The location of the tumour on PET/CT is indicated with a white arrow. ^{89}Zr-atezo was administered at a specific activity of 1.53 µCi/µg. (B). ImmunoPET (left) and biodistribution studies (right) from selected tissues show the accumulation of ^{89}Zr-atezo in intact male nu/nu mice with subcutaneous H1975 tumours. Similar qualitative trends in the biodistribution of normal tissues were observed compared to the data collected from C57BL/6J mice. Tumour uptake in H1975 was lower than that observed in B16F10 tumours, consistent with the relative expression levels of PD-L1. The location of the tumour on PET/CT is indicated with a white arrow. ^{89}Zr-atezo was administered at a specific activity of 2.17 µCi/µg (Data are decay corrected).

Table 6. A summary of the tumour to blood and tumour to muscle ratios derived from the biodistribution studies with ^{89}Zr-atezo outlined in Figure 1.

	Tumour: Blood		Tumour: Muscle	
	B16 F10	H1975	B16 F10	H1975
24 hours	1.76 ± 0.4	1.46 ± 0.2	8.97 ± 1.3	4.32 ± 0.4
48 hours	4.89 ± 0.6	3.96 ± 0.8	9.33 ± 3.2	4.79 ± 0.4
72 hours	10.25 ± 4.1	4.00 ± 0.6	13.06 ± 0.7	2.64 ± 0.4

The data referring to B16F10 tumours were acquired in the C57BL/6J mouse strain, while the data for H1975 were acquired in nu/nu mice.

The biodistribution of ^{89}Zr-atezo was next evaluated in immunocompromised intact male nu/nu mice bearing H1975 tumours, a human non-small cell lung cancer model with ~2.5 fold lower endogenous PD-L1 levels compared to B16 F10. At a specific activity of 2.17 μCi/μg, the pattern of radiotracer biodistribution in normal tissues from 2 to 72 hours was qualitatively similar to what was observed in C57Bl/6J mice, with the highest uptake observed in the spleen, liver, kidney, lung, small intestine, and bone. The retention of ^{89}Zr-atezo in H1975 tumours was above that in the blood and muscle as early as 24 hours post injection, and ~3.5-fold lower than B16 F10 (Figure 22B). Moreover, the tumour to blood and tumour to muscle ratios from both mouse strains suggested that optimal tumour detection requires at least 48 hours of uptake time (Table 6). Notably, ^{89}Zr-atezo retention was generally lower in the normal mouse tissues of nu/nu mice versus C57BL/6J. Since the specific activity of the ^{89}Zr-atezo formulation was higher in the nu/nu mouse cohort, the lower uptake likely reflects the reduced T-cell content of athymic nu/nu mice (Table 7).

Table 7. A summary of the biodistribution data for ^{89}Zr-atezo and ^{89}Zr-C4 in tumour-bearing mice at 48-hour post-injection.

Tissue	^{89}Zr-atezo	^{89}Zr-C4	^{89}Zr-atezo	^{89}Zr-C4
Blood	2.87 ± 0.4	2.17 ± 0.3	1.02 ± 0.2	2.87 ± 0.6
Heart	3.93 ± 0.3	0.96 ± 0.05	1.85 ± 0.3	1.08 ± 0.1
Lung	8.59 ± 0.8	0.89 ± 0.1	5.53 ± 0.9	1.79 ± 0.3
Liver	6.79 ± 1.6	7.33 ± 1.1	3.15 ± 0.5	8.16 ± 0.6
Kidney	6.71 ± 0.3	2.76 ± 0.8	3.60 ± 0.4	4.28 ± 0.7
Spleen	19.95 ± 1.5	6.05 ± 0.2	15.51 ± 1.6	6.48 ± 1.0
Pancreas	1.85 ± 0.2	0.49 ± 0.01	1.03 ± 0.07	0.57 ± 0.06
Lg. Int.	2.83 ± 0.3	0.68 ± 0.3	1.57 ± 0.2	0.51 ± 0.1
Sm. Int.	6.44 ± 0.5	0.59 ± 0.1	3.59 ± 0.6	0.73 ± 0.3
Stomach	1.75 ± 0.5	0.36 ± 0.1	0.89 ± 0.2	0.44 ± 0.1
Muscle	1.63 ± 0.6	0.73 ± 0.3	0.82 ± 0.07	0.47 ± 0.06
Bone	7.11 ± 1.64	2.62 ± 0.3	3.31 ± 0.8	2.87 ± 0.3
Brain	0.33 ± 0.02	0.27 ± 0.1	0.14 ± 0.08	0.16 ± 0.02
B16 F10	13.92 ± 1.0	13.83 ± 0.5	N/A	N/A
H1975	N/A	N/A	3.97±1.0	7.08±0.8

Immunocompetent intact male C57Bl/6J mice were inoculated subcutaneously with B16F10 in the flank, and immunocompromised athymic male nu/nu mice received subcutaneous H1975 tumours in the flank. C4 uptake in normal tissues was generally lower than atezo, with the notable exception of the liver and kidney. Abbreviations: Lg. Int. = large intestine, Sm. Int. = small intestine, N/A = not applicable. The specific activity of ^{89}Zr-atezo was 1.53 μCi/μg (B16 F10) and 2.17 μCi/μg (H1975). The specific activity of ^{89}Zr-C4 was previously determined to be 7 μCi/μg.

The comparison of the biodistribution patterns between ^{89}Zr-atezo and ^{89}Zr-C4 showed that the accumulation of both radiotracers in B16F10 tumours was equivalent, while the uptake of ^{89}Zr-atezo was significantly lower in H1975 tumours compared to ^{89}Zr-C4 (Table 7). This was accompanied by higher levels of ^{89}Zr-atezo in virtually all normal mouse tissues compared to ^{89}Zr-C4, suggesting that there may be a "sink effect" imparted by normal mouse

tissues that prevents ^{89}Zr-atezo from engaging the relatively modest levels of PD-L1 expressed on H1975. To test this hypothesis more systematically, the impact of added carrier was next evaluated (i.e. unlabeled atezo) on the biodistribution of ^{89}Zr-atezo.

6.2.3. *Investigating the impact of added carrier on the biodistribution of ^{89}Zr-atezo*

To identify the optimal carrier concentration, we first compared our preclinical biodistribution values to the available human data for ^{89}Zr-atezo. The human data showed equivalent accumulation of ^{89}Zr-atezo in normal organs like the spleen (~18% ID/kg), liver (~7% ID/kg), kidney (~5% ID/kg), and intestines (~5% ID/kg). The clinical formulation consisted of 1 mg ^{89}Zr-atezo with 10 mg of carrier added, and the mouse studies conducted with carrier-free ^{89}Zr-atezo suggested to us that increasing carrier beyond 10 molar excess may be required to impact ^{89}Zr-atezo biodistribution in mice.

On this basis, immunocompetent mice bearing subcutaneous B16 F10 tumours were co-injected with ^{89}Zr-atezo (specific activity = 2.45 µCi/µg) or ^{89}Zr-atezo with 15x excess unlabeled atezo (specific activity = 0.16 µCi/µg). At 48 hours post injection, the added carrier significantly reduced ^{89}Zr-atezo uptake in the spleen, small intestine, and bone (Figure 23A). The carrier also increased ^{89}Zr-atezo levels to a statistically significant extent in B16 F10 tumours. Further increasing the dose of added carrier to 30x in a separate cohort of mice only marginally improved the tumour to normal tissue ratios (Table 8). To further understand the mechanistic basis of tracer redistribution by carrier, an additional cohort of mice was co-injected with ^{89}Zr-atezo (specific activity = 2.45 µCi/µg) and 15x molar excess of an IgG1 isotype control. The isotype control did not alter ^{89}Zr-atezo biodistribution in normal or tumour tissues at 48 hours post injection, strongly suggesting that the added atezo carrier impacted radiotracer biodistribution through epitope/CDR interactions (Figure 24A). Inspection of the PET/CT imaging data and maximum intensity projections showed that the

atezo carrier effects on radiotracer biodistribution were visually obvious and consistent with the biodistribution data (Figure 24B and 24C).
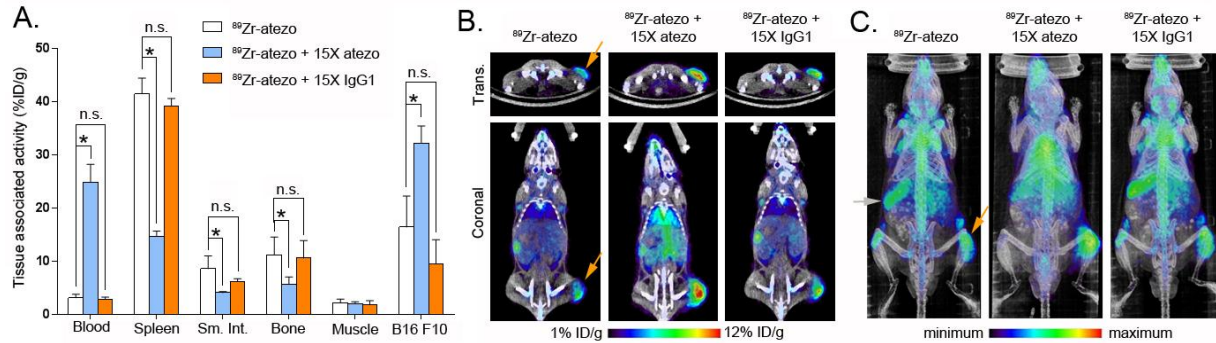
Figure 24. Added atezo carrier redistributes ⁸⁹Zr-atezo from normal tissues to tumours via a CDR-dependent mechanism. *(**A**). Biodistribution data acquired 48 hours post injection in immunocompetent C57BL/6J mice with subcutaneous B16F10 xenografts show that 15x atezo carrier suppresses ⁸⁹Zr-atezo uptake in normal PD-L1 rich mouse tissues, while the tumour uptake of the radiotracer increases. In contrast, co-administration of 15x excess unlabeled non-targeting human IgG1 isotype control does not alter the biodistribution of ⁸⁹Zr-atezo suggesting that the redistribution requires CDR interaction with its epitope on PD-L1. ⁸⁹Zr-atezo was prepared and used at a specific activity of 2.45 µCi/µg prior to dilution with atezo or IgG1 isotype control. *P < 0.01, n.s. = not significant. Data are decay corrected. (**B**). Representative coronal and transverse PET/CT images of mice from each treatment arm 48 hours post injection show the impact of added naked atezo carrier on tumour uptake of ⁸⁹Zr-atezo. The tumour is located on the right hind limb on each mouse and is highlighted in the ⁸⁹Zr-atezo treatment arm with an orange arrow. (**C**). Maximum intensity projections of the same mice also capture the redistribution of ⁸⁹Zr-atezo due to added atezo but not non-targeting IgG1 isotype control. The position of the tumour is highlighted with an orange arrow, and the position of the spleen is highlighted with a grey arrow.*

Table 8. A summary of the impact of added atezo carrier on the biodistribution of ^{89}Zr-atezo in immunocompetent C57Bl/6J mice bearing B16 F10 xenografts.

	Molar excess of added atezo carrier		
	0	15	30
Tumour: Spleen	0.64 ± 0.7	1.68 ± 0.1	1.42 ± 0.4
Tumour:Sm.Int.	2.35 ± 0.3	7.01 ± 0.2	10.55 ± 2.7
Tumour: Bone	2.29 ± 0.5	5.07 ± 1.0	6.53 ± 2.1
Tumour: Muscle	15.28 ± 0.9	15.82 ± 2.1	18.47 ± 2.2

Significant elevation of the tumour to normal tissue ratio was observed due to co-injection with 15x or 30x molar excess of naked atezo compared to carrier-free ^{89}Zr-atezo (specific activity 2.75 µCi/µg). The improvement was driven both by suppression of ^{89}Zr-atezo binding in normal tissues, and elevation of ^{89}Zr-atezo accumulation in tumour. No significant improvement was noted by elevating the dose of carrier from 15x to 30x. All data were collected 48 hours post injection of radiotracer formulation. Data represent the mean ± standard deviation.

A separate cohort of nu/nu mice bearing subcutaneous H1975 tumours were treated with ^{89}Zr-atezo (specific activity = 2.5 µCi/µg) or ^{89}Zr-atezo with 15x molar excess naked atezo (specific activity = 0.16 µCi/µg). At 48 hours post injection, the added carrier suppressed radiotracer uptake in normal mouse tissues, as expected, while elevating radiotracer uptake in the tumours (Figure 25A). The relative suppression of ^{89}Zr-atezo uptake in normal tissues due to the added carrier was essentially equivalent in both mouse strains, further underscoring that carrier added effects are likely due to interactions between the CDR and PD-L1 (Figure 25B).
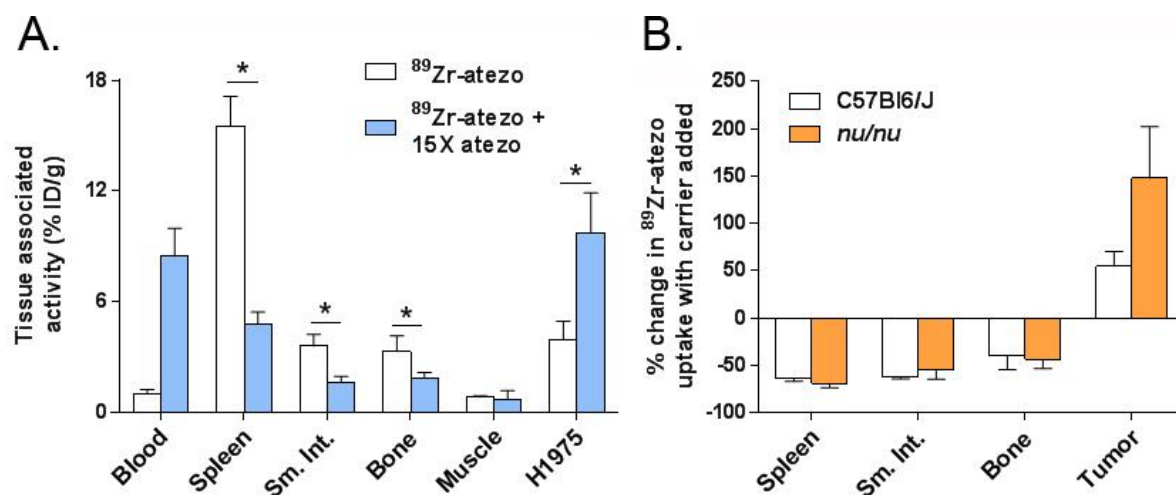
Figure 25. Added atezo carrier substantially elevates ^{89}Zr-atezo uptake in H1975 tumours in the T-cell deficient nu/nu background. (A). A summary of the biodistribution values for ^{89}Zr-atezo co-injected with 15x molar excess unlabeled atezo in nu/nu mice with subcutaneous H1975 tumours. As with the study in immunocompetent mice, radiotracer uptake was suppressed in PD-L1 rich normal tissues and elevated in the tumour. The biodistribution data were collected 48 hours post injection. ^{89}Zr-atezo was prepared at a specific activity of 2.5 μCi/μg prior to use with or without added atezo. *P<0.01 (B). A bar graph representing the percent change in radiotracer uptake due to added carrier among the immunocompetent and immunocompromised mouse cohorts. Suppression of ^{89}Zr-atezo uptake in normal mouse tissues by carrier atezo was substantial and equivalent among two mouse strains. Data are decay corrected.

6.3.   Targeting mTORC1 signaling to detect tuberous sclerosis complex and lymphangioleiomyomatosis with PET

Cell line models of TSC or LAM, while convenient, often require genetic manipulation to be further immortalized and maintained in culture. On this ground, I first tested if spontaneous growths arising in a genetically engineered mouse (GEM) model of TSC were detectable with ^{89}Zr-Tf PET. The A/J GEM model bears a germline deletion of one Tsc2 allele, and predominantly develops renal cystadenomas within one year [Onda et al, 1999]. Eight-month old male A/J mice were treated with ^{89}Zr-Tf, and the biodistribution of the radiotracer was studied at 48 hours post injection. Focal accumulation of the radiotracer within small regions of the transgenic kidneys was visually obvious on PET/CT (Figure

26A). Moreover, PET/CT of the surgically excised transgenic kidneys revealed numerous regions of high radiotracer uptake compared to wild type kidneys (Figure 26B). Digital autoradiography was performed to identify the source of the radioactivity, and the regions of the highest radiotracer accumulation co-localized with renal cystadenomas identified by H&E and phospho-S6 immunohistochemistry (Figure 26C).
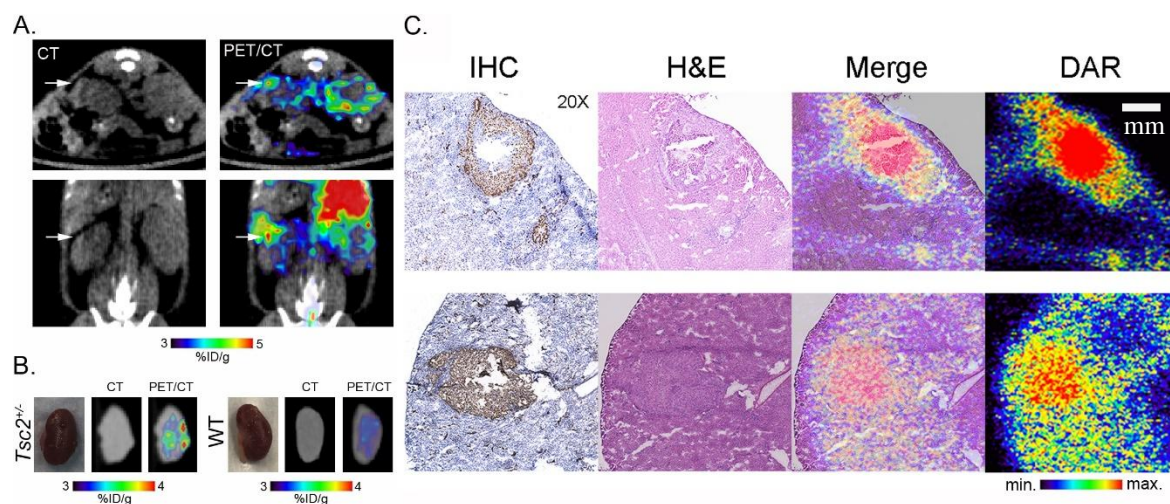
Figure 26. ^{89}Zr-Tf detects spontaneous benign renal cystadenomas arising in A/J Tsc2+/- mice. (A). CT and PET/CT images showing the biodistribution of ^{89}Zr-Tf 48 hours after injection in Tsc2+/- mice. Several regions of aberrant density on CT were observed without added contrast agent that co-aligned with foci of high ^{89}Zr-Tf uptake. One focus is highlighted with a white arrow. (B). PET/CT of surgically excised transgenic kidneys shows several regions of focal uptake of radiotracer significantly higher than the level of radiotracer observed in normal tissue. On the right a representative normal kidney from an immunocompetent mouse treated with an equivalent dose and uptake time of ^{89}Zr-Tf are shown. (C). Digital autoradiography (DAR) showing the co-localization of ^{89}Zr-Tf with renal cystadenomas, detected on H&E and phospho-S6 immunohistochemistry. Two representative cystadenomas are shown at 20X magnification. (Data are decay corrected).

To evaluate if TSC and LAM cell lines express TFRC and have avidity for Tf, TFRC expression and activity were next probed on cell line models of TSC *in vitro*. Immunoblot established that the *Tsc2* mutant cell lines tsc2 ang1 (mouse angiomyolipoma), 105K (mouse angiomyolipoma), ELT3 (rat LAM), and 621-101 (human LAM) express TFRC. Moreover,

TFRC was expressed in three TSC1 null human bladder cancer cell lines, HCV29, 97-1, and RT4. Cellular uptake assays with ^{125}I-labeled Tf showed that all cell lines bind and internalize Tf. We next performed *in vivo* studies to determine if tumours are avid for ^{89}Zr-Tf on PET. ^{89}Zr-Tf uptake was evaluated over time in intact female mice bearing subcutaneous ELT3 tumours, and tumours were clearly detectable on the flank of mice within 8 hours post i.v. injection of ^{89}Zr-Tf (Figure 26A). Moreover, serial imaging showed increasing retention of ^{89}Zr-Tf in the tumours from 8 to 48 hours. *Ex vivo* biodistribution studies corroborated the PET findings, as tumour uptake of ^{89}Zr-Tf rose from 8 to 72 hours post injection (Figure 27A). Moreover, tumour uptake of the radiotracer significantly exceeded blood pool- and muscle-associated activity at all time points post injection. A separate cohort of intact male mice bearing subcutaneous tsc2 ang1 tumours were treated with ^{89}Zr-Tf, and radiotracer biodistribution was studied over time. As with the ELT3 cohort, the xenografts were visualized within a day post injection, with peak radiotracer uptake in the tumour occurring between 24 and 48 hours post injection (Figure 27B). Lastly, a broader survey of ^{89}Zr-Tf uptake was conducted at 48 hours post injection in mice bearing the *Tsc2* and *Tsc1* mutant tumour models 105K, 621-101, 97-1 and RT4. ^{89}Zr-Tf uptake was detected in all the tumours at levels above background (Figure 27C).
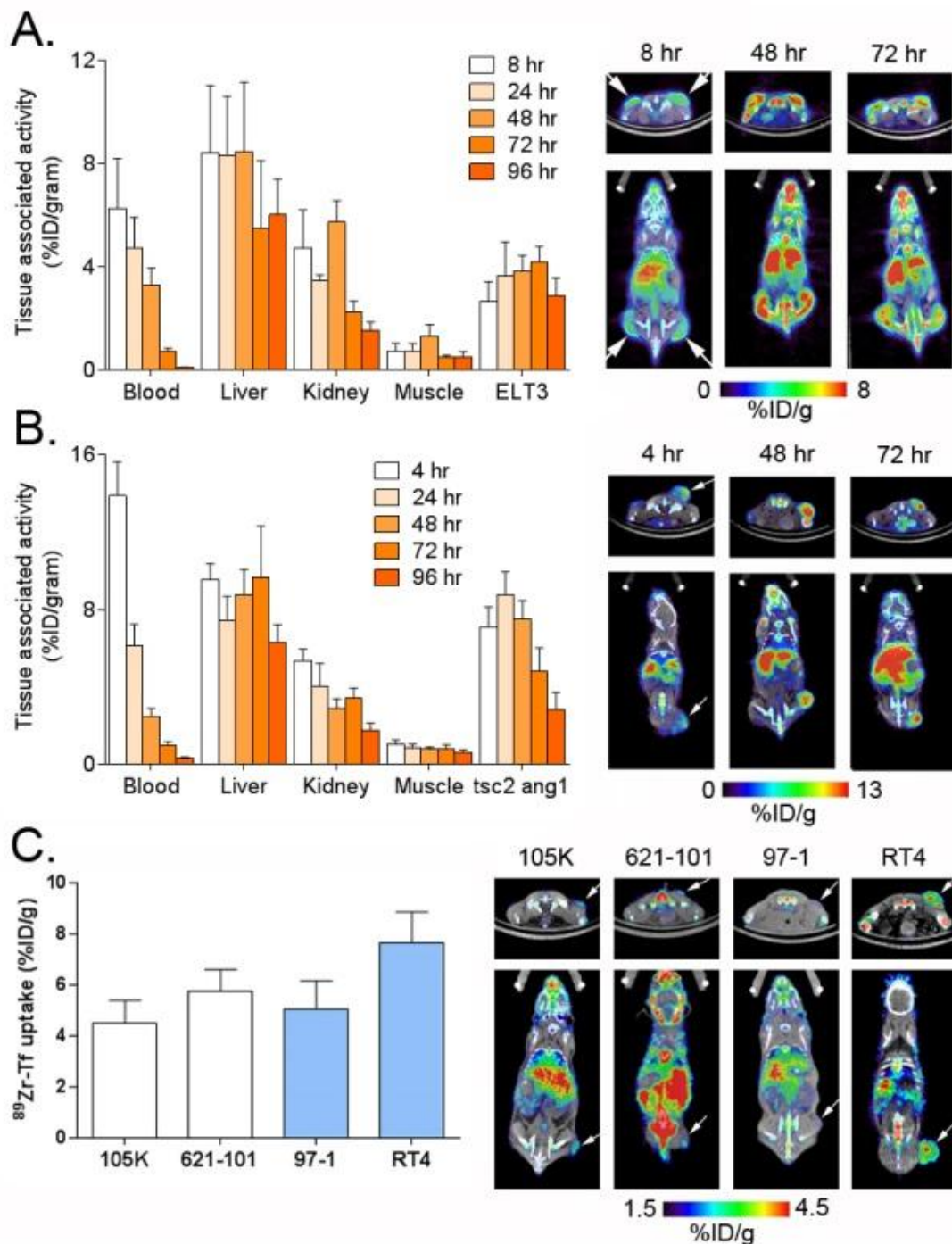
Figure 27. Multiple cell line models harbouring inactivating mutations in TSC1 or TSC2 are highly avid for ⁸⁹Zr-Tf. (A). On the left data depicting the biodistribution of ⁸⁹Zr-Tf in mice bearing subcutaneous ELT3 xenografts (a Tsc2 mutant model of LAM) are shown. Radiotracer uptake peaked in the ELT3 tumours between 24 and 72 hours post injection, consistent with the pharmacology of ⁸⁹Zr-Tf. Radiotracer uptake in representative normal tissues is also shown and has the expected degree of ⁸⁹Zr-Tf accumulation. On the right representative coronal and transverse PET/CT images from a mouse in the cohort are shown. The positions of the bilateral tumours are indicated with white arrows. (B). On the leftthe data depicting the biodistribution of ⁸⁹Zr-Tf in mice bearing subcutaneous tsc2 ang1

*xenografts (a Tsc2 mutant model of AML) are shown. Radiotracer uptake peaked in the tsc2 ang1 tumours and exceeded blood pool levels at 24 hours post injection. Radiotracer uptake in representative normal tissues is also shown and has the expected degree of ^{89}Zr-Tf accumulation. On the right representative coronal and transverse PET/CT images from a mouse in the cohort are shown. The positions of the xenografts are indicated with a white arrow. (**C**). On the left the tumour uptake values for ^{89}Zr-Tf acquired 48 hours post injection in mice bearing the indicated subcutaneous tumour are shown. All tumour values exceeded blood pool, strongly suggesting uptake due to specific binding. White bars indicate cell line models harbouring inactivating mutations in Tsc2, while blue bars highlight two human bladder cancer models with inactivating mutations in Tsc1. On the right representative PET/CT images are shown. The position of the xenograft is highlighted with a white arrow (Data are decay corrected).*

To test whether TFRC protein is upregulated in TSC models in an mTORC1-dependent fashion, we applied flow cytometry to ELT3 V3 and T3, isogenic pairs stably expressing an empty vector and a vector with a wild type *Tsc2* insert, respectively [Li et al, 2014]. TFRC levels were ~40% higher in ELT3 V3 compared to ELT3 T3, suggesting that restoration of wild type levels of the TSC1/TSC2 complex reduces TFRC expression (Figure 28A). Moreover, treating ELT3 V3 and 621-101 cells with the mTOR inhibitors RAD001, INK128, or BEZ235 decreased cell surface expression of TFRC. Importantly, treatment with a bioactive dose of doxorubicin did not impact TFRC levels, underscoring that the TFRC "response" is dependent on mTOR activity, and not simply associated with suppression of cellular proliferation and survival. *Tfrc* mRNA was also reduced by mTOR inhibitors. Lastly, cellular uptake of Tf was inhibited *in vitro* in the panel of cell lines with endogenous *Tsc1* or *Tsc2* mutations due to treatment with mTOR inhibitors (Figure 28B). Collectively, these data underscore that TFRC expression and Tf uptake is mTORC1 regulated in TSC and LAM cell lines.

To determine if treatment-induced changes in intracellular mTORC1 signaling are sufficiently large to be quantified with ^{89}Zr-Tf PET, mice bearing subcutaneous tsc2 ang1 tumours were treated daily via gavage for 5 days with RAD001 (10 mg/kg), BEZ235 (30

mg/kg), doxorubicin (5 mg/kg), or vehicle. Animals received [89]Zr-Tf intravenously on day 3, and PET and biodistribution studies were conducted 48 hours after radiotracer injection. Treatment with mTOR inhibitors significantly reduced tumour uptake of [89]Zr-Tf compared to vehicle and doxorubicin treatment (Figure 28C and 28D). BEZ235 treatment also reduced [89]Zr-Tf uptake in a separate cohort of mice bearing subcutaneous ELT3 tumours compared to vehicle or doxorubicin treatment, suggesting that [89]Zr-Tf PET can measure treatment-induced changes in mTORC1 signaling non-invasively.
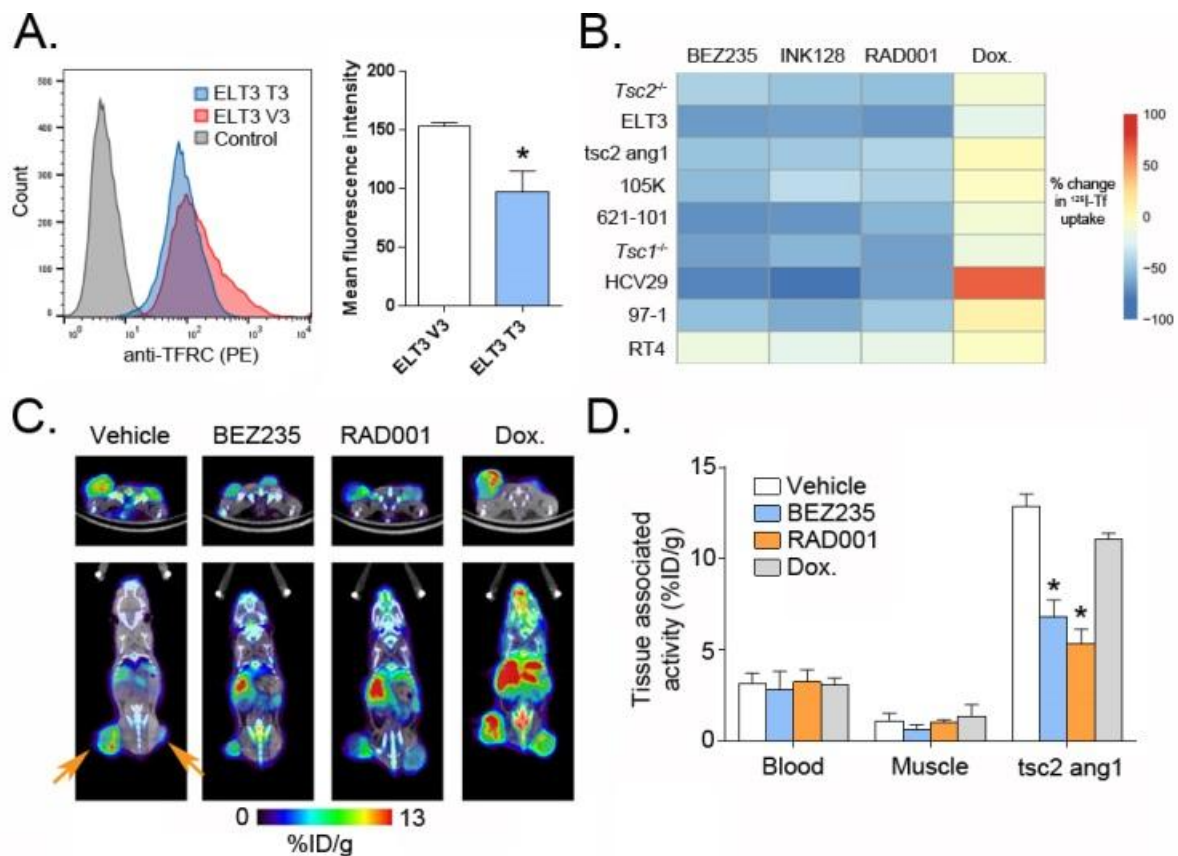
Figure 28. TFRC expression and Tf uptake is mTORC1 dependent in LAM and TSC models. (A). Flow cytometry data showing that cell surface expression levels of TFRC are higher in Tsc2 mutant ELT3 V3 cells compared to ELT T3, a subline with stable expression of wild type TSC2. Quantification of the mean fluorescence intensity from replicates shows that V3 cells have ~50% higher expression of cell surface TFRC. *P<0.01. (B). A heat map representing the percent change in ^{125}I-labeled Tf uptake in cells due to treatment with mechanistically discrete mTOR inhibitors (BEZ235, INK128, RAD001) or doxorubicin. Tf uptake is consistently repressed in Tsc1 or Tsc2 mutant cells, while a bioactive dose of doxorubicin does not alter Tf uptake (or mTORC1 activity). (C). Representative coronal and transverse PET/CT images showing the biodistribution of ^{89}Zr-Tf in mice bearing subcutaneous tsc2 ang1 tumours after prior treatment with vehicle, BEZ235 (30 mg/kg) RAD001 (10 mg/kg) or doxorubicin (5 mg/kg). ROI analysis at the tumour site showed a statistically significant decrease in ^{89}Zr-Tf uptake due to treatment with mTOR inhibitors compared to vehicle or doxorubicin treated mice. (D). Tumour biodistribution data from the animal cohort treated as described in C. Blood and muscle values are shown as reference tissues not expected to be impacted by drug treatment. *P<0.01 compared to vehicle treated mice. (Data are decay corrected).

Chapter 7. Discussion and Conclusions

My work aimed at devising new approaches to using the radiolabeled antibodies for diagnostics as well as therapy of RAS driven cancer. Besides the main project, two independent studies focusing on fields of mTOR regulation as well as checkpoint inhibitors were conducted working on the goal of developing new strategies for cancer treatment and molecular imaging.

By conducting the main study, I have successfully confirmed that Cub domain containing protein 1 (CDCP1) may serve as a target for visualization and treatment of RAS driven cancer cells on the example of pancreatic cancer CDX and PDX models. Furthermore, we have demonstrated the ability of ^{89}Zr-labeled and ^{177}Lu-labeled 4A06 antibody to stably bind to CDCP1 and act as a delivery system for Immuno/PET imaging and Immuno/SPECT imaging. Moreover, the data allowed me to successfully present the first RAS targeted therapy based on ^{177}Lu-4A06 Abs, which reliably inhibits tumour growth in the pancreatic cancer model.

Our strategy for the second project exploited a functional connection between a loss of TSC1/2, and an mTORC1-dependent increase in cell surface TFRC expression and Tf uptake into cells. Importantly, ^{89}Zr-Tf detected renal cystadenomas spontaneously arising in a GEM model of TSC. Moreover, a pathologically diverse panel of TSC and LAM cell lines bore high avidity for Tf in an mTORC1-dependent fashion. Lastly, a short term treatment of TSC and LAM xenografts with mechanistically discrete mTORC1 inhibitors showed that intracellular changes in mTORC1 signaling can be measured with ^{89}Zr-Tf PET prior to the onset of volumetric regression. A novel molecular imaging approach that may improve the detecting and monitoring the clinically problematic cells arising from TSC and/or LAM was described herein.

Lastly, my colleagues and I took advantage of the increase in availability of experimental imaging technologies to non-invasively measure immune checkpoint protein expression which presented the opportunity for rigorous comparative studies towards identifying a gold standard. ^{89}Zr-atezolizumab is currently in man, and early data show tumour targeting as well as abundant uptake in several normal tissues. Therefore, I conducted a reverse translational study both to understand if tumour to normal tissue ratios for ^{89}Zr-atezolizumab could be improved and to make direct comparisons to ^{89}Zr-C4, a radiotracer that we proved to be capable of detecting a large dynamic range of tumour-associated PD-L1 expression. PET/ CT and biodistribution studies in tumour-bearing immunocompetent and nu/nu mice revealed high specific activity of ^{89}Zr-atezolizumab (~2 µCi/µg) binding to PD-L1 on tumours but also resulting in a very high uptake in many normal mouse tissues, as expected. Unexpectedly, ^{89}Zr-atezolizumab uptake was generally higher in normal mouse tissues compared to ^{89}Zr -C4 and lower in H1975, a tumour model with modest PD-L1 expression. Unexpectedly as well, reducing the specific activity at least 15-fold suppressed ^{89}Zr-atezo uptake in normal mouse tissues but increased the tumour uptake to levels observed with high specific activity of ^{89}Zr-C4.

RAS / CDCP1 research

Up to date A406 is the only anti-CDCP1 antibody with a high potential to become both a diagnostic tool and a therapeutic agent. Previously studied antibodies such as RG7287 [G. Kollmorgen et Al., 2016] were never reported to get into clinical trials. My research is contributing to solving the challenge of targeting RAS pathway being critical in cancer research of the last decade. This pathway is commonly regarded as undruggable, while it drives various cancers in nearly a million new patients every year. My approach represents a new way to directly target RAS driven tumours and is in unison with multiple drugs targeting

downstream pathways, such as Panitumumab (EGFR inhibitor), Pimasertib, Tramatinib (MEK-inhibitor) being at early stages of clinical TRIALs. No other credible options are discovered to date.

Assessing the tumour progression and treatment response as well as tumour disease burdens is a crucial part of cancer treatment, especially for ones requiring surgical resection. I have shown 4A06 to be a promising diagnostic tool with high tumour to blood and tumour to muscle ratios. Since 89Zr is actually in clinics (Groningen group), it can be urged to the first in-human PET-CT visualization. Even though the cytotoxic potential of 4A06 was shown using Jurkat/NFAT T-cell model, a lot of studies are to be done. Future prospective includes developing mice cross-reactive antibody to test cytotoxic and other downstream effect of 4A06 in mice cancer cell line models and GEM models. Other avenue to discover is to target new types of cancer and look outside of RAS-mutation pathway, including colon lung breast cancer, prostate and kidney cancer. Potential combination therapy with check point inhibitors (PD-L1/PD-1, CTLA4 blockade) or with anti-EGFR antibodies to overcome resistance to such treatment remains to be studied.

mTOR / Transferrin

By conducting the second study I have successfully confirmed a new molecular imaging approach that may improve the detection and monitoring of clinically problematic cells arising from TSC and/or LAM. The strategy exploits a functional connection between a loss of TSC1/2, and an mTORC1-dependent increase in cell surface TFRC expression and Tf uptake into cells. Importantly, ^{89}Zr-Tf detected renal cystadenomas spontaneously arising in a GEM model of TSC. Moreover, a pathologically diverse panel of TSC and LAM cell lines bore high avidity for Tf in an mTORC1 dependent fashion. Lastly, a short-term treatment of TSC and LAM xenografts with mechanistically discrete mTORC1 inhibitors showed that

intracellular changes in mTORC1 signaling can be measured with ^{89}Zr-Tf PET prior to the onset of volumetric regression.

The limited clinical data suggest that conventional PET/CT is not useful for studying benign disease burden, as angiomyolipoma and LAM are not avid for ^{18}F-fluorodeoxyglucose (FDG). Malignant angiomyolipoma is detectable with ^{18}F-FDG and ^{11}C-acetate PET; however, the overall risk of developing malignancies due to TSC or LAM is minimal. ^{11}C-methyl-L-tryptophan PET may be useful to detect epileptogenic brain tubers, though its mechanism of action makes this radiotracer unlikely to be useful for detecting disease outside the brain.

While ^{89}Zr-Tf is experimental and not ready to be tested in humans, PET studies with ^{68}Ga-citrate were performed, which potently binds to apo-Tf after i.v. administration [Larson et al, 1978]. In preclinical tumour models, ^{68}Ga-citrate has a virtually identical biodistribution to ^{89}Zr-Tf, despite a significantly shorter uptake time (4 versus 48 hours). Moreover, ^{68}Ga-citrate PET/CT and PET/MR studies were conducted in over 20 patients with castration-resistant prostate cancer and hepatocellular carcinoma at UCSF since 2015. That ^{68}Ga-citrate is avidly taken up by these tumour types, known to have mTORC1 hyperactivity, gives us optimism that the encouraging preclinical data with ^{89}Zr-Tf will be translated into meaningful clinical findings for TSC and LAM patients when imaged with ^{68}Ga-citrate PET. Considering the facts discussed above, next step for the project is to show proof-of-concept clinical imaging studies to this end.

Checkpoint inhibitors / Atezolizumab

Measuring PD-L1 with non-invasive imaging is an unusual clinical challenge, as it need not be overexpressed to promote tumour growth, and patients with as little as 1% of PD-L1 positive cells on immunohistochemistry can experience durable clinical responses to anti-

PD-1/PD-L1 therapies. Therefore, the ideal non-invasive companion diagnostic should be capable of measuring the largest possible dynamic range of PD-L1 expression to accommodate the diversity of antigen expression that is presented clinically. ^{89}Zr-atezo requires a trial to determine if a specific activity can be identified that reveals antigen on tumours with low expression without blocking binding to tumours with abundant antigen expression. Alternatively, ^{89}Zr-C4 may be more straightforward to implement clinically, as high specific activity formulations result in higher binding to tumour with lower "background" in normal tissues compared to ^{89}Zr-atezo. Why ^{89}Zr-C4 differs from ^{89}Zr-atezo in this regard is currently unclear. The difference is likely to be unrelated to recognizing discrete subpopulations of endogenous PD-L1, as unlabeled atezo or C4 were both found to be effective, albeit to different extent, at suppressing the binding of ^{89}Zr-atezo to natively expressed PD-L1 on B16F10 cells *in vitro*. One of further steps is to understand the basis for the biodistribution differences, as well as to prepare ^{89}Zr-C4 for a clinical trial in which its ultimate utility can be assessed. Moreover, the findings from this study argue strongly for further studies to determine if tumour measurement of PD-L1 by emerging low molecular weight constructs also requires low specific activities [Chatterjee et al, 2017]. In summary, these reverse translational studies with ^{89}Zr-atezo have revealed a special importance of lower specific activity to measure tumour-associated PD-L1, especially for tumours with modest antigen expression.

Overall, I have conducted numerous preclinical studies going significantly beyond the scope of previously published work yet still in demand in this area of cancer research. It resulted in validation of CDCP1 as a prominent target for both diagnostics and treatment using antibodies labeled with ^{89}Zr and ^{177}Lu as well as confirming that ^{89}Zr labeled transferrin can be successfully used in preclinical and, with more detailed studies, clinical cases involving tuberoslerosis in cancer. Our data on ^{89}Zr labeled Atezo vs C4 antibodies

demonstrate some intrigue as of how to build up on it, but also a clear path for successful Immuno/PET studies using these agents.

Bibliography

1. Aghevlian S, Boyle AJ, Reilly RM. Radioimmunotherapy of cancer with high linear energy transfer (LET) radiation delivered by radionuclides emitting α-particles or Auger electrons. Adv Drug Deliv Rev. 2017 Jan 15;109:102-118. doi: 10.1016/j.addr.2015.12.003. Epub 2015 Dec 17.

2. Aguirre-Portolés Cristina, Lara P. Fernández, Ana Ramírez de Molina Precision Nutrition for Targeting Lipid Metabolism in Colorectal Cancer Nutrients. 2017 Oct; 9(10): 1076. Published online 2017 Sep 28. doi: 10.3390/nu9101076 PMCID: PMC5691693.

3. Ahearn IM, Haigis K, Bar-Sagi D, Philips MR. Regulating the regulator: post-translational modification of RAS. Nat Rev Mol Cell Biol. 2011 Dec 22;13(1):39-51. doi: 10.1038/nrm3255. Review. PubMed PMID: 22189424; PubMed Central PMCID: PMC3879958.

4. Alajati A, Guccini I, Pinton S, Garcia-Escudero R, Bernasocchi T, Sarti M, Montani E, Rinaldi A, Montemurro F, Catapano C, Bertoni F, Alimonti A. Interaction of CDCP1 with HER2 enhances HER2-driven tumorigenesis and promotes trastuzumab resistance in breast cancer. Cell Rep. 2015 Apr 28;11(4):564-76. doi: 10.1016/j.celrep.2015.03.044. Epub 2015 Apr 16. PubMed PMID: 25892239.

5. Alberts B, Johnson A, Lewis J, et al. Molecular Biology of the Cell. 4th edition. New York: Garland Science; 2002. B Cells and Antibodies.

6. Aluicio-Sarduy E et al PET radiometals for antibody labeling. J Labelled. Comp Radiopharm 2018 Jul;61(9):636-651. doi: 10.1002/jlcr.3607. Epub 2018 Mar 12.

7. Anderson CJ, Connett JM, Schwarz SW, Rocque PA, Guo LW, Philpott GW, et al. Copper-64-labeled antibodies for PET imaging. J Nucl Med. 1992;33:1685–90.

8. André M, Le Caer JP, Greco C, Planchon S, El Nemer W, Boucheix C, Rubinstein E, Chamot-Rooke J, Le Naour F. Proteomic analysis of the tetraspanin web using LC-ESI-MS/MS and MALDI-FTICR-MS. Proteomics. 2006 Mar;6(5):1437-49. PubMed PMID: 16404722.

9. Appels, N. M. G. M., Beijnen, J. H. & Schellens, J. H. M. Oncologist 10, 565–578 (2005).

10. Ashutosh Dash Maroor Raghavan Ambikalmajan Pillai, and Furn F. Knapp, Jr. Production of 177Lu for Targeted Radionuclide Therapy: Available Options Nucl Med Mol Imaging. 2015 Jun; 49(2): 85–107. Published online 2015 Feb 17. doi: 10.1007/s13139-014-0315-z.

11. Backer MP, Metzger LS, Slaber PL, Nevitt KL, Boder GB. Large-scale production of monoclonal antibodies in suspension culture. Biotechnol Bioeng. 1988 Oct 5;32(8):993-1000. PubMed PMID: 18587817.

12. Barbacid M. Ras genes. Annu Rev Biochem. 1987;56:779-827. Review. PubMed PMID: 3304147.

13. Bauer AJ Gieschler S Lemberg KM McDermott AE Stockwell BR Functional model of metabolite gating by human voltage-dependent anion channel 2.Biochemistry. 2011 May 3;50(17):3408-10. doi: 10.1021/bi2003247. Epub 2011 Apr 6.

14. Bensch, F., van der Veen, E., Jorritsma, A., Lub-de Hooge, M., Boellaard, R., Oosting, S., Schroder, C., Hiltermann, J., van der Wekken, A., Groen, H., et al. (2017) First in human PET imaging with the PD-L1 antibody 89Zr-atezolizumab. Cancer research 77, Abtract nr CT017.

15. Berger R., Rotem-Yehudar R., Slama G., Landes S., Kneller A., Leiba M., et al. (2008). Phase I safety and pharmacokinetic study of CT-011, a humanized antibody interacting with PD-1, in patients with advanced hematologic malignances. Clin.

Cancer Res. 14, 3044–3051. 10.1158/1078-0432.CCR-07-4079.

16. Bockisch A, Freudenberg LS, Schmidt D, Kuwert T. Hybrid imaging by SPECT/CT and PET/CT: proven outcomes in cancer imaging. Semin Nucl Med. 2009 Jul;39(4):276-89. doi: 10.1053/j.semnuclmed.2009.03.003.

17. Bryan, J. N., Jia, F., Mohsin, H., Sivaguru, G., Anderson, C. J., Miller, W. H., Henry, C. J., and Lewis, M. R. (2011) Monoclonal Antibodies for Copper-64 PET Dosimetry and Radioimmunotherapy. Cancer Biol. Ther. 11, 1001−1007.

18. Bühring HJ, Kuçi S, Conze T, Rathke G, Bartolović K, Grünebach F,Scherl-Mostageer M, Brümmendorf TH, Schweifer N, Lammers R. CDCP1 identifies a broad spectrum of normal and malignant stem/progenitor cell subsets of hematopoietic and nonhematopoietic origin. Stem Cells. 2004;22(3):334-43. PubMed PMID: 15153610.

19. Cai J, Li F. Single-photon emission computed tomography tracers for predicting and monitoring cancer therapy. Curr Pharm Biotechnol. 2013;14(7):693-707.

20. Cai WB, Chen K, He LN, Cao QH, Koong A, Chen XY. Quantitative PET of EGFR expression in xenograft-bearing mice using Cu-64-labeled cetuximab, a chimeric anti-EGFR monoclonal antibody. Eur J Nucl Med Mol I. 2007;34:850–8.

21. Campbell SL, Khosravi-Far R, Rossman KL, Clark GJ, Der CJ. Increasing complexity of Ras signaling. Oncogene. 1998 Sep 17;17(11 Reviews):1395-413. Review. PubMed PMID: 9779987.

22. Chatterjee, S., Lesniak, W. G., Gabrielson, M., Lisok, A., Wharram, B., Sysa-Shah, P., Azad, B. B., Pomper, M. G., and Nimmagadda, S. (2016) A Humanized Antibody for Imaging Immune Checkpoint Ligand PD-L1 Expression in Tumors. Oncotarget 7, 10215−10227.

23. Chan SM, Hoffer PB, Maric N, Zoghbi SS, Kirkwood JM, Ernstoff MS, Duray PH,

Gerich B.Comparison of gallium-67 versus indium-111 monoclonal antibody (96.5, ZME-018) in detection of human melanoma in athymic mice. J Nucl Med. 1987 Sep;28(9):1441-6.

24. Chatterjee, S., Lesniak, W. G., Miller, M. S., Lisok, A., Sikorska, E., Wharram, B., Kumar, D., Gabrielson, M., Pomper, M. G., Gabelli, S. B., et al. (2017) Rapid PD-L1 Detection in Tumors with PET Using a Highly Specific Peptide. Biochem. Biophys. Res. Commun. 483, 258−263.

25. Chiu Kuo-Liang, Yu-Sen Lin, Ting-Ting Kuo, Chia-Chien Lo, Yu-Kai Huang, Hsien-Fang Chang, Eric Y. Chuang, Ching-Chan Lin, Wei-Chung Cheng, Yen-Nien Liu, Liang-Chuan Lai, Yuh-Pyng Sher ADAM9 enhances CDCP1 by inhibiting miR-1 through EGFR signaling activation in lung cancer metastasis Oncotarget. 2017 Jul 18; 8(29): 47365–47378. Published online 2017 May 7. doi: 10.18632/oncotarget.17648 PMCID: PMC5564571.

26. Christiansen JR, Kolandaivelu S, Bergo MO, Ramamurthy V. RAS-converting enzyme 1-mediated endoproteolysis is required for trafficking of rod phosphodiesterase 6 to photoreceptor outer segments. Proceedings of the National Academy of Sciences of the United States of America. 2011;108(21):8862-8866. doi:10.1073/pnas.1103627108.

27. Conze T, Lammers R, Kuci S, Scherl-Mostageer M, Schweifer N, Kanz L, Buhring HJ. CDCP1 is a novel marker for hematopoietic stem cells. Ann N Y Acad Sci. 2003 May;996:222-6. PubMed PMID: 12799299.

28. Cousin S, Grellety T, Toulmonde M, Auzanneau C, Khalifa E, Laizet Y, Tran K,Le Moulec S, Floquet A, Garbay D, Robert J, Hostein I, Soubeyran I, Italiano A. Clinical impact of extensive molecular profiling in advanced cancer patients. JHematol Oncol. 2017 Feb 8;10(1):45. doi: 10.1186/s13045-017-0411-5. PubMed PMID: 28179005;

PubMed Central PMCID: PMC5299780.

29.   Cox AD, Der CJ. Ras history: The saga continues. Small GTPases. 2010 Jul;1(1):2-27. PubMed PMID: 21686117; PubMed Central PMCID: PMC3109476.

30.   Cox AD, Fesik SW, Kimmelman AC, Luo J, Der CJ. Drugging the undruggable Ras: mission possible? Nature reviews Drug discovery. 2014;13(11):828-851. doi:10.1038/nrd4389. de la Cruz, F. F., Gapp, B. V. & Nijman, S. M. B. Annu. Rev. Pharmacol. Toxicol. 55, 513–531 (2015).

31.   Crino, P.B., Nathanson, K.L., and Henske, E.P. 2006. The tuberous sclerosis complex. N Engl J Med 355:1345-1356.; Patel, S. P., and Kurzrock, R. (2015) PD-L1 Expression as a Predictive Biomarker in Cancer Immunotherapy. Molecular cancer therapeutics 14, 847-56.

32.   Cullen PJ, Lockyer PJ. Integration of calcium and Ras signaling. Nat Rev Mol Cell Biol. 2002 May;3(5):339-48. Review. PubMed PMID: 11988768.

33.   Daniels M.A. et Al. Thymic selection threshold defined by compartmentalization of RAS/MAPK signaling. Nature 444, 724-729 2006.

34.   Deer EL, Gonzalez Hernandez J, Coursen JD, Shea JE, Ngatia J, Scaife CL, Firpo MA, Mulvihill SJ. Phenotype and genotype of pancreatic cancer cell lines. Pancreas. 2010 May;39(4):425-35. doi: 10.1097/MPA.0b013e3181c15963. Review.

35.   Deryugina E et al, Functional Role of Cell Surface CUB Domain-Containing Protein 1 (CDCP1) in Tumor Cell Dissemination Mol Cancer Res. 2009 Aug; 7(8): 1197–1211. doi: 10.1158/1541-7786.MCR-09-0100.

36.   Dijkers ECF, Kosterink JGW, Rademaker AP, Perk LR, van Dongen GAMS, Bart J, et al. Development and characterization of clinical-grade 89Zr-trastuzumab for HER2/neu immunoPET imaging. J Nucl Med. 2009;50:974–81.

37.   Dijkers EC, Munnink THO, Kosterink JG, Brouwers AH, Jager PL, de Jong JR, et al.

Biodistribution of 89Zr-trastuzumab and PET imaging of HER2-positive lesions in patients with metastatic breast cancer. Clin Pharmacol Ther. 2010;87:586–92.

38. Dirican N, Duman A, Sağlam G, et al. The diagnostic significance of signal peptide-complement C1r/C1s, Uegf, and Bmp1-epidermal growth factor domain-containing protein-1 levels in pulmonary embolism. Annals of Thoracic Medicine. 2016;11(4):277-282. doi:10.4103/1817-1737.191876.

39. Donnelly, D. J., Smith, R. A., Morin, P., Lipovsek, D., Gokemeijer, J., Cohen, D., Lafont, V., Tran, T., Cole, E. L., Wright, M., Kim, J., Pena, A., Kukral, D., Dischino, D. D., Chow, P., Gan, J., Adelakun, O., Wang, X. T., Cao, K., Leung, D., Bonacorsi, S. J., Jr., and Hayes, W. (2018) Synthesis and Biologic Evaluation of a Novel (18)F-Labeled Adnectin as a PET Radioligand for Imaging PD-L1 Expression. Journal of nuclear medicine: official publication, Society of Nuclear Medicine 59, 529-535.

40. Downward J. Targeting RAS signaling pathways in cancer therapy. Nat Rev Cancer. 2003 Jan;3(1):11-22. Review. PubMed PMID: 12509763.

41. Dumphy JT, Linder ME. Signaling function of protein palmitoylation. Biochem Biophys Acta 1998;1436:245.

42. Dunkelberger JR, Song WC. Complement and its role in innate and adaptive immune responses. Cell Res. 2010;20:34–50.

43. Dunn Kl, Davie JR Stimulation of the Ras-MAPK pathway leads to independent phosphorylation of histone H3 on serine 10 and 28. Oncogene. 2005 May 12;24(21):3492-502.

44. Ehlerding, E. B., England, C. G., McNeel, D. G., and Cai, W. (2016) Molecular Imaging of Immunotherapy Targets in Cancer. Journal of nuclear medicine: official publication, Society of Nuclear Medicine 57, 1487-1492.

45. Faris Jason Edward, Darrell R. Borger, Carlos Fernandez-del Castillo, Jeffrey W.

Clark, Lawrence Scott Blaszkowsky, Andrew X. Zhu, Jill N. Allen, Janet E. Murphy, Cristina Ferrone, Lipika Goyal, Nabeel Bardeesy, Gabriel Dan Duda, Hui Zheng, David Tsai Ting, Eunice Lee Kwak, Keith D Lillemoe, Jennifer Yon-Li Wo, A. John Iafrate, David P. Ryan, and Theodore S. Hong Effect of molecular genotyping to predict outcomes in patients with metastatic pancreatic cancer. Journal of Clinical Oncology 2014 32:15_suppl, 4128-4128.

46.   Fernández-Medarde A, Santos E. Ras in Cancer and Developmental Diseases. Santos E, ed. Genes & Cancer. 2011;2(3):344-358. doi:10.1177/1947601911411084.

47.   Garon E. B., Rizvi N. A., Hui R., Leighl N., Balmanoukian A. S., Eder J. P., et al. (2015). Pembrolizumab for the treatment of non-small-cell lung cancer. N. Engl. J. Med. 372, 2018–2028. 10.1056/NEJMoa1501824.

48.   Gettinger S. N., Shepherd F. A., Antonia S. J., Brahmer J. R., Chow M. L. Q., Juergens R. A., et al. (2014). First-Line Nivolumab (Anti-PD-1; BMS-936558, ONO-4538) Monotherapy in Advanced NSCLC: Safety, Efficacy, and Correlation of Outcomes with PD-L1 Status. American Society of Clinical Oncology.

49.   Geyer MB, Brentjens RJ. Review: Current clinical applications of chimeric antigen receptor (CAR) modified T cells. Cytotherapy. 2016;18(11):1393-1409. doi:10.1016/j.jcyt.2016.07.003.

50.   Gordon J Freeman, Andrew J Long, Yoshiko Iwai, Karen Bourque, Tatyana Chernova, Hiroyuki Nishimura, Lori J Fitz, Nelly Malenkovich, Taku Okazaki, Michael C Byrne, Heidi F Horton, Lynette Fouser, Laura Carter, Vincent Ling, Michael R Bowman, Beatriz M Carreno, Mary Collins, Clive R Wood, Tasuku Honjo Engagement of the PD-1 immunoinhibitory receptor by a novel B7 family member leads to negative regulation of lymphocyte activation 2000/10/2 Journal Journal of Experimental Medicine Volume 192 Issue 7 Pages 1027-1034.

51.   Grawe RW, Knotts TA. The effects of tether placement on antibody stability on surfaces. The Journal of Chemical Physics. 2017;146(21):215102. doi:10.1063/1.4983705.

52.   Gupta Suprit et al Antibody Labeling with Radioiodine and Radiometals Methods Mol Biol. 2014; 1141: 147–157. doi: 10.1007/978-1-4939-0363-4_9.

53.   Haigis KM, Kendall KR, Wang Y, Cheung A, Haigis MC, Glickman JN, Niwa-Kawakita M, Sweet-Cordero A, Sebolt-Leopold J, Shannon KM, Settleman J, Giovannini M, Jacks T. Differential effects of oncogenic K-Ras and N-Ras on proliferation, differentiation and tumor progression in the colon. Nat Genet. 2008 May;40(5):600-8. doi: 10.1038/ng.115. Epub 2008 Mar 30. PubMed PMID: 18372904; PubMed Central PMCID: PMC2410301.

54.   Halim H, Luanpitpong S, Chanvorachote P. Acquisition of anoikis resistance up-regulates caveolin-1 expression in human non-small cell lung cancer cells. Anticancer Res. 2012 May;32(5):1649-58.

55.   Hammers CM, Stanley JR. Antibody Phage Display: Technique and Applications. The Journal of investigative dermatology. 2014;134(2):e17. doi:10.1038/jid.2013.521.

56.   Harvey Jj. An Unidentified Virus Which Causes The Rapid Production Of Tumours In Mice. Nature. 1964 Dec 12;204:1104-5. PubMed PMID: 14243400.

57.   Hayward WS, Neel BG, Astrin SM. Activation of a cellular onc gene by promoter insertion in ALV-induced lymphoid leucosis. Nature. 1981 Apr 9;290(5806):475-80. PubMed PMID: 6261142.

58.   He Y, Wortmann A, Burke LJ, Reid JC, Adams MN, Abdul-Jabbar I, Quigley JP, Leduc R, Kirchhofer D, Hooper JD. Proteolysis-induced N-terminal ectodomain shedding of the integral membrane glycoprotein CUB domain-containing protein 1 (CDCP1) is accompanied by tyrosine phosphorylation of its C-terminal domain and

recruitment of Src and PKCdelta. J Biol Chem. 2010 Aug 20;285(34):26162-73. doi: 10.1074/jbc.M109.096453. Epub 2010 Jun 15. PubMed PMID: 20551327; PubMed Central PMCID: PMC2924022.

59. He Y, Reid JC, He H, Harrington BS, Finlayson B, Khan T, Hooper JD. Evidence that cell surface localization of serine protease activity facilitates cleavage of the protease activated receptor CDCP1. Biol Chem. 2018 Sep 25;399(9):1091-1097. doi: 10.1515/hsz-2017-0308. PubMed PMID: 29447112.

60. He Y, Harrington BS, Hooper JD. New crossroads for potential therapeutic intervention in cancer - intersections between CDCP1, EGFR family members and downstream signaling pathways. Oncoscience. 2016;3(1):5-8.

61. Hecquet C Lefevre G Valtink M Engelmann K Mascarelli FActivation and role of MAP kinase-dependent pathways in retinal pigment epithelial cells: ERK and RPE cell proliferation. Invest Ophthalmol Vis Sci. 2002 Sep;43(9):3091-8.

62. Hobbs GA1, Der CJ2, Rossman KL1.). J Cell Sci. 2016 Apr 1;129(7):1287-92. doi: 10.1242/jcs.182873. Epub 2016 Mar 16. RAS isoforms and mutations in cancer at a glance.

63. Hodi F. S., O'Day S. J., McDermott D. F., Weber R. W., Sosman J. A., Haanen J. B., et al. (2010)]. Improved survival with ipilimumab in patients with metastatic melanoma. N. Engl. J. Med. 363, 711–723. 10.1056/NEJMoa1003466.

64. Hoedt E, Zhang G, Neubert TA. Stable isotope labeling by amino acids in cellculture (SILAC) for quantitative proteomics. Adv Exp Med Biol. 2014; 806:93-106.doi: 10.1007/978-3-319-06068-2_5. Review. PubMed PMID: 24952180.

65. Hoffmann RM, Coumbe BGT, Josephs DH, et al. Antibody structure and engineering considerations for the design and function of Antibody Drug Conjugates (ADCs). Oncoimmunology. 2018;7(3): e1395127. doi:10.1080/2162402X.2017.1395127.

66. Hooper John D et al Subtractive immunization using highly metastatic human tumor cells identifies SIMA135/CDCP1, a 135 kDa cell surface phosphorylated glycoprotein antigen Oncogene volume 22, pages 1783–1794 (27 March 2003).

67. Huang Chunfa, Carl Freter Lipid Metabolism, Apoptosis and Cancer Therapy Int J Mol Sci. 2015 Jan; 16(1): 924–949. Published online 2015 Jan 2. doi: 10.3390/ijms16010924 PMCID: PMC4307283.

68. Ingley E. Src family kinases: regulation of their activities, levels and identification of new pathways. Biochem Biophys Acta. 2008 Jan;1784(1):56-65. Epub 2007 Aug 22. Review. PubMed PMID: 17905674.

69. Janeway CA Jr, Travers P, Walport M, et al. Immunobiology: The Immune System in Health and Disease. 5th edition. New York: Garland Science; 2001. The structure of a typical antibody molecule.

70. Johnston SR. Targeting downstream effectors of epidermal growth factor receptor/HER2 in breast cancer with either farnesyl transferase inhibitors or mTOR antagonists. Int J Gynecol Cancer. 2006;16 Suppl 2:543-8. Review.

71. Karachaliou N, Chaib I, Cardona AF, Berenguer J, Bracht JWP, Yang J, Cai X. Wang Z, Hu C, Drozdowskyj A, Servat CC, Servat JC, Ito M, Attili I, Aldeguer E. Capitan AG, Rodriguez J, Rojas L, Viteri S, Molina-Vila MA, Ou SI, Okada M, Mok TS, Bivona TG, Ono M, Cui J, Cajal SRY, Frias A, Cao P, Rosell R. Common Co-activation of AXL and CDCP1 in EGFR-mutation-positive Non-smallcell Lung Cancer Associated with Poor Prognosis. EBioMedicine. 2018 Mar; 29:112-127. doi: 10.1016/j.ebiom.2018.02.001. Epub 2018 Feb 5. PubMed PMID: 29433983; PubMed Central PMCID: PMC5925453.

72. Katsuhiko Nakashima, Takamasa Uekita, Shigenobu Yano, Jun-ichi Kikuchi, Ruri Nakanishi, Nozomi Sakamoto, Keisuke Fukumoto, Akihiro Nomoto, Keisuke

Kawamoto, Takashi Shibahara, Hideki Yamaguchi, Ryuichi Sakai Novel small molecule inhibiting CDCP1-PKCδ pathway reduces tumor metastasis and proliferation Cancer Sci. 2017 May; 108(5): 1049–1057. Published online 2017 May 11. doi: 10.1111/cas.13218 PMCID: PMC5448658.

73.   Keeton AB, Salter EA, Piazza GA. The RAS-effector interaction as a drug target. Cancer research. 2017;77(2):221-226. doi: 10.1158/0008-5472.CAN-16-0938.

74.   Khalil Magdy M., Jordi L. Tremoleda, Tamer B. Bayomy and Willy Gsell Molecular SPECT Imaging: An Overview Int J Mol Imaging 2011; 2011: 796025. Published online 2011 Apr 5. doi: 10.1155/2011/796025.

75.   Kohler G, Milstein C (1975) Continuous cultures of fused cells secreting antibody of predefined specificity. Nature 256:495–497.

76.   Kollmorgen G et al Antibody mediated CDCP1 degradation as mode of action for cancer targeted therapy. Mol Oncol. 2013 Dec;7(6):1142-51. doi: 10.1016/j.molonc.2013.08.009. Epub 2013 Sep 3.

77.   Kwak, J. J., Tirumani, S. H., Van den Abbeele, A. D., Koo, P. J., and Jacene, H. A. (2015) Cancer immunotherapy: imaging assessment of novel treatment response patterns and immune-related adverse events. Radiographics: a review publication of the Radiological Society of North America, Inc 35, 424-37.

78.   Vlad, Catalin & Kubelac, Paul & Onisim, Andrea & Irimie, Alexandru & Achimas-Cadariu, Patriciu. (2015). The role of CDCP1 (CUB domain-containing protein 1) and ADAM12 (a disintegrin and metalloproteinase 12) in ovarian cancer. Journal of B.U.ON.: official journal of the Balkan Union of Oncology. 20. 673-679.

79.   Kurosawa G, Sugiura M, Hattori Y, Tsuda H, Kurosawa Y. Classification of 27 Tumor-Associated Antigens by Histochemical Analysis of 36 Freshly Resected Lung Cancer Tissues. Int J Mol Sci. 2016 Nov 8;17(11). pii: E1862. PubMed PMID:

27834817; PubMed Central PMCID: PMC5133862.

80. Lampson BL, Pershing NL Prinz JA Lacsina JR Marzluff WF Nicchitta CVMacAlpine DM Counter CM. Rare codons regulate KRas oncogenesis. Curr Biol. 2013 Jan 7;23(1):70-5. doi: 10.1016/j.cub.2012.11.031.

81. Larson, S.M. 1978. Mechanisms of localization of gallium-68 in tumors. Semin Nucl Med 8:193-203.

82. Le, D. T., Durham, J. N., Smith, K. N., Wang, H., Bartlett, B. R., Aulakh, L. K., Lu, S., Kemberling, H., Wilt, C., Luber, B. S., Wong, F., Azad, N. S., Rucki, A. A., Laheru, D., Donehower, R., Zaheer, A., Fisher, G. A., Crocenzi, T. S., Lee, J. J., Greten, T. F., Duffy, A. G., Ciombor, K. K., Eyring, A. D., Lam, B. H., Joe, A., Kang, S. P., Holdhoff, M., Danilova, L., Cope, L., Meyer, C., Zhou, S., Goldberg, R. M., Armstrong, D. K., Bever, K. M., Fader, A. N., Taube, J., Housseau, F., Spetzler, D., Xiao, N., Pardoll, D. M., Papadopoulos, N., Kinzler, K. W., Eshleman, J. R., Vogelstein, B., Anders, R. A., and Diaz, L. A., Jr. (2017) Mismatch repair deficiency predicts response of solid tumors to PD-1 blockade. Science 357, 409-413.

83. Leroy C, Shen Q, Strande V, Meyer R, McLaughlin ME, Lezan E, Bentires-Alj M, Voshol H, Bonenfant D, Alex Gaither L. CUB-domain-containing protein 1 overexpression in solid cancers promotes cancer cell growth by activating Src family kinases. Oncogene. 2015 Oct 29;34(44):5593-8. doi: 10.1038/onc.2015.19. Epub 2015 Mar 2. PubMed PMID: 25728678; PubMed Central PMCID: PMC4761645.

84. Lesniak, W. G., Chatterjee, S., Gabrielson, M., Lisok, A., Wharram, B., Pomper, M. G., and Nimmagadda, S. (2016) PD-L1 detection in Tumors Using [(64) Cu] Atezolizumab. Bioconjugate Chem. 27, 2103−2110.

85. Li Z, Zhang G, Liu J, Stojanovic A, Ruan C, Lowell CA, Du X. An important role of the SRC family kinase Lyn in stimulating platelet granule secretion. J Biol Chem.

2010 Apr 23;285(17):12559-70. doi: 10.1074/jbc.M109.098756. Epub 2010 Feb 26. PubMed PMID: 20189992; PubMed Central PMCID: PMC2857081.

86.   Li J, Menzel C, Meier D, Zhang C, Dübel S, Jostock T. A comparative study of different vector designs for the mammalian expression of recombinant IgG antibodies. J Immunol Methods. 2007 Jan 10;318(1-2):113-24. Epub 2006 Nov 13. PubMed PMID: 17161420.

87.   Li C, Lee PS, Sun Y, Gu X, Zhang E, Guo Y, Wu CL, Auricchio N, Priolo C, Li J,Csibi A, Parkhitko A, Morrison T, Planaguma A, Kazani S, Israel E, Xu KF, Henske EP, Blenis J, Levy BD, Kwiatkowski D, Yu JJ. Estradiol and mTORC2 cooperate toenhance prostaglandin biosynthesis and tumorigenesis in TSC2-deficient LAM cells. J Exp Med. 2014 Jan 13;211(1):15-28. doi: 10.1084/jem.20131080. Epub 2014 Jan 6. PubMed PMID: 24395886; PubMed Central PMCID: PMC3892971.

88.   Liu Hui, Shao-En Ong, Kwabena Badu-Nkansah, Jeffrey Schindler, Forest M. White, Richard O. Hynes CUB-domain–containing protein 1 (CDCP1) activates Src to promote melanoma metastasis Proc Natl Acad Sci U S A. 2011 Jan 25; 108(4): 1379–1384. doi: 10.1073/pnas.1017228108PMCID: PMC3029734.

89.   Luo Xiangjian, Can Cheng, Zheqiong Tan, Namei Li, Min Tang, Lifang Yang, Ya Cao Emerging roles of lipid metabolism in cancer metastasis Mol Cancer. 2017; 16: 76.   Published online 2017 Apr 11. doi: 10.1186/s12943-017-0646-3 PMCID: PMC5387196.

90.   Markowitz A, Saleemi K, Freeman LM. Role of In-111 labeled CYT-103 immunoscintigraphy in the evaluation of patients with recurrent colorectal carcinoma. Clin Nucl Med. 1993 Aug;18(8):685-700.

91.   Martinko AJ, Truillet C, Julien O, Diaz JE, Horlbeck MA, Whiteley G, Blonder J, Weissman JS, Bandyopadhyay S, Evans MJ, Wells JA. Targeting RAS-driven human

cancer cells with antibodies to upregulated and essential cell-surface proteins. Elife. 2018 Jan 23;7. pii: e31098. doi: 10.7554/eLife.31098. PubMed PMID:29359686; PubMed Central PMCID: PMC5796798.

92. Mayrhofer P, Kunert R. (Nomenclature of humanized mAbs: Early concepts, current challenges and future perspectives. Hum Antibodies. 2018 Jul 23. doi: 10.3233/HAB-180347.

93. Morrison SL: Genetically engineered (chimeric) antibodies. Hosp Pract 15:65-79, 1989.

94. Munnink THO, de Korte MA, Nagengast WB, Timmer-Bosscha H, Schroder CP, de Jong JR, et al. Zr-89-trastuzumab PET visualizes HER2 downregulation by the HSP90 inhibitor NVP-AUY922 in a human tumour xenograft. Eur J Cancer. 2010; 46:678–84.

95. Nagengast WB, de Korte MA, Munnink THO, Timmer-Bosscha H, den Dunnen WF, Hollema H, et al. (89) Zr-bevacizumab PET of early antiangiogenic tumor response to treatment with HSP90 inhibitor NVP-AUY922. J Nucl Med. 2010; 51:761–7.

96. Nakazawa M, Mukumoto M, Miyatake K. Production and purification of polyclonal antibodies. Methods Mol Biol. 2010; 657:63-74. doi: 10.1007/978-1-60761-783-9_5.

97. Narumiya S, Thumkeo D. Rho signaling research: history, current status and future directions. Febs Letters. 2018;592(11):1763-1776. doi:10.1002/1873-3468.13087.

98. Nicodemus CF. Antibody-based immunotherapy of solid cancers: progress and possibilities. Immunotherapy. 2015;7(8):923-939. doi:10.2217/imt.15.57.

99. Nishio K, Sakai K, Togashi Y. PI3K and mTOR pathway and molecular targeted agents. Nihon Rinsho. 2015 Aug;73(8):1315-22. Review. Japanese. PubMed PMID: 26281684.

100. Nisonoff A, Wissler FC, Lipman LN, et al: Separation of univalent fragments from

the bivalent rabbit antibody molecule by reduction of disulfide bonds. Arch Biochem Biophys 89:230-244, 1960.

101. Núñez-Wehinger S et al. Caveolin-1 in cell migration and metastasis. Curr Mol Med. (2014).

102. Ogura T, Yamao K, Hara K, Mizuno N, Hijioka S, Imaoka H, Sawaki A, Niwa Y,Tajika M, Kondo S, Tanaka T, Shimizu Y, Bhatia V, Higuchi K, Hosoda W, Yatabe Y. Prognostic value of K-ras mutation status and subtypes in endoscopic ultrasound-guided fine-needle aspiration specimens from patients with unresectable pancreatic cancer. J Gastroenterol. 2013 May;48(5):640-6. doi:10.1007/s00535-012-0664-2. Epub 2012 Sep 15. PubMed PMID: 22983505.

103. Onda, H., Lueck, A., Marks, P.W., Warren, H.B., and Kwiatkowski, D.J. 1999. Tsc2(+/-) mice develop tumors in multiple sites that express gelsolin and are influenced by genetic background. J Clin Invest 104:687-695.

104. Orchard-Webb David J, Thong Chuan Lee, Graham P Cook, G Eric Blair CUB Domain Containing Protein 1 (CDCP1) modulates adhesion and motility in colon cancer cells BMC Cancer. 2014; 14: 754. doi: 10.1186/1471-2407-14-754 PMCID: PMC4200232.

105. Ostrem, J. M, Peters, U., Sos, M. L., Wells, J. A. & Shokat, K. M. Nature 503, 548–551 (2013).). (KRAS (G12C) inhibitors allosterically control GTP affinity and effector interactions.

106. Pace A, Tapia JA, Garcia-Marin LJ, Jensen RT. The Src family kinase, Lyn, is activated in pancreatic acinar cells by gastrointestinal Hormones / neurotransmitters and growth factors which stimulate its association with numerous other signaling molecules. Biochim Biophys Acta. 2006 Apr;1763(4):356-65. Epub 2006 Apr 7. PubMed PMID: 16713446.

107. Pardoll DM. The blockade of immune checkpoints in cancer immunotherapy. Nature reviews Cancer. 2012;12(4):252-264. doi:10.1038/nrc3239.

108. Patel, S. P., and Kurzrock, R. (2015) PD-L1 Expression as a Predictive Biomarker in Cancer Immunotherapy. Molecular cancer therapeutics 14, 847-56;

109. Perbal B. Communication is the key. Cell Commun Signal. 2003; 1: 3. Published online 2003 Oct 27. doi: 10.1186/1478-811X-1-3.

110. Perk LR, Visser GWM, Vosjan M, Stigter-van Walsum M, Tijink BM, Leemans CR, et al. Zr-89 as a PET surrogate radioisotope for scouting biodistribution of the therapeutic radiometals Y-90 and Lu-117 in tumor-bearing nude mice after coupling to the internalizing antibody cetuximab. J Nucl Med. 2005; 46:1898–906.

111. Press OW Radiolabeled antibody therapy of B-cell lymphomas. Semin Oncol. 1999 Oct;26 (5 Suppl 14):58-65. Review.

112. Pylypenko O, Hammich H, Yu I-M, Houdusse A. Rab GTPases and their interacting protein partners: Structural insights into Rab functional diversity. Small GTPases. 2018;9(1-2):22-48. doi:10.1080/21541248.2017.1336191.

113. Rahib L., B.D. Smith, R. Aizenberg, A.B. Rosenzweig, J.M. Fleshman, L.M. Matrisian Projecting cancer incidence and deaths to 2030: the unexpected burden of thyroid, liver, and pancreas cancers in the United States Cancer Res, 74 (2014), pp. 2913-2921.

114. Rebollo A, Martínez-A C. Ras proteins: recent advances and new functions. Blood. 1999 Nov 1;94(9):2971-80.

115. Redei GP (2008) Immunoglobulins. In: Encyclopedia of Genetics, Genomics, Proteomics and Informatics. Springer, Dordrecht.

116. Redman JM et al Mechanisms of Action of Therapeutic Antibodies for Cancer Mol Immunol. 2015 Oct; 67(2 0 0): 28–45. doi: 10.1016 / j. molimm 2015.04.002.

117. Rizvi, N. A., Hellmann, M. D., Snyder, A., Kvistborg, P., Makarov, V., Havel, J. J., Lee, W., Yuan, J., Wong, P., Ho, T. S., Miller, M. L., Rekhtman, N., Moreira, A. L., Ibrahim, F., Bruggeman, C., Gasmi, B., Zappasodi, R., Maeda, Y., Sander, C., Garon, E. B., Merghoub, T., Wolchok, J. D., Schumacher, T. N., and Chan, T. A. (2015) Cancer immunology. Mutational landscape determines sensitivity to PD-1 blockade in non-small cell lung cancer. Science 348, 124-127.

118. Rojas AM, Fuentes G, Rausell A, Valencia A. The RAS protein superfamily: evolutionary tree and role of conserved amino acids. J Cell Biol. 2012 Jan 23;196(2):189-201. doi: 10.1083/jcb.201103008.

119. Rogers Laura M. Suresh Veeramani, George J. Weiner Complement in monoclonal antibody therapy of cancer August 2014, Volume 59, Issue 1–3, pp 203–210).

120. Rui Huang, Mingwei Wang, Yizhou Zhu, Peter S. Conti, Kai Chen. Development of PET Probes for Cancer Imaging Current Topics in Medicinal Chemistry Volume 15, Issue 8, 2015 DOI: 10.2174/1568026615666150302110325

121. Sapienza MT, Marques FL, Okamoto MR, Hironaka FH, Buchpiguel CA. Anti-CEA monoclonal antibody: technetium-99m labeling and the validation process of a scintigraphic animal model with a non-cellular antigenic implant. Cell Mol Biol (Noisy-le-grand). 2002 Jul;48(5):511-6.

122. Scherl-Mostageer M, Sommergruber W, Abseher R, Hauptmann R, Ambros P, Schweifer N. Identification of a novel gene, CDCP1, overexpressed in human colorectal cancer. Oncogene. 2001 Jul 19;20(32):4402-8. PubMed PMID: 11466621.

123. Seshacharyulu P, Ponnusamy MP, Haridas D, Jain M, Ganti AK, Batra SK. Targeting the EGFR signaling pathway in cancer therapy. Expert Opin Ther Targets. 2012 Jan;16(1):15-31. doi: 10.1517/14728222.2011.648617. Epub 2012 Jan 12. Review. PubMed PMID: 22239438; PubMed Central PMCID: PMC3291787.

124. Sharma, S. K., Chow, A., Monette, S., Vivier, D., Pourat, J., Edwards, K. J., Dilling, T. R., Abdel-Atti, D., Zeglis, B. M., Poirier, J. T., and Lewis, J. S. (2018) Fc-Mediated Anomalous Biodistribution of Therapeutic Antibodies in Immunodeficient Mouse Models. Cancer research 78, 1820-1832.

125. Shattil SJ. Integrins and Src: dynamic duo of adhesion signaling. Trends Cell Biol. 2005 Aug;15(8):399-403. PubMed PMID: 16005629.

126. Sheng C, Qiu J, Wang Y, et al. Knockdown of Ran GTPase expression inhibits the proliferation and migration of breast cancer cells. Molecular Medicine Reports. 2018;18(1):157-168. doi:10.3892/mmr.2018.8952.

127. Siegel R.L., K.D. Miller, A. Jemal Cancer statistics, 2015 CA Cancer J Clin, 65 (2015), pp. 5-29.

128. Simanshu DK, Nissley DV, McCormick F. RAS Proteins and Their Regulators in Human Disease. Cell. 2017;170(1):17-33. doi: 10.1016/j.cell.2017.06.009.

129. Siva AC, Wild MA, Kirkland RE, et al. Targeting CUB domain-containing protein 1 with a monoclonal antibody inhibits metastasis in a prostate cancer model. Cancer Res. 2008;68(10):3759–3766.

130. Slovin S. F., Higano C. S., Hamid O., Tejwani S., Harzstark A., Alumkal J. J., et al. (2013). Ipilimumab alone or in combination with radiotherapy in metastatic castration-resistant prostate cancer: results from an open-label, multicenter phase I/II study. Ann. Oncol. 24, 1813–1821. 10.1093/annonc/mdt107.

131. Smith Matthew J., Benjamin G. Neel, and Mitsuhiko Ikura NMR-based functional profiling of RASopathies and oncogenic RAS mutations PNAS March 19, 2013 110 (12) 4574-4579; https://doi.org/10.1073/pnas.1218173110.

132. Steis RG, Carrasquillo JA, McCabe RP, et al: Evaluation of the toxicity, immunogenicity, and tumor radioimmunodetecting ability of two human monoclonal

antibodies in patients with metastatic colorectal carcinoma. J Clin Oncol 8:476-490, 1990.

133. Stickney DR, Anderson LD, Slater JB, et al: Bifunctional antibody: A binary radiopharmaceutical delivery system for imaging colorectal carcinoma. Cancer Res 51:6650-6655, 1991.

134. Strosberg J et al Phase 3 Trial of 177Lu-Dotatate for Midgut Neuroendocrine Tumors. N Engl J Med. 2017 Jan 12;376(2):125-135. doi: 10.1056/NEJMoa1607427.

135. Strother SC, Casey ME, Hoffman EJ. Measuring PET scanner sensitivity – relating count rates in the image to signal-to-noise ratios using noise equivalent counts. IEEE Trans Nucl Sci 1990; 37:783-8.

136. Sun, Q. et al. (Discovery of small molecules that bind to K-RAS and inhibit Sos-mediated activation. Angew. Chem. Int. Ed. Engl. 51, 6140–6143 (2012).

137. Takai Y, Sasaki T, Matozaki T. Small GTP-binding proteins. Physiol Rev. 2001 Jan;81(1):153-208. Review. PubMed PMID: 11152757.

138. Talukdar S, Pradhan AK, Bhoopathi P, Shen XN, August LA, Windle JJ, Sarkar D, Furnari FB, Cavenee WK, Das SK, Emdad L, Fisher PB. MDA-9/Syntenin regulates protective autophagy in anoikis-resistant glioma stem cells. Proc Natl Acad Sci U S A. 2018 May 29;115(22):5768-5773. doi: 10.1073/pnas.1721650115. Epub 2018 May 14. PubMed PMID: 29760085; PubMed Central PMCID: PMC5984507.

139. Ter-Pogossian, M.M., M.E. Phelps, E.J. Hoffman & N.A. Mullani. 1975. A positron-emission transaxial tomograph for nuclear imaging (PET T). Radiology 114: 89–98.

140. Torre L.A., F. Bray, R.L. Siegel, J. Ferlay, J. Lortet-Tieulent, A. Jemal Global cancer statistics, 2012 CA Cancer J Clin, 65 (2015), pp. 87-108.

141. Troiani T, Napolitano S, Vitagliano D, Morgillo F, Capasso A, Sforza V, Nappi A, Ciardiello D, Ciardiello F, Martinelli E. Primary and acquired resistance of colorectal

cancer cells to anti-EGFR antibodies converge on MEK/ERK pathway activation and can be overcome by combined MEK/EGFR inhibition. Clin Cancer Res. 2014 Jul 15;20(14):3775-86. doi: 10.1158/1078-0432.CCR-13-2181. Epub 2014 May 8. PubMed PMID: 24812410.

142. Uekita T, Jia L, Narisawa-Saito M, Yokota J, Kiyono T, Sakai R. CUB domain-containing protein 1 is a novel regulator of anoikis resistance in lung adenocarcinoma. Mol Cell Biol. 2007;27(21):7649–7660.

143. Uekita T, Tanaka M, Takigahira M, et al. CUB-domain-containing protein 1 regulates peritoneal dissemination of gastric scirrhous carcinoma. Am J Pathol. 2008;172(6):1729–1739.

144. Uekita T, Fujii S, Miyazawa Y, Iwakawa R, Narisawa-Saito M, Nakashima K, Tsuta K, Tsuda H, Kiyono T, Yokota J, Sakai R. Oncogenic Ras/ERK signaling activates CDCP1 to promote tumor invasion and metastasis. Mol Cancer Res. 2014 Oct;12(10):1449-59. doi: 10.1158/1541-7786.MCR-13-0587. Epub 2014 Jun 17. PubMed PMID: 24939643.

145. Uekita T, Sakai R. Roles of CUB domain-containing protein 1 signaling in cancer invasion and metastasis. Cancer Sci. 2011 Nov;102(11):1943-8. doi:10.1111/j.1349-7006.2011.02052.x. Epub 2011 Sep 6. Review. PubMed PMID: 21812858.

146. Valent P, Groner B, Schumacher U, Superti-Furga G, Busslinger M, Kralovics R, Zielinski C, Penninger J, M, Kerjaschki D, Stingl G, Smolen J, S, Valenta R, Lassmann H, Kovar H, Jäger U, Kornek G, Müller M, Sörgel F, Paul Ehrlich (1854-1915) and His Contributions to the Foundation and Birth of Translational Medicine. J Innate Immun 2016; 8:111-120.

147. Van Cutsem E, Lenz HJ, Köhne CH, Heinemann V, Tejpar S, Melezínek I, Beier F, Stroh C, Rougier P, van Krieken JH, Ciardiello F. luorouracil, leucovorin,

andirinotecan plus cetuximab treatment and RAS mutations in colorectal cancer. J Clin Oncol. 2015 Mar 1;33(7):692-700. doi: 10.1200/JCO.2014.59.4812. Epub 2015 Jan 20. PubMed PMID: 25605843.

148. Vandenberghe, S., M.E. Daube-Witherspoon, R.M. Lewitt & J.S. Karp. 2006. Fast reconstruction of 3D time-of-flight PET data by axial rebinning and transverse mashing. Phys. Med. Biol. 51: 1603–1662.

149. Verel I, Visser GWM, Vosjan MJWD, Finn R, Boellaard R, Van Dongen GAMS. High-quality 124I-labelled monoclonal antibodies for use as PET scouting agents prior to 131I-radioimmunotherapy. Eur J Nucl Med Mol I. 2004; 31:1645–52.

150. Vetter I, Wittinhofer A, The Guanine Nucleotide-Binding Switch in Three Dimensions Science 09 Nov 2001: Vol. 294, Issue 5545, pp. 1299-1304 DOI: 10.1126/science.1062023.

151. Vincent PH, Benedikz E, Uhlén P, Hovatta O, Sundström E. Expression of Pluripotency Markers in Nonpluripotent Human Neural Stem and Progenitor Cells. Stem Cells Dev. 2017 Jun 15;26(12):876-887. doi: 10.1089/scd.2016.0346. Epub 2017 Mar 27. PubMed PMID: 28351210.

152. Weber WA, Avril N, Schwaiger M. Relevance of positron emission tomography (PET) in oncology. Strahlenther Onkol 1999; 175:356-73.

153. Wei, W., Jiang, D., Ehlerding, E. B., Luo, Q., and Cai, W. (2018) Noninvasive PET Imaging of T cells. Trends in cancer 4, 359-373.

154. Weiner Louis M., Rishi Surana, and Shangzi Wang Antibodies and cancer therapy: versatile platforms for cancer immunotherapy Nat Rev Immun. 2010 May; 10(05) 317-27 doi: 10.1038/nri2744.

155. Wittinghofer A. Signal transduction via Ras. Biol Chem. 1998 Aug-Sep;379(8-9):933-7. Review. PubMed PMID: 9792425.

156. Wong, A. N. M., McArthur, G. A., Hofman, M. S., and Hicks, R. J. (2017) The Advantages and Challenges of Using FDG PET/CT for Response Assessment in Melanoma in the Era of Targeted Agents and Immunotherapy. European journal of nuclear medicine and molecular imaging 44, 67-77.

157. Wortmann A, He Y, Deryugina EI, Quigley JP, Hooper JD. The cell surface glycoprotein CDCP1 in cancer--insights, opportunities, and challenges. IUBMB Life. 2009 Jul;61(7):723-30. doi: 10.1002/iub.198. Review. PubMed PMID: 19514048.

158. Wright HJ, Arulmoli J, Motazedi M, Nelson LJ, Heinemann FS, Flanagan LA Razorenova OV. CDCP1 cleavage is necessary for homodimerization-induced migration of triple-negative breast cancer. Oncogene. 2016 Sep 8;35(36):4762-72. doi: 10.1038/onc.2016.7. Epub 2016 Feb 15. PubMed PMID: 26876198; PubMed Central PMCID: PMC4985505.

159. Wright Heather J., Jue Hou, Binzhi Xu, Marvin Cortez, Eric O. Potma, Bruce J. Tromberg, Olga V. Razorenova CDCP1 drives triple-negative breast cancer metastasis through reduction of lipid-droplet abundance and stimulation of fatty acid oxidation Proc Natl Acad Sci U S A. 2017 Aug 8; 114(32): E6556–E6565. Published online 2017 Jul 24. doi: 10.1073/pnas.1703791114 PMCID: PMC5559020.

160. Wu AM, Olafsen T Antibodies for molecular imaging of cancer. Cancer J. 2008 May-Jun;14(3):191-7. doi: 10.1097/PPO.0b013e31817b07ae.

161. Yang L, Dutta SM, Troyer DA, Lin JB, Lance RA, Nyalwidhe JO, Drake RR, Semmes OJ. Dysregulated expression of cell surface glycoprotein CDCP1 in prostate cancer. Oncotarget. 2015 Dec 22;6(41):43743-58. doi: 10.18632/oncotarget.6193. PubMed PMID: 26497208; PubMed Central PMCID: PMC4791263.

162. Yashwant Pathak, Simon Benita Antibody-Mediated Drug Delivery Systems: Concepts, Technology, and Applications ISBN: 978-0-470-61281-1 May 2012.

163. Ye X, Chan KC, Waters AM, Bess M, Harned A, Wei BR, Loncarek J, Luke BT Orsburn BC, Hollinger BD, Stephens RM, Bagni R, Martinko A, Wells JA, Nissley DV,McCormick F, Whiteley G, Blonder J. Comparative proteomics of a modelMCF10A-KRasG12V cell line reveals a distinct molecular signature of the KRasG12V cell surface. Oncotarget. 2016 Dec 27;7(52):86948-86971. doi:10.18632/oncotarget.13566. PubMed PMID: 27894102; PubMed Central PMCID: PMC5341332.

164. Ying Dong, Yaowu He, Leonore de Boer, M. Sharon Stack, John W. Lumley, Judith A. Clements, John D The Cell Surface Glycoprotein CUB Domain-containing Protein 1 (CDCP1) Contributes to Epidermal Growth Factor Receptor-mediated Cell Migration. Hooper J Biol Chem. 2012 Mar 23; 287(13): 9792–9803. Published online 2012 Feb 7. doi: 10.1074/jbc.M111.335448 PMCID: PMC3322992.

165. Zanella ER, Galimi F, Sassi F, Migliardi G, Cottino F, Leto SM, Lupo B, Erriquez J, Isella C, Comoglio PM, Medico E, Tejpar S, Budinská E, Trusolino L, Bertotti A. IGF2 is an actionable target that identifies a distinct subpopulation of colorectal cancer patients with marginal response to anti-EGFR therapies. Sci Transl Med. 2015 Jan 28;7(272):272ra12. doi: 10.1126/scitranslmed.3010445. PubMedPMID: 25632036.

166. Zavala VA, Kalergis AM. New clinical advances in immunotherapy for the treatment of solid tumours. Immunology. 2015;145(2):182-201. doi:10.1111/imm.12459.

167. Zeglis BM, Lewis JS. A practical guide to the construction of radiometallated bioconjugates for positron emission tomography. Dalton T. 2011; 40:6168–95).

168. Zeng XJ, Wu YH, Luo M, Cong PG, Yu H. Inhibition of pulmonary carcinoma proliferation or metastasis of miR-218 via down-regulating CDCP1 expression. Eur Rev Med Pharmacol Sci. 2017 Apr;21(7):1502-1508. PubMed PMID: 28429357.

169. Zhang Y, Larraufie MH, Musavi L, Akkiraju H, Brown LM, Stockwell BRDesign of Small Molecules That Compete with Nucleotide Binding to an Engineered Oncogenic KRAS Allele. Biochemistry. 2018 Feb 27;57(8):1380-1389. doi: 10.1021/acs.biochem.7b01113. Epub 2018 Feb 6.

170. Zhou J, Wu Z, Wong G, Pectasides E, Nagaraja A, Stachler M, Zhang H, Chen T. Zhang H, Liu JB, Xu X, Sicinska E, Sanchez-Vega F, Rustgi AK, Diehl JA, Wong KK, Bass AJ. CDK4/6 or MAPK blockade enhances efficacy of EGFR inhibition inoesophageal squamous cell carcinoma. Nat Commun. 2017 Jan 6;8: 13897. doi:10.1038/ncomms13897. PubMed PMID: 28059068; PubMed Central PMCID: PMC5227099.

171. Zhu Z, Aref AR, Cohoon TJ, Barbie TU, Imamura Y, Yang S, Moody SE, Shen RR, Schinzel AC, Thai TC, Reibel JB, Tamayo P, Godfrey JT, Qian ZR, Page AN, Maciag K, Chan EM, Silkworth W, Labowsky MT, Rozhansky L, Mesirov JP, Gillanders WE, Ogino S, Hacohen N, Gaudet S, Eck MJ, Engelman JA, Corcoran RB, Wong KK, Hahn WC, Barbie DA. Inhibition of KRAS-driven tumorigenicity by interruption of an autocrine cytokine circuit. Cancer Discov. 2014 Apr;4(4):452-65. doi: 10.1158/2159-8290.CD-13-0646. Epub 2014 Jan 20.

172. Zipfel PF, Skerka C. Complement regulators and inhibitory proteins. Nat Rev Immunol. 2009;9: 729–740.

173. Zubáčová Z, Krylov V, Tachezy J. Fluorescence in situ hybridization (FISH)mapping of single copy genes on Trichomonas vaginalis chromosomes. Mol Biochem Parasitol. 2011 Apr;176(2):135-7. doi: 10.1016/j.molbiopara. 2010.12.011. Epub2010 Dec 30. PubMed PMID: 21195113.

Supplementary

UCPDAC-187   UCPDAC-208
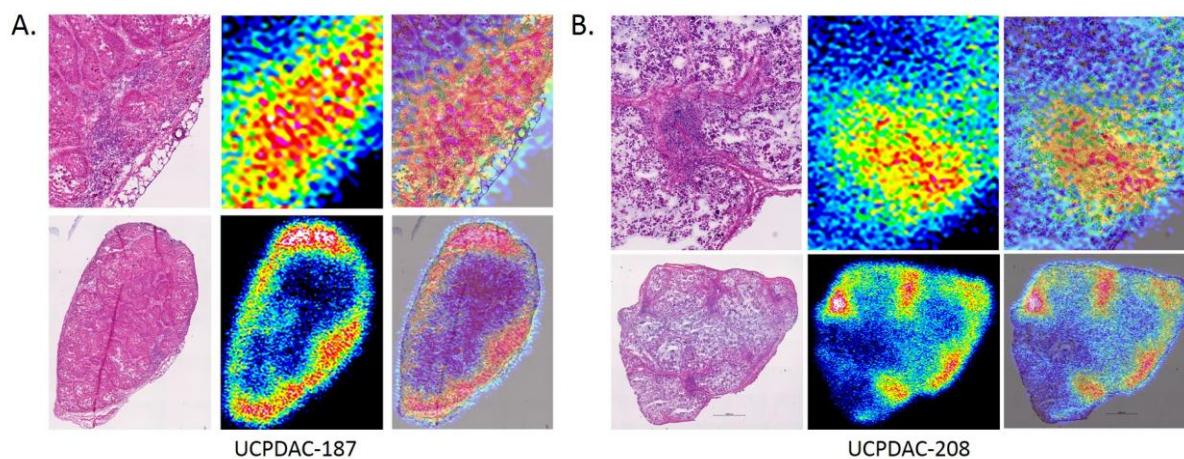
Supplemental Figure 1. *^{89}Zr-4A06 detects pancreatic ductal adenocarcinoma in patient-derived xenografts (PDX).* H&E staining of PDX tumours, digital autoradiography (DAR) showing penetration of PDX tumour by ^{89}Zr-4A06 and merged view, 20X and 40X magnifications. PDXs from two differend patients (A) and (B) are demonstrated.